

Low Temperature Relation for the Trace of the Energy–Momentum Tensor in QCD with Light Quarks¹

N. O. Agasian

Institute of Theoretical and Experimental Physics, ul. Bol'shaya Cheremushkinskaya 25, Moscow, 117218 Russia

e-mail: agasian@heron.itep.ru

Received August 28, 2001

It is shown that the temperature derivatives of the anomalous and normal (quark massive term) contributions to the trace of the energy–momentum tensor in QCD are equal to each other in the low-temperature region. The physical consequences of this relation are discussed. © 2001 MAIK “Nauka/Interperiodica”.

PACS numbers: 12.38.-t; 11.10.Wx

1. The low-energy theorems, playing an important role in the understanding of the vacuum state properties in quantum field theory, were discovered almost at the same time as quantum field methods were being applied to particle physics (see, for example, Low theorems [1]). In QCD, they were obtained in the early eighties [2]. The QCD low-energy theorems, being derived from the very general symmetry considerations and independent of the details of the confinement mechanism, sometimes give information which is not easy to obtain in other ways. Also, they can be used as “physically sensible” restrictions in the constructing of effective theories. Recently, they were generalized to the finite temperature and chemical potential case [3, 4]. These theorems were used for the investigation of a QCD vacuum phase structure in a magnetic field [5] at finite temperature [6].

The investigation of the vacuum state behavior under the influence of various external factors is known to be one of the central problems of quantum field theory. In the realm of strong interactions (QCD), the main factors are the temperature and the baryon density. At low temperatures, $T < T_c$ (T_c is the temperature of the “hadron-quark-gluon” phase transition), the dynamics of QCD is essentially nonperturbative and is characterized by confinement and spontaneous breaking of chiral symmetry (SBCS). In the hadronic phase, the partition function of the system is dominated by the contribution of the lightest particles in the physical spectrum. It is well known that, due to the smallness of pion mass as compared to the typical scale of strong interactions, the pion plays a special role among other strongly interacting particles. Therefore, for many problems of QCD at zero temperature, the chiral limit, $M_\pi \rightarrow 0$, is an appropriate one. On the other hand, a

new mass scale emerges in the physics of QCD phase transitions, namely, the critical transition temperature T_c . Numerically, the critical transition temperature turns out to be close to the pion mass, $T_c \approx M_\pi$.² However, hadron states heavier than those of pions have masses several times larger than T_c and, therefore, their contribution to the thermodynamic quantities is damped by the Boltzmann factor $\sim \exp\{-M_{\text{hadr}}/T\}$. Thus, the thermodynamics of the low-temperature hadronic phase, $T \lesssim M_\pi$, is described basically in terms of the thermal excitations of relativistic massive pions.

In this paper, the low temperature relation for the trace of the energy–momentum tensor in QCD with two light quarks is obtained based on the general dimensional and renormalization-group properties of the QCD partition function and on the dominating role of the pion thermal excitations in the hadronic phase. The physical consequences of this relation, as well as the possibilities to use it in the lattice studies of the QCD at finite temperature are discussed.

2. For nonzero quark mass ($m_q \neq 0$), the scale invariance is broken already at the classical level. Therefore, the pion thermal excitations would change, even in the ideal gas approximation, the value of the gluon condensate with increasing temperature.³ To determine this dependence, use will be made of the general renormalization and scale properties of the QCD partition function.

² The deconfining phase-transition temperature is the one obtained in lattice calculations; $T_c(N_f = 2) \approx 173$ MeV and $T_c(N_f = 3) \approx 154$ MeV [7].

³ At zero quark mass, the gas of massless noninteracting pions is obviously scale-invariant and, therefore, does not contribute to the trace of the energy–momentum tensor and, correspondingly, to the gluon condensate $\langle (G_{\mu\nu}^a)^2 \rangle$.

¹ This article was submitted by the author in English.

The QCD Euclidean partition function with two quark flavors has the following form ($\beta = 1/T$)

$$Z = \int [DA] \prod_{q=u,d} [D\bar{q}][Dq] \exp \left\{ - \int_0^\beta dx_4 \int_V d^3x \mathcal{L} \right\}. \quad (1)$$

Here, the QCD Lagrangian is

$$\mathcal{L} = \frac{1}{4g_0^2} (G_{\mu\nu}^a)^2 + \sum_{q=u,d} \bar{q} \left[\gamma_\mu \left(\partial_\mu - i \frac{\lambda^a}{2} A_\mu^a \right) + m_{0q} \right] q, \quad (2)$$

where the gauge-fixing and ghost terms are omitted. The free-energy density is given by the relation $\beta VF(T, m_{0u}, m_{0d}) = -\ln Z$. Equation (1) yields the following expression for the gluon condensate ($\langle G^2 \rangle \equiv \langle (G_{\mu\nu}^a)^2 \rangle$):

$$\langle G^2 \rangle(T, m_{0u}, m_{0d}) = 4 \frac{\partial F}{\partial(1/g_0^2)}. \quad (3)$$

The system described by the partition function (1) is characterized by the set of dimensionful parameters M , T , $m_{0q}(M)$, and dimensionless charge $g_0^2(M)$, where M is the ultraviolet cutoff. On the other hand, one can consider the renormalized free energy F_R and, by using the dimensional and renormalization-group properties of F_R , recast Eq. (3) in the form containing derivatives with respect to the physical parameter T and renormalized masses m_q .

The phenomenon of dimensional transmutation results in the appearance of a nonperturbative dimensionful parameter

$$\Lambda = M \exp \left\{ \int_{\alpha_s(M)}^{\infty} \frac{d\alpha_s}{\beta(\alpha_s)} \right\}, \quad (4)$$

where $\alpha_s = g_0^2/4\pi$, and $\beta(\alpha_s) = d\alpha_s(M)/d\ln M$ is the Gell-Mann–Low function. Furthermore, as it is well known, the quark mass has an anomalous dimension and depends on the scale M . The renormalization-group equation for $m_0(M)$, the running mass, is $d\ln m_0/d\ln M = -\gamma_m$, and we use the \overline{MS} scheme, for which β and γ_m are independent of the quark mass [4, 8]. Upon integration, the renormalization-group invariant mass is given by

$$m_q = m_{0q}(M) \exp \left\{ \int_{\alpha_s(M)}^{\alpha_s} \frac{\gamma_{m_q}(\alpha_s)}{\beta(\alpha_s)} d\alpha_s \right\}, \quad (5)$$

where the indefinite integral is evaluated at $\alpha_s(M)$. Next we note that, since free energy is a renormalization-group invariant quantity, its anomalous dimension is zero. Thus, F_R has only a normal (canonical) dimension equal to four. Making use of the renorm-invariance of

Λ , one can write in the most general form

$$F_R = \Lambda^4 f \left(\frac{T}{\Lambda}, \frac{m_u}{\Lambda}, \frac{m_d}{\Lambda} \right), \quad (6)$$

where f is some function. From Eqs. (4), (5), and (6) one gets

$$\frac{\partial F_R}{\partial(1/g_0^2)} = \frac{\partial F_R}{\partial \Lambda} \frac{\partial \Lambda}{\partial(1/g_0^2)} + \sum_q \frac{\partial F_R}{\partial m_q} \frac{\partial m_q}{\partial(1/g_0^2)}, \quad (7)$$

$$\frac{\partial m_q}{\partial(1/g_0^2)} = -4\pi\alpha_s^2 m_q \frac{\gamma_{m_q}(\alpha_s)}{\beta(\alpha_s)}. \quad (8)$$

With account taken of Eq. (3), the gluon condensate is given by

$$\begin{aligned} \langle G^2 \rangle(T, m_u, m_d) \\ = \frac{16\pi\alpha_s^2}{\beta(\alpha_s)} \left(4 - T \frac{\partial}{\partial T} - \sum_q (1 + \gamma_{m_q}) m_q \frac{\partial}{\partial m_q} \right) F_R. \end{aligned} \quad (9)$$

It is convenient to choose so large a scale so that one can take the lowest order expressions, $\beta(\alpha_s) \rightarrow -b\alpha_s^2/2\pi$, where $b = (11N_c - 2N_f)/3$ and $1 + \gamma_m \rightarrow 1$. Thus, we have the following equations for condensates

$$\begin{aligned} \langle G^2 \rangle(T) \\ = -\frac{32\pi^2}{b} \left(4 - T \frac{\partial}{\partial T} - \sum_q m_q \frac{\partial}{\partial m_q} \right) F_R \equiv -\hat{D}F_R, \end{aligned} \quad (10)$$

$$\langle \bar{q}q \rangle(T) = \frac{\partial F_R}{\partial m_q}. \quad (11)$$

3. In the hadronic phase, the effective pressure, from which one can extract the condensates $\langle \bar{q}q \rangle(T)$ and $\langle G^2 \rangle(T)$ using the general relations (10) and (11), has the form

$$P_{\text{eff}}(T) = -\varepsilon_{\text{vac}} + P_h(T), \quad (12)$$

where $\varepsilon_{\text{vac}} = \frac{1}{4} \langle \theta_{\mu\mu} \rangle$ is the nonperturbative vacuum energy density at $T = 0$ and

$$\langle \theta_{\mu\mu} \rangle = -\frac{b}{32\pi^2} \langle G^2 \rangle + \sum_{q=u,d} m_q \langle \bar{q}q \rangle \quad (13)$$

is the trace of the energy–momentum tensor. In Eq. (12), $P_h(T)$ is the pressure of thermal hadrons. The quark and gluon condensates are given by the equations

$$\langle \bar{q}q \rangle(T) = -\frac{\partial P_{\text{eff}}}{\partial m_q}, \quad (14)$$

$$\langle G^2 \rangle(T) = \hat{D}P_{\text{eff}}, \quad (15)$$

where the operator \hat{D} is defined by the relation (10)

$$\hat{D} = \frac{32\pi^2}{b} \left(4 - T \frac{\partial}{\partial T} - \sum_q m_q \frac{\partial}{\partial m_q} \right). \quad (16)$$

Consider the $T = 0$ case. One can use the low-energy theorem for the derivative of the gluon condensate with respect to the quark mass [2],

$$\begin{aligned} \frac{\partial}{\partial m_q} \langle G^2 \rangle &= \int d^4x \langle G^2(0) \bar{q}q(x) \rangle \\ &= -\frac{96\pi^2}{b} \langle \bar{q}q \rangle + O(m_q), \end{aligned} \quad (17)$$

where $O(m_q)$ stands for the terms linear in light-quark masses. Then one arrives at the following relation

$$\begin{aligned} \frac{\partial \varepsilon_{\text{vac}}}{\partial m_q} &= -\frac{b}{128\pi^2} \frac{\partial}{\partial m_q} \langle G^2 \rangle + \frac{1}{4} \langle \bar{q}q \rangle \\ &= \frac{3}{4} \langle \bar{q}q \rangle + \frac{1}{4} \langle \bar{q}q \rangle = \langle \bar{q}q \rangle. \end{aligned} \quad (18)$$

Note that three fourths of the quark condensate stem from the gluon part of the nonperturbative vacuum energy density. Along the same lines, one arrives at the expression for the gluon condensate

$$-\hat{D}\varepsilon_{\text{vac}} = \langle G^2 \rangle. \quad (19)$$

In order to get the dependence of the quark and gluon condensates upon T , use is made of the Gell-Mann–Oakes–Renner (GMOR) relation ($\Sigma = |\langle \bar{u}u \rangle| = |\langle \bar{d}d \rangle|$)

$$F_\pi^2 M_\pi^2 = -\frac{1}{2}(m_u + m_d) \langle \bar{u}u + \bar{d}d \rangle = (m_u + m_d) \Sigma. \quad (20)$$

Then we can find the following relations

$$\frac{\partial}{\partial m_q} = \frac{\Sigma}{F_\pi^2} \frac{\partial}{\partial M_\pi^2}, \quad (21)$$

$$\sum_q m_q \frac{\partial}{\partial m_q} = (m_u + m_d) \frac{\Sigma}{F_\pi^2} \frac{\partial}{\partial M_\pi^2} = M_\pi^2 \frac{\partial}{\partial M_\pi^2}, \quad (22)$$

$$\hat{D} = \frac{32\pi^2}{b} \left(4 - T \frac{\partial}{\partial T} - M_\pi^2 \frac{\partial}{\partial M_\pi^2} \right). \quad (23)$$

Within the framework described above, one can derive the thermodynamic relation for the quantum anomaly in the energy–momentum tensor of QCD. At low temperature, the main contribution to the pressure comes from the thermal excitations of massive pions. The general expression for the pressure reads

$$P_\pi = T^4 \phi(M_\pi/T), \quad (24)$$

where ϕ is a function of the ratio M_π/T . Then the following relation is valid

$$\left(4 - T \frac{\partial}{\partial T} - M_\pi^2 \frac{\partial}{\partial M_\pi^2} \right) P_\pi = M_\pi^2 \frac{\partial P_\pi}{\partial M_\pi^2}. \quad (25)$$

With account taken of Eqs. (14), (15), (18), (22), and (25), one gets

$$\Delta \langle \bar{q}q \rangle = -\frac{\partial P_\pi}{\partial m_q}, \quad \Delta \langle G^2 \rangle = \frac{32\pi^2}{b} M_\pi^2 \frac{\partial P_\pi}{\partial M_\pi^2}, \quad (26)$$

where $\Delta \langle \bar{q}q \rangle = \langle \bar{q}q \rangle_T - \langle \bar{q}q \rangle$ and $\Delta \langle G^2 \rangle = \langle G^2 \rangle_T - \langle G^2 \rangle$. In view of Eq. (22), one can recast Eq. (26) in the form

$$\Delta \langle G^2 \rangle = -\frac{32\pi^2}{b} \sum_q m_q \Delta \langle \bar{q}q \rangle. \quad (27)$$

Let us divide both sides of Eq. (27) by ΔT and take the limit $\Delta T \rightarrow 0$. This yields

$$\frac{\partial \langle G^2 \rangle}{\partial T} = -\frac{32\pi^2}{b} \sum_q m_q \frac{\partial \langle \bar{q}q \rangle}{\partial T}. \quad (28)$$

This can be rewritten as

$$\frac{\partial \langle \theta_{\mu\mu}^g \rangle}{\partial T} = \frac{\partial \langle \theta_{\mu\mu}^q \rangle}{\partial T}, \quad (29)$$

where

$$\begin{aligned} \langle \theta_{\mu\mu}^q \rangle &= \sum_{q=u,d} m_q \langle \bar{q}q \rangle \quad \text{and} \\ \langle \theta_{\mu\mu}^g \rangle &= (\beta(\alpha_s)/16\pi\alpha_s^2) \langle G^2 \rangle \end{aligned}$$

are, correspondingly, the quark and gluon contributions to the trace of the energy–momentum tensor. Note that in deriving this result use was made of the low-energy GMOR relation, and, therefore, the thermodynamic relations (28) and (29) are valid in the light quark theory. Thus, in the low-temperature region, where the excitations of massive hadrons and interactions of pions can be neglected, Eq. (29) becomes a rigorous QCD theorem.

As was mentioned above, the pion plays an exceptional role in the thermodynamics of QCD due to the fact that its mass is numerically close to the phase-transition temperature, while the masses of heavier hadrons are several times larger than T_c . This was the reason why the role of massive states in the low-temperature phase was not considered in this paper. This question was discussed in detail in [9]. It was shown there that, at low temperatures, the contribution to $\langle \bar{q}q \rangle$ generated by the massive states is very small and less than 5% if T is below 100 MeV. At $T = 150$ MeV, this contribution is on the order of 10%. The influence of thermal excitations of massive hadrons on the properties of

the gluon and quark condensates was also studied in detail in [10], within the framework of the conformal nonlinear σ model.

4. It was shown that the temperature derivatives of the anomalous and normal (quark massive term) contributions to the trace of the energy–momentum tensor in QCD with light quarks are equal to each other in the low-temperature region.

Let us consider some physical consequences and possible applications of this relation. To this end, we introduce the function

$$\delta_\theta(T) = \frac{\partial}{\partial T} \langle \theta_{\mu\mu}^g - \theta_{\mu\mu}^q \rangle. \quad (30)$$

As was stated above, the function $\delta_\theta(T)$ at low temperatures is close to zero with good accuracy. In the vicinity of and at the phase-transition point, i.e., in the region of nonperturbative vacuum reconstruction, this function changes drastically. To see it, let us first consider pure gluodynamics. It was shown in [11], using the effective dilaton Lagrangian, that gluon condensate decreases very weakly with an increase in temperature up to the phase-transition point. This result is physically transparent and is the consequence of Boltzmann suppression of thermal glueball excitations in the confining phase.

Further, in works [12] the dynamical picture of deconfinement was suggested on the basis of the reconstruction of the nonperturbative gluonic vacuum. Namely, confining and deconfining phases, according to [12], differ, first of all, in the vacuum fields, i.e., in the value of the gluon condensate and in the gluonic field correlators. It was argued in [12] that color-magnetic (CM) correlators and their contribution to the condensate are kept intact across the temperature phase transition, while the confining color-electric (CE) part abruptly disappears above T_c . Furthermore, there exist numerical lattice measurements of field correlators near the critical transition temperature T_c , made by the Pisa group [13], where both CE and CM correlators are found with good accuracy. These data clearly demonstrate the strong suppression of the CE component above T_c and the persistence of CM components. Thus, the function $\delta_\theta(T)_{GD} = \partial \langle \theta_{\mu\mu}^g \rangle / \partial T$ can be presented as a δ function smeared around the critical point T_c with the width $\sim \Delta T$, which defines the fluctuation region of phase transition.

A similar but more complicated and interesting situation takes place in the theory with quarks. The func-

tion $\delta_\theta(T)$ contains the quark term proportional to the chiral phase-transition order parameter $\langle \bar{q}q \rangle(T)$. So, it is interesting to check the relation (29) and to study the behavior of the function $\delta_\theta(T)$ in the lattice QCD at finite temperature. It will allow one to test both the nonperturbative QCD vacuum at low temperatures in the confining phase and to extract additional information on the thermal phase transitions in QCD.

I am grateful to A.B. Kaidalov, V.A. Novikov, Yu.A. Simonov, and A.V. Smilga for useful discussions and comments. This work was supported by the Russian Foundation for Basic Research (project no. 00-02-17836) and INTAS (grant no. 110).

REFERENCES

1. F. E. Low, Phys. Rev. **110**, 974 (1958).
2. V. A. Novikov, M. A. Shifman, A. I. Vainshtein, and V. I. Zakharov, Nucl. Phys. B **191**, 301 (1981); Fiz. Élem. Chastits At. Yadra **13**, 542 (1982) [Sov. J. Part. Nucl. **13**, 224 (1982)]; A. A. Migdal and M. A. Shifman, Phys. Lett. B **114**, 445 (1982).
3. P. J. Ellis, J. I. Kapusta, and H.-B. Tang, Phys. Lett. B **443**, 63 (1998).
4. I. A. Shushpanov, P. J. Ellis, and J. I. Kapusta, Phys. Rev. C **59**, 2931 (1999).
5. N. O. Agasian and I. A. Shushpanov, Pis'ma Zh. Éksp. Teor. Fiz. **70**, 711 (1999) [JETP Lett. **70**, 717 (1999)]; Phys. Lett. B **472**, 143 (2000).
6. N. O. Agasian, Phys. Lett. B **488**, 39 (2000); Yad. Fiz. **64**, 608 (2001) [Phys. At. Nucl. **64**, 554 (2001)].
7. F. Karsch, E. Laermann, and A. Peikert, hep-lat/0012023; F. Karsch, hep-ph/0103314.
8. T. Muta, *Foundations of Quantum Chromodynamics: an Introduction to Perturbative Methods in Gauge Theories* (World Scientific, Singapore, 1998), World Scientific Lecture Notes in Physics, Vol. 57.
9. P. Gerber and H. Leutwyler, Nucl. Phys. B **321**, 387 (1989).
10. N. O. Agasian, D. Ebert, and E.-M. Ilgenfritz, Nucl. Phys. A **637**, 135 (1998).
11. N. O. Agasian, Pis'ma Zh. Éksp. Teor. Fiz. **57**, 200 (1993) [JETP Lett. **57**, 208 (1993)].
12. Yu. A. Simonov, Pis'ma Zh. Éksp. Teor. Fiz. **54**, 256 (1991) [JETP Lett. **54**, 249 (1991)]; Pis'ma Zh. Éksp. Teor. Fiz. **55**, 605 (1992) [JETP Lett. **55**, 627 (1992)]; Yad. Fiz. **58**, 357 (1995) [Phys. At. Nucl. **58**, 309 (1995)].
13. A. Di Giacomo, E. Meggiolaro, and H. Panagopoulos, Nucl. Phys. B **483**, 371 (1997).

Shedding and Interaction of Solitons in Imperfect Medium¹

M. Chertkov¹, I. Gabitov¹, I. Kolokolov^{1,2}, and V. Lebedev^{1,3,4}

¹Theoretical Division, LANL, Los Alamos, NM 87545, USA

²Budker Institute of Nuclear Physics, Siberian Division, Russian Academy of Sciences,
pr. akademika Lavrent'eva 11, Novosibirsk, 630090 Russia

³Landau Institute for Theoretical Physics, Russian Academy of Sciences, Moscow, 117334 Russia

⁴Physics Department, Weizmann Institute of Science, Rehovot 76100, Israel

Received September 6, 2001

The propagation of a soliton pattern through one-dimensional medium with weakly disordered dispersion is considered. Solitons, perturbed by this disorder, radiate. The emergence of a long-range interaction between the solitons, mediated by the radiation, is reported. Basic soliton patterns are analyzed. The interaction is triple and is extremely sensitive to the phase mismatch and relative spatial separations within the pattern. This phenomenon is a generic feature of any problem explaining adiabatic evolution of solitons through a medium with frozen disorder. © 2001 MAIK "Nauka/Interperiodica".

PACS numbers: 42.65.Tg; 42.81.Dp

We consider long-range soliton interaction mediated by radiation in nonlinear 1d system with frozen disorder. The problem is of a great importance for nonlinear fiber optics of the next generation (see, e.g., [1, 2]), and it is also of general relevance for any of the traditional fields, like plasma physics, where propagation of solitary waves is possible. Our aim here is to answer the following sets of fundamental questions:

What statistics describe the radiation emitted due to disorder by a single soliton or a pattern of solitons? How far do the radiation wings extend from the peak of the soliton(s)? What is the structure of the wings?

How strong is the radiation mediating interaction between the solitons? How is the interaction modified if we vary the soliton positions and phases within a pattern of solitons?

We focus on the dynamics of wave packets. The universal coarse-grained description of a wave packet envelope is given by the nonlinear Schrödinger equation (NLS) [3–5]. We consider the 1d problem motivated mainly by applications to fiber optics [6]

$$i\partial_z\psi + d(z)\partial_t^2\psi + 2|\psi|^2\psi = 0. \quad (1)$$

The medium (fiber) is imperfect; i.e., various macroscopic characteristics of the fiber fluctuate in space. Fluctuations of the dispersion coefficient, d , are believed to be one of the major sources of disorder present in real fibers [7]. This disorder is frozen; i.e., d is a random function of z . We assume that d fluctuates on short spatial scales and that the fiber is homogeneous on larger scales. The averaged value of d is a constant, which can be rescaled to unity by changing the units

of t . One obtains $d = 1 + \xi(z)$, where $\langle \xi \rangle = 0$. According to the Central Limit Theorem [8], ξ at scales larger than the correlation length can be treated as a homogeneous Gaussian random process with zero mean and described by the quantity $D = \int dz \langle \xi(z)\xi(z') \rangle$, which is the noise intensity. The pair correlation function of ξ is

$$\langle \xi(z_1)\xi(z_2) \rangle = D\delta(z_1 - z_2). \quad (2)$$

We assume that the disorder is weak; i.e., $D \ll 1$.

At $z = 0$, a sequence of well-separated solitons is launched. In an ideal medium ($\xi = 0$), each of the solitons is preserved dynamically gaining, according to the exact single-soliton solution of Eq. (1), only a multiplicative phase factor. Because the medium is imperfect, the solitons, perturbed by impurities, shed radiation. The first problem is to describe the radiation. The soliton loses energy shedding radiation. Another problem is to describe the degradation of a single soliton. The tails of different solitons interfere with each other, forming a collective background. This fluctuating background affects all solitons. It results in the emergence of a long-range effective intersoliton interaction, which is the final (but not the least) problem to be addressed. The long-range interaction dominates the direct interaction due to overlapping of soliton tails, as this direct interaction decays exponentially with separation [9, 10]. The emergence of the long-range interaction between the imperfect solitons in the pure ($\xi = 0$) NLS, mediated by the emitted radiation, was noted in [11]. The description of the calculation details, only briefly explained here, will be published elsewhere.

To examine the effects, one should separate the degrees of freedom explaining solitons themselves and

¹ This article was submitted by the authors in English.

their continuous spectrum (radiation). For a single soliton, this can be done as follows

$$\psi = \eta \exp\left(i \int_0^z \eta^2 dz\right) \left\{ \frac{\exp[i\alpha + i\beta(t-y)]}{\cosh[\eta(t-y)]} + v \right\}, \quad (3)$$

where the four variables $\eta(z)$, $\alpha(z)$, $y(z)$, $\beta(z)$ are the amplitude, phase, position, and the phase velocity of the soliton, respectively, and $v(t; z)$ stands for the continuous spectrum. The function v can be expanded in a complete set of delocalized eigenfunctions of the unperturbed ($\xi = 0$) NLS Eq. (1) linearized on the background of the perfect soliton [12, 13]. The continuous spectrum is separated by a gap in frequency from the four zero modes, associated with variations of η , α , y , β . The zero modes are localized in t . If D is finite but small, the four parameters vary slowly with z , in contrast to the fast fluctuations of v , which are also small in amplitude. The separation of the slow and fast variables is the heart of the adiabatic approximation [12–16], which we explore here.

For a single soliton, the parameters y and β , which are assumed to be zero initially, cannot change due to the $t \rightarrow -t$ symmetry of Eq. (1). Thus, only two out of four soliton variables, η and α , evolve. The phase α is influenced by the noise ξ directly, $\partial_z \alpha = -\xi$, whereas η is affected by the noise indirectly, through the radiation shed by the soliton. Substituting Eq. (3) into Eq. (1) and keeping terms only linear in v and ξ , one arrives at an inhomogeneous equation for v with a source term proportional to ξ . The source is localized on the soliton. Solving the equation and averaging the result over the statistics of ξ , one deduces the expression

$$\langle |v|^2 \rangle \approx \frac{\pi}{16} D \eta^4 \ln \left[\frac{z\eta}{t} \right] \quad (4)$$

valid for $z\eta \gg t \gg 1$. Eq. (4) describes the extended radiation tails shed by the soliton due to medium imperfectness. One observes a very slow decay of the radiation intensity in t . Equation (4) applies at any large z (the soliton is always well distinguishable from the radiation). To disclose the z dependence of η , one can use the conservation of the integral $\int dt |\psi|^2$, $2\eta + \int dt \eta^2 |v|^2 = 2$. It shows that variations of η emerge in the second order in v . At $z \gg 1$, the quantity $\int dt |v|^2$ is self-averaged. Therefore, $|v|^2$ in the integral relation can be replaced by its average value, which is a function of η , according to Eq. (4). The result is a closed equation for η , and, finally, the solution

$$\eta(z) = (1 + 8Dz/3)^{-1/5}. \quad (5)$$

One concludes that the shedding soliton amplitude, η , remains unchanged until $z\eta$ reaches the scale $z\eta = 1/D$.

Let us proceed to the multisoliton case. A qualitatively new effect, associated with interaction of the shedding solitons through their radiation, emerges here (the effect can be compared with the van der Waals interaction, although the later is mediated by virtual photons whereas the intersoliton interaction is due to real radiation). The soliton positions are the first among other soliton parameters to be affected by the interaction. An essential change in the positions takes place at scales much shorter than $z\eta$, where the soliton amplitudes are unchanged (still $z \gg 1$). This enables us to seek a solution of Eq. (1) in the form

$$\psi = \exp(iz) \left\{ \sum_m \frac{\exp[i\alpha_m + i\beta_m(t-y_m)]}{\cosh[t-y_m]} + v \right\}, \quad (6)$$

where each term in the sum corresponds to a soliton, and v describes the continuous spectrum. One can derive equations for the soliton parameters, α_m , β_m , y_m , making use of the adiabatic approximation. The continuous spectrum is to be studied by substituting Eq. (6) into Eq. (1), and its subsequent linearization with respect to v and ξ . Equations for the soliton parameters are derived from Eq. (1) in the second order in v . Furthermore, as in the single-soliton case, $\int dt |v|^2$ is self-averaged, and therefore can be replaced by its noise average, which is a function of the soliton parameters. The resulting equations describing the slow dynamics of β_m and y_m are

$$\partial_z y_m = 2\beta_m, \quad \partial_z \beta_m = F_m, \quad (7)$$

$$F_m = -\frac{\pi D}{36} \sum_{j,n} \cos(\alpha_j - \alpha_n) (y_j + y_n - 2y_m)^{-1}, \quad (8)$$

where the $j = n = m$ contribution has to be excluded from the sum. It is assumed in Eq. (8) that all the triple combinations, $|y_j + y_n - 2y_m|$, are large. The phase velocities, β_m , which are zero initially, remain small, $\sim Dz \ll 1$, and their effects on the continuous spectrum can be neglected. In spite of this smallness, the β terms in the equation for y give the major, $O(Dz)$, contribution (dominating the one proportional to $|v|^2 \sim O(D)$, omitted in Eq. (7) for β). The direct contributions from the noise to the absolute phase, which is $O(\xi)$, cancel out from the phase differences in Eq. (8). Other changes in the phases are not essential for $z \ll 1/D$.

The two-soliton version of Eqs. (7), (8) reads

$$\partial_z^2 x = \frac{\pi D}{18x} (1 + 4 \cos \alpha), \quad (9)$$

where $\alpha = \alpha_1 - \alpha_2$ is the phase mismatch between the solitons and $x = y_2 - y_1$ stands for their relative separation. Eq. (9) describes the long-range interaction between the solitons. The α dependence in Eq. (9) originates from the interference of the radiated waves with the same wavelengths, moving in opposite directions

(in other words, joint radiation of the system of two solitons is not just a sum of the two single-soliton contributions). Notice that similar interference leads to the Anderson localization in $1d$ random media [17]. The sign of the interaction is controlled by the phase mismatch α : solitons repel each other if $0 < |\alpha| < \alpha_c \approx 1.823$, while $\alpha_c < |\alpha| < \pi$ corresponds to the solitons' attraction. The picture is opposite here to the one explaining the direct interaction of solitons, where the attraction at $\alpha = 0$ changes to repulsion at $\alpha = \pi$ [9, 10]. The solution to Eq. (9) with the condition $\partial_z x(0) = 0$ is given by

$$x(0)\text{Erfi}\{\sqrt{\ln[x/x(0)]}\} = z\sqrt{(1+4\cos(\alpha))D/9}, \quad (10)$$

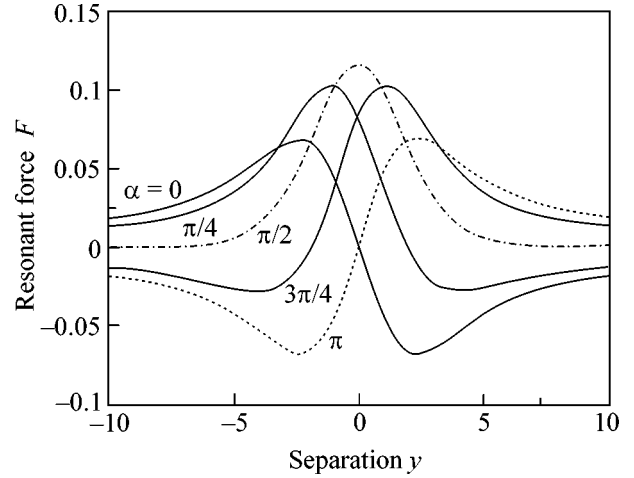
where Erfi is the imaginary error function. One finds that x changes on the order of its initial value at $z \sim z_{\text{int}} = x/\sqrt{D}$. Therefore, the scale separation, $z_{\text{int}} \ll z_\eta$, assumed in the derivation of Eqs. (7)–(10), is justified.

The intersoliton interaction, described by Eqs. (7), (8), is triple. One may expect that a new physics, missed in the consideration of a soliton pair, would show itself in the more complex three-soliton case. A special, extremely long-range, resonant interaction is indeed emerging here if the triple combination, $y \equiv y_1 + y_3 - 2y_2$, is $O(1)$, in spite of the fact that all the pair separations, $x_{jm} = y_m - y_j$, in the triad are large, $|x_{jm}| \gg 1$. The resonant contribution to the intersoliton force (8), acting on the soliton positioned at y_2 , is given by

$$F = \frac{\pi^2 D}{18} \text{Im} \int_0^\infty \frac{dq q (1+q^2)^2 e^{i\alpha - iqy}}{\cosh^2(\pi q/2) \sinh(\pi q)}, \quad (11)$$

where the ordering, $y_1 < y_2 < y_3$, is assumed. At $x_{13} \gg y \sim 1$, the resonant term, which is $O(1)$, dominates the nonresonant one, which is $O(1/x)$. The dependence of the resonant force on y for different values of the phase mismatch $\alpha = \alpha_1 - \alpha_3$ is shown in the figure. One observes that the middle soliton (positioned at y_2) is stable [$F(y)$ is negative at the node position y_0 , given by $F(y_0) = 0$] if $|\alpha| < \pi/2$, and unstable otherwise. The stability implies dynamical oscillations of the middle soliton around the stable node y_0 , with a period in z estimated by $z_{\text{osc}} \sim 1/\sqrt{D}$. The period of the oscillations is still much shorter than $z_{\text{int}} \sim x_{13}/\sqrt{D}$, where the size of the triad (x_{13}) changes on the order of its initial value. At $z \sim z_{\text{int}}$, the triad extends (or contracts, depending on the phases) as a whole under the action of the $\sim 1/x_{13}$ interaction, still keeping the relative positions of the solitons within the triad intact. The unstable case, which takes place if $\pi/2 < |\alpha| < \pi$, corresponds to the uncertainty of the relative positions of solitons within the triad at $z \sim z_{\text{int}}$. The figure also shows that the position of the node y_0 depends on the phase mismatch α .

In the multisoliton case, the dynamics of the pattern is controlled by Eqs. (7) and (8), provided all denomi-



Three-soliton resonant force $F(y)$ measured in the units of D .

nators are large. However, resonant configurations are possible here as well. Each of the configurations corresponds to a set of three solitons positioned according to $y_1 + y_3 - 2y_2 = O(1)$. The other solitons displayed inside the resonant pattern (in between y_1 and y_3) do affect the resonant interaction; i.e., it changes the force acting on the soliton positioned at y_2 . If the difference between the number of solitons in between y_1, y_2 , and y_2, y_3 , respectively, is n , the expression (11) is modified via the multiplier, $[(q+i)/(q-i)]^{2n}$, inserted into the integrand.

Let us summarize the fundamental features of the interaction between the solitons through their radiation induced by disorder. First of all, the weakness of disorder, $D \ll 1$, allows us to reduce the original field problem, given by Eq. (1), to the N -body one, described by Eqs. (7) and (8). Also, in spite of the stochastic nature of the original problem, the N -body problem is *deterministic*. This is a consequence of the self-averaging nature of the radiation intensity, $|\nu|^2$. Second, the interaction between the solitons through their radiation is not pairwise. It is seen, in particular, through the triple character of the force F_m driving the β_m change in Eq. (7) [each term in Eq. (8) corresponds to a contribution from a triad of solitons]. Third, the interaction in Eq. (8) for $x \gg 1$ is generically algebraic, i.e., long-range. Fourth, not all the triple configurations contribute $O(D/x)$ into F_m ; contribution from a resonant triad with $y \equiv y_j + y_k - 2y_m \sim 1$ is $O(D)$. Finally, the interaction is very sensitive to the soliton phases.

From the point of view of fiber optics applications, the effect of the mutual interactions of the shedding solitons mediated by their radiation is really strong and potentially destructive (the major requirement here is to preserve relative separations between solitons, which are bits of information, and not to allow the solitons to leave their allocated time slots). However, there exists another side of the analysis which may actually help to

cure the problem. The dynamics is very sensitive to the values of the relative phases and positions in the soliton sequence, and there is certainly a great potential for reducing the intersoliton forces by calibrating the positions (within the allocated slots) and phases of the solitons.

Another, radical (pattern-independent) way to improve characteristics of propagation through noisy lines, called the pinning method, was suggested recently in [18]. The idea is to pin the integral dispersion, $\int dz \xi$, to zero by inserting periodically short spans of fiber with carefully controlled dispersion. Let us now briefly explain how the pinning affects the phenomenon introduced in this paper. The pinning is effective if the pinning period, l , is shorter than all other scales; i.e., if $l \ll 1$. Then, on the larger scales, the effective noise, ξ_{pin} , is described by

$$\langle \xi_{\text{pin}}(z_1) \xi_{\text{pin}}(z_2) \rangle = -\frac{Dl^2}{3} \delta''(z_1 - z_2). \quad (12)$$

Pinning of the noise leads to modification of the soliton degradation law (5), $\eta_{\text{pin}} = (1 + 64Dl^2z/315)^{-1/9}$. The interaction of solitons is reduced by pinning. It is displayed through renormalization of D , $D \rightarrow Dl^2\eta^4/3$ in Eq. (4), and $D \rightarrow Dl^2/3$ in Eqs. (7) and (10).

Let us emphasize that the phenomenon described in this paper is generic. Regardless of whether it is additive or multiplicative frozen (t -independent), noise stimulates the shedding of radiation by solitons, which, in turn, mediates a long-ranged interaction between solitons. This long-ranged triple, and nonrandom character of the interaction, along with the sensitivity of the phenomenon to phases are generic features of any problem explaining the adiabatic evolution of solitons in the presence of induced radiation. However, if spatiotemporal (short-correlated both in t and z) noise is considered, the radiation effect, equivalent to the one considered in the letter, is masked by a jitter in relative soliton positions, $\delta y^2 \sim \tilde{D} z^3$ [19–21], where \tilde{D} measures the intensity of the noise. Different solitons jitter independently; i.e., fluctuations of intersoliton separations are described by the same δy . This spatiotemporal jitter is effective at the scales, $\sim \tilde{D}^{-1/3}$, where the long-range interaction of solitons mediated by radiation (a phenomenon equivalent to the one considered in this paper) is still not essential.

The algebraic, $\sim 1/x$, character of the interaction is closely related to the reflectiveness feature of the continuous radiation scattering on the soliton. However, the scattering becomes reflective in some nonintegrable generalizations of Eq. (1) that are of physical importance. The reflectivity leads to essential changes in the properties of the radiation and of the intersoliton interaction. The reported stochastic phenomena (along with others of the kind caused by random birefringence of

the fiber [22] and multichannel interaction)² plays an important role in fiber communications.

We conclude this paper by brief discussion of real world parameters which would lead to the practical observation and system impact of the predicted effects in fiber optics communication. It was reported in [7] that fluctuations of the dispersion coefficient in a sample of the “dispersion shifted” fiber are on the order of its average value, i.e., ~ 1 ps/nm km, while the typical scale of the variations in dispersion is estimated from above by 1 km (the actual correlation scale is, probably, defined by linear dimensions of the devices used in the fiber production; i.e., it is somehow shorter, ~ 100 m). Therefore, for the pulse width of ~ 7 ps (that corresponds to a 28 Gb/s single-channel transmission rate) and the pulse period of ~ 50 km, D is estimated by 10^{-3} – 10^{-2} . Then, the soliton interaction is seen at $z_{\text{int}} \sim (2000\text{--}5000)$ km if solitons are separated by five soliton width. Notice, however, that a decrease in the pulse width by a factor of q (correspondent to the factor q increase of the transmission rate) leads to the q^2 decrease in z_{int} .

We are grateful to G.D. Doolen for useful comments. This work was supported by the LDRD ER 2001109 at LANL; the J. R. Oppenheimer fellowship (MC), DOE through Contract no. W-7-405-ENG-36 and its Program in Applied Mathematical Sciences, KJ-01-01 (IG); and the Russian Foundation for Basic Research (project no. 00-02-17652) (IK).

REFERENCES

1. H. Haus, W. Wong, and F. Khatri, *J. Opt. Soc. Am. B* **14**, 304 (1997).
2. L. Socci and M. Romagnoli, *J. Opt. Soc. Am. B* **16**, 12 (1999).
3. S. P. Novikov, S. V. Manakov, L. P. Pitaevskii, and V. E. Zakharov, *Theory of Solitons: The Inverse Scattering Methods* (Nauka, Moscow, 1980; Consultants Bureau, New York, 1984).
4. A. Newell, *Solitons in Mathematics and Physics* (SIAM, Philadelphia, 1985; Mir, Moscow, 1989).
5. M. Ablowitz and H. Segur, *Solitons and the Inverse Scattering Transform* (SIAM, Philadelphia, 1981; Mir, Moscow, 1986).
6. G. P. Agrawal, *Fiber-Optic Communication Systems* (Wiley, New York, 1997).
7. L. F. Mollenauer, P. V. Mamyshev, and M. J. Neubelt, *Opt. Lett.* **21**, 1724 (1996).
8. W. Feller, *An Introduction to Probability Theory and Its Applications* (Wiley, New York, 1957; Mir, Moscow, 1964).
9. V. I. Karpman and V. V. Soloviev, *Physica D (Amsterdam)* **3**, 487 (1981).
10. J. P. Gordon, *Opt. Lett.* **8**, 596 (1983).

²In the multichannel case, an additional mechanism of interpulse interaction in the same channel mediated by quasi-random sequence of pulses passing through the other channels may play an essential role.

11. E. A. Kuznetsov, A. V. Mikhailov, and I. A. Shimokhin, *Physica D (Amsterdam)* **87**, 201 (1995).
12. D. J. Kaup, *Phys. Rev. A* **42**, 5689 (1990).
13. D. J. Kaup, *Phys. Rev. A* **44**, 4582 (1991).
14. N. N. Bogoljubov, Ju. A. Mitropoliskii, and A. M. Samoilenko, *Methods of Accelerated Convergence in Nonlinear Mechanics* (Naukova Dumka, Kiev, 1969; Springer-Verlag, New York, 1976).
15. V. I. Karpman and E. M. Maslov, *Zh. Éksp. Teor. Fiz.* **73**, 537 (1977) [*Sov. Phys. JETP* **46**, 281 (1977)].
16. D. J. Kaup and A. C. Newell, *Proc. R. Soc. London, Ser. A* **361**, 413 (1978).
17. I. M. Lifshits, S. A. Gredeskul, and L. A. Pastur, *Introduction to the Theory of Disordered Systems* (Nauka, Moscow, 1982; Wiley, New York, 1988).
18. M. Chertkov, I. Gabitov, and J. Moeser, nlin.cd/0011043.
19. J. N. Elgin, *Phys. Lett. A* **110**, 441 (1985).
20. J. P. Gordon and H. A. Haus, *Opt. Lett.* **11**, 665 (1986).
21. G. E. Falkovich, I. Kolokolov, V. Lebedev, and S. K. Turitsyn, *Phys. Rev. E* **63**, 025601 (2001).
22. M. Chertkov, I. Gabitov, I. Kolokolov, and V. Lebedev, submitted to *Opt. Lett.*; <http://cnls.lanl.gov/~chertkov/Fiber>.

Dust Ion-Acoustic Shock-Wave Structures: Theory and Laboratory Experiments

S. I. Popel, A. P. Golub', and T. V. Losseva

Institute of Geosphere Dynamics, Leninskiĭ pr. 38-6, Moscow, 117334 Russia

e-mail: s_i_popel@mtu-net.ru; popel@horus.tp1.ruhr-uni-bochum.de

Received August 22, 2001

An evolutionary theoretical model is developed that describes dust ion-acoustic shock waves in dusty plasma consisting of ions (treated in the hydrodynamic approximation), Boltzmann electrons, and variable-charge dust grains. Account is taken not only of ionization, absorption, momentum loss by electrons and ions in collisions with dust grains, and gas-kinetic pressure effects but also of the processes peculiar to laboratory plasmas. It is shown that the model is capable of describing all the main experimental results on dust ion-acoustic shock waves [Q.-Z. Luo *et al.*, *Phys. Plasmas* **6**, 3455 (1999); Y. Nakamura *et al.*, *Phys. Rev. Lett.*, **83**, 1602 (1999)].
© 2001 MAIK "Nauka/Interperiodica".

PACS numbers: 52.27.Lw; 52.35.Tc

The problem of shock waves occupies an important place in present-day physics of dusty plasmas. Shock waves in a dusty plasma have specific features that distinguish them from ordinary collisional and collisionless shock waves and are attributed, in particular, to the anomalous dissipation originating from dust grain charging. In dusty plasma, anomalous dissipation suggests the possibility of existence of a new kind of shock waves, which are collisionless in the sense that they are insignificantly affected by electron–ion collisions. However, in contrast to classical collisionless shock waves, the anomalous dissipation due to dust charging involves interaction of the electrons and ions with dust grains in the form of microscopic electron and ion currents to the grain surfaces. That dust ion-acoustic shock waves associated with anomalous dissipation can actually exist was proved analytically in [1]. The dust ion-acoustic mode in a dusty plasma is analogous to the ion-acoustic mode in a conventional two-component electron–ion plasma. The difference in their dispersion properties is explained as being due to the effects peculiar to dusty plasmas (processes at the grain surfaces, fluctuations of the grain charge, recombination of electrons and ions, etc.). Dust ion-acoustic shock waves were observed for the first time in laboratory experiments at the University of Iowa (USA) [2] and at the Institute of Space and Astronautical Science (Japan) [3]. Experiments on shock waves in dusty plasmas are being conducted in a number of major research laboratories throughout the world. There are also plans to carry out such experiments during the mission of the International Space Station. In this context, one of the most urgent tasks is to develop theoretical models that will adequately describe the relevant experiments. Here, we construct a theoretical model for describing

dust ion-acoustic shock waves and compare theoretical conclusions with the experimental data.

Let us briefly formulate the main experimental results. The experiments carried out by Luo *et al.* [2] with the Q-machine showed that:

(i) Dust ion-acoustic shock waves are generated at sufficiently high dust densities (under the experimental conditions of [2], at dust densities such that $\epsilon Z_{d0} \equiv n_{d0} Z_{d0} / n_{i0} \geq 0.75$, where $q_d = -Z_d e$ is the grain charge, $-e$ is the electron charge, n_d is the dust density, n_i is the ion density, and the subscript 0 stands for the unperturbed plasma parameters). In [2], the conclusion about the formation of a shock wave was drawn from the fact that the perturbation front steepens as time elapses. At sufficiently low dust densities, the perturbation front does not steepen but instead widens.

(ii) When the shock wave structure has formed, the shock front width $\Delta\xi$ is described by the following theoretical estimate, which is based on the model developed in [1]:

$$\Delta\xi \sim M c_s / v_q, \quad (1)$$

where $M c_s$ is the speed of the shock-wave structure, M is the Mach number, $c_s = \sqrt{T_e / m_i}$ is the ion acoustic speed, $v_q = \omega_{pi}^2 a (1 + z_0 + T_i / T_e) / \sqrt{2\pi} v_{Ti}$ is the grain charging rate, $\omega_{pi} = \sqrt{4\pi n_{i0} e^2 / m_i}$ is the ion plasma frequency, m_i is the mass of an ion, a is the grain radius, $z = Z_d e^2 / a T_e$, $T_{e(i)}$ is the electron (ion) temperature, and $v_{Ti} = \sqrt{T_i / m_i}$ is the ion thermal velocity.

(iii) The velocity of the dust ion-acoustic waves increases considerably with increasing ϵZ_{d0} .

(iv) In experiments with a double plasma device, Nakamura *et al.* [3] revealed that the most important feature of ion acoustic waves in a dusty plasma is the following. In the absence of dust, the effect of the electron and ion charge separation gives rise to oscillations in the shock wave profile in the vicinity of the shock front, while the presence of dust suppresses these oscillations.

Hence, in order for a theoretical model to adequately describe shock-wave structures in dusty plasmas, it should be capable of explaining the above main properties of shock waves under the conditions of the relevant experiments. For this purpose, we modify the so-called ionization source model [4, 5] in the following way. In [4, 5], the ionization source term was chosen to correspond to conventional electron impact ionization of neutrals (as is traditionally done in describing dusty plasmas) and, accordingly, was proportional to the electron density. However, in the laboratory experiments of [2], a hot (~2000–2500 K) plate installed in the end region of the machine was irradiated with a beam of cesium atoms, so that cesium ions in the plasma were produced through ionization of cesium atoms at the plate surface. In the experiments of [3], the electron mean free paths were so long that the neutrals were ionized presumably in collisions with the wall. Thus, under the experimental conditions of [3] [the partial pressure of a neutral gas (argon) is $(3-6) \times 10^{-4}$ torr and the electron temperature is $T_e = 0.1$ eV], the electron mean free path with respect to electron–neutral collisions is on the order of 10^4 cm, which is much larger than the length of the device (90 cm) and its diameter (40 cm) [6]. Consequently, under the experimental conditions of [2, 3], the ionization source term in the evolutionary equation for the ion density should be independent of the electron density. Additionally, in contrast to the model of [4, 5], we take into account the effect of the gas-kinetic ion pressure on the evolution of the dusty plasma.

Hence, in planar geometry, the evolution of a perturbation and its transformation to a nonlinear wave structure are described by a set of nonlinear equations that differs somewhat from the set presented in [4, 5] and consists of the following equations:

(a) The evolutionary equations for the ions,

$$\partial_t n_i + \partial_x (n_i v_i) = -v_{\text{ch}} n_i + S_i, \quad (2)$$

$$\begin{aligned} & \partial_t (n_i v_i) + \partial_x (n_i v_i^2) \\ &= -\frac{en_i}{m_i} \partial_x \phi - \frac{T_i}{m_i} \partial_x n_i - \tilde{v} n_{0i} v_i, \end{aligned} \quad (3)$$

and a Boltzmann distribution for the electrons,

$$n_e = n_{e0} \exp\left(\frac{e\phi}{T_e}\right). \quad (4)$$

Here, v_i is the ion velocity, n_e is the electron density, S_i is the ionization source intensity (its value is chosen so that it exactly cancels the term describing the absorption of ions by dust grains in an unperturbed dusty plasma), ϕ is the electrostatic potential, the rate v_{ch} at which the ions are absorbed by the dust grains is equal to

$$v_{\text{ch}} = v_q \frac{Z_{d0} d}{1 + Z_{d0} d} \frac{(T_i/T_e + z_0)}{z_0(1 + T_i/T_e + z_0)}, \quad (5)$$

$d = n_{d0}/n_{e0}$, the rate \tilde{v} at which the ions lose their momentum as a result of their absorption on the grain surfaces and their Coulomb collisions with the grains has the form

$$\begin{aligned} \tilde{v} &= v_q \frac{Z_{d0} d}{(1 + Z_{d0} d) z_0 (1 + T_i/T_e + z_0)} \\ &\times \left(z_0 + \frac{4T_i}{3T_e} + \frac{2z_0^2 T_e}{3T_i} \Lambda \right), \end{aligned} \quad (6)$$

$\Lambda = \ln(\lambda_{Di}/\max\{a, b\})$ is the Coulomb logarithm, λ_{Di} is the ion Debye radius, and $b = Z_{d0} e^2/T_i$. Expressions (5) and (6) are valid in the range $v_i/c_s < 1$;

(b) Poisson's equation for the electrostatic potential,

$$\partial_{xx} \phi = 4\pi e (n_e + Z_d n_d - n_i); \quad (7)$$

(c) The evolutionary equation for the dust grain charge,

$$\partial_t q_d = I_e(q_d) + I_i(q_d). \quad (8)$$

Here, the electron and ion microscopic currents to the grain surface, $I_e(q_d)$ and $I_i(q_d)$, are represented as

$$I_e \approx -\pi a^2 e \left(\frac{8T_e}{\pi m_e} \right)^{1/2} n_e \exp\left(\frac{eq_d}{aT_e}\right), \quad (9)$$

$$\begin{aligned} I_i &= \sqrt{\frac{\pi}{2}} a^2 v_{Ti} e n_i \left[2 \exp\left(-\frac{v_i^2}{2v_{Ti}^2}\right) \right. \\ &\left. + \sqrt{2\pi} \frac{v_{Ti}}{v_i} \left(1 + \frac{v_i^2}{v_{Ti}^2} - \frac{2eq_d}{am_i v_{Ti}^2} \right) \text{erf}\left(\frac{v_i}{\sqrt{2}v_{Ti}}\right) \right], \end{aligned} \quad (10)$$

where m_e is the mass of an electron and $\text{erf}(x)$ is the error function.

Below, the agreement of the conclusions of the theory developed here with the main experimental results (i)–(iv) will be tested by comparing the theoretical predictions from Eqs. (2)–(10) with the experimental data of [2, 3]. Note that Nakamura *et al.* [3] attempted to describe their experimental results on the basis of the Korteweg–de Vries–Burgers (KdVB) equation with the dissipative viscosity coefficient proportional to the ion–grain collision rate (see also [3, 7]). However, in a classical approach to describing dusty plasmas (see, e.g., [8]) by Eq. (8) for dust grain charging, it is impossible

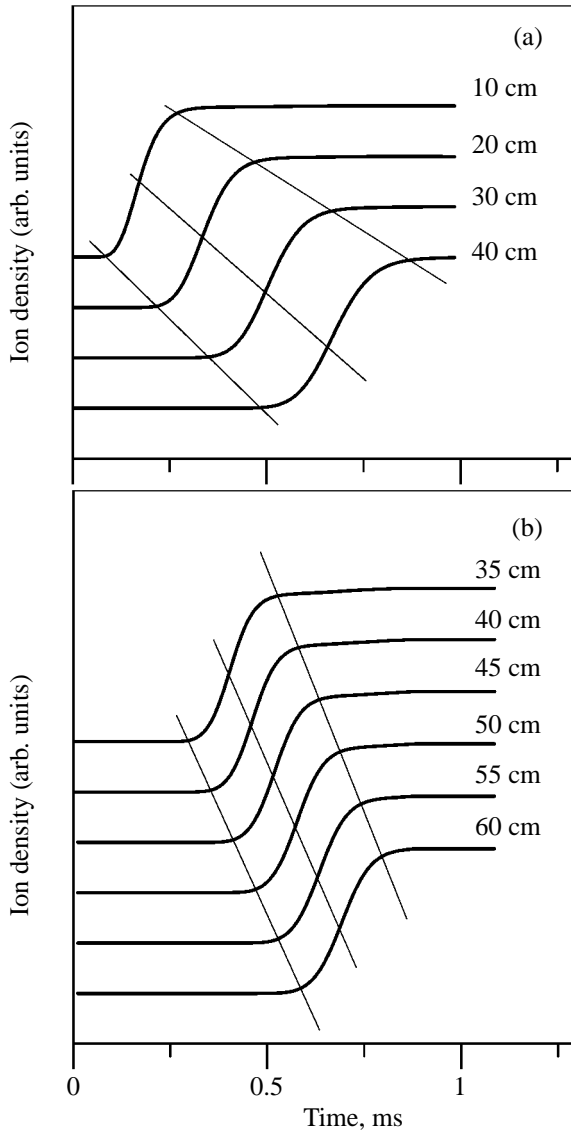


Fig. 1. Time evolutions of the ion density (heavy curves) at different distances from the grid for $\epsilon Z_{d0} =$ (a) 0 and (b) 0.75. The remaining parameters of the plasma and of the perturbation are as follows: $T_e = T_i = 0.2$ eV, $n_{i0} = 1.024 \times 10^7$ cm $^{-3}$, $a = 0.1$ μ m, $\Delta x = 25$ cm, and $\Delta n_i/n_{i0} = 2$. The light curves show the widening of the wave front (at $\epsilon Z_{d0} = 0$) and its steepening (at $\epsilon Z_{d0} = 0.75$), which agrees with the experimental data of [2].

to derive the general hydrodynamic equation that describes the evolution of the ion momentum and contains the viscosity term in conventional hydrodynamic form (the KdVB equation used in [3, 7] was derived precisely from this general equation).

Now, we test our theoretical model against the experimental results (i)–(iii), which were obtained in [2]. To do this, we use Eqs. (2)–(10) to trace the evolution of a rectangular initial perturbation in the ion density profile under the conditions of those experiments.

In [2], the experiments were carried on a Q-machine modified so that the dust component of the plasma would be easier to produce. The parameters of the dusty plasma were as follows: $T_e \approx T_i \approx 0.2$ eV, $n_{i0} \sim 10^6$ – 10^7 cm $^{-3}$, and $a \sim 0.1$ – 1 μ m. The parameter $\epsilon Z_{d0} = n_{d0} Z_{d0}/n_{i0}$ ranged between 0 and 0.95. A study was made of the evolution of a rectangular perturbation in the initial ion density profile. The perturbation was initiated by a grid held at an electrostatic potential of about -6 V with respect to the potential of the hot plate.¹ The width of the initial perturbation was about 25 cm.

We have already mentioned that, in the experiments of [2], a cesium vapor plasma (containing Cs $^+$ ions) was created through surface ionization. In other words, a cesium atom striking the hot plate becomes ionized. The newly produced cesium ion flies away from the plate at a certain directed velocity. Hence, we can expect the ion flux to be generated in the immediate vicinity of the plate. The intensity of the ion flux and its density are strongly sensitive to the plate temperature. In calculations, this dependence was modeled by imposing the corresponding boundary condition at the surface of the hot plate (analogous to the related boundary condition in the surface evaporation problem [9]) under the following assumptions:

(a) at the plate surface, not only are the atoms ionized, but also the inverse process takes place—surface recombination of the ions that strike the plate;

(b) all the ions striking the plate recombine;

(c) at the initial instant (just before the perturbation starts evolving), the ionization and recombination processes are in dynamic equilibrium; i.e., the ion gas temperature is equal to the plate temperature and the intensity of the flux of the ions that strike the plate and recombine is the same as the intensity of the flux of the ions that fly away from the plate surface; and

(d) the ions flying away from the plate obey a Maxwellian distribution function with a temperature T_i equal to the plate temperature, the directed ion velocity is zero, and the ion density is always equal to the initial density of the ion gas.

During the evolution of the initial perturbation, the ions in the vicinity of the plate acquire a directed velocity v_i , so that the ion density n_i changes. The directed ion velocity and ion density are calculated from the conservation conditions for the ion flux from the plate surface and ion momentum flux. As at the initial instant, the ions are assumed to obey a Maxwellian distribution function, which now corresponds to a nonzero directed ion velocity and an ion density different from the initial ion density near the plate surface.

Our calculations were based on the computational method developed in [5] in order to investigate the evolution of the initial perturbation in a dusty plasma with variable-charge dust grains. We used the following val-

¹ R.L. Merlino, private communication (2001).

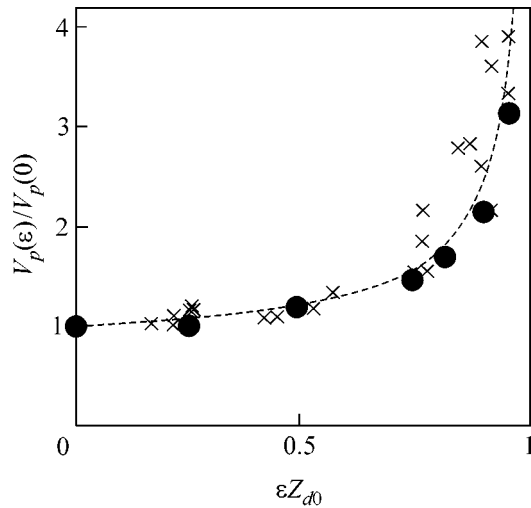


Fig. 2. Dependence of the perturbation front velocity (normalized to its value in the absence of dust) on εZ_{d0} . The crosses refer to the experimental points obtained in [2] and the calculated results are represented by the closed circles.

ues of the plasma parameters: the electron and ion temperatures were equal to one another, $T_e = T_i = 0.2$ eV; the background ion density $n_{i0} = 1.024 \times 10^7$ cm $^{-3}$ was the same for all series of simulations; the grain radius was $a = 0.1$ μ m; the width of the rectangular initial perturbation was $\Delta x = 25$ cm; and the excess initial perturbed ion density above the background ion density in the remaining unperturbed plasma was $\Delta n_i/n_{i0} = 2$ (see Fig. 2 in [2]). The calculations were carried out for different values of the parameter εZ_{d0} .

In Fig. 1 (which is analogous to Fig. 2 from [2]), we illustrate the time evolution of the ion density at different distances from the grid. The time evolutions (heavy curves) were calculated for $\varepsilon Z_{d0} =$ (a) 0 and (b) 0.75. The light curves show the widening of the wave front (at $\varepsilon Z_{d0} = 0$) and its steepening (at $\varepsilon Z_{d0} = 0.75$). This agrees with the experimental data from [2]. Note that it is the above boundary condition that allowed us to numerically capture the effect of the widening of the wave front in the absence of dust.

The extent to which the shock front widens was calculated to be $\Delta \xi/Mc_s \sim 0.3$ ms (see Fig. 1b), which corresponds to that observed experimentally (see Fig. 2b in [2]) and also to estimate (1), obtained using the theoretical model of [1].

The initial perturbation evolves in such a way that its front velocity V_p becomes nearly constant about 1 ms after it starts propagating through the background plasma. Figure 2 shows the dependence of the perturbation front velocity (normalized to its value in the absence of dust, $\varepsilon = 0$) on the parameter εZ_{d0} . For comparison, we also plot the experimental points (crosses) taken from Fig. 5 in [2]. The calculated results are rep-

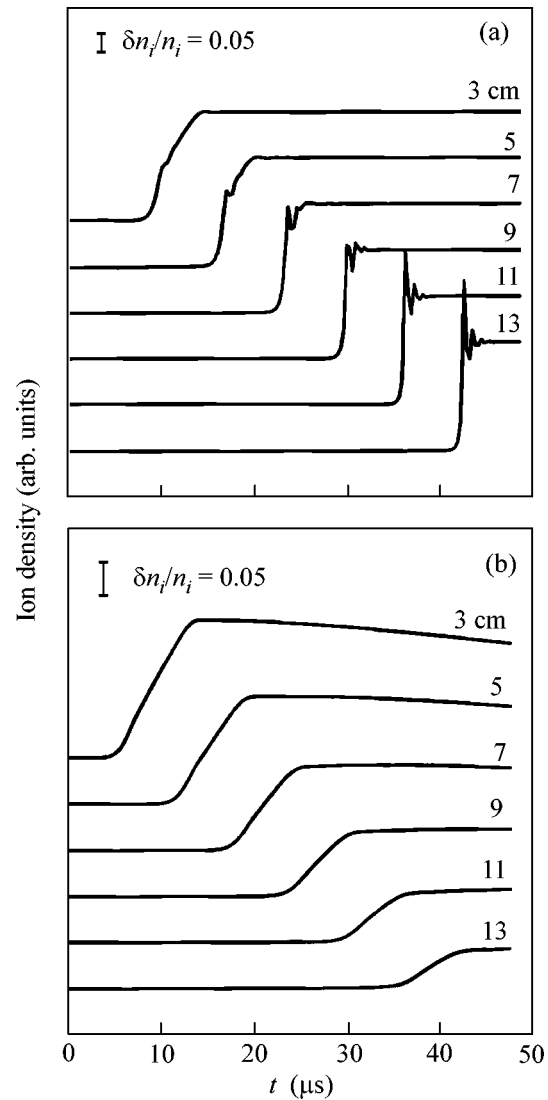


Fig. 3. Time evolutions of the ion density at different distances from the grid for $n_{d0} =$ (a) 0 and (b) 1.46×10^4 cm $^{-3}$. The remaining plasma parameters are as follows: $T_e = T_i = 1.5$ eV, $n_{i0} = 2.3 \times 10^8$ cm $^{-3}$, and $a = 4.4$ μ m. Like in the experiments of [3], the oscillations in the shock wave profile that are caused by the electron and ion charge separation are suppressed by the dust.

resented by closed circles. The agreement between theory and experiment is quite good.

Now, we test our theoretical model against the experimental result (iv), which was obtained in [3]. The experiments described in that paper were carried out with a double plasma device, which was modified so that the dust component was present in the plasma. The parameters of the dusty plasma were as follows: $T_e \approx 1$ – 1.5 eV, $T_i < 0.1$ eV, $n_{e0} \sim 10^8$ – 10^9 cm $^{-3}$, and $a \approx 4.4$ μ m. The unperturbed dust density n_{d0} was varied from 0 to about $\sim 10^5$ cm $^{-3}$. Dust ion-acoustic shock waves were excited by applying a triangular voltage pulse with a

peak amplitude of 2.0 V and a rise time of about 10 μ s to the driver anode.

The calculations were carried out for different dust densities and for the following parameter values: $T_e = T_i = 1.5$ eV, $n_{i0} = 2.3 \times 10^8$ cm $^{-3}$ (the ion background density was the same for all series of simulations), and $a = 4.4$ μ m. The width of the perturbation ($\Delta x \approx 20$ cm) and its shape were determined self-consistently, in accordance with the method for exciting a shock wave. It should be noted that Nakamura and Bailung [6] compared the theoretical and experimental potential differences between the grains and the plasma under essentially the same conditions as those prevailing in the experiments of [3]. They found that, although the ion temperature in those experiments was significantly lower than the electron temperature ($T_i \ll T_e$), the experimental results were best fitted by the curve calculated for $T_i = T_e$. They attributed this circumstance to the possible ion acceleration to energies comparable to the electron energy. That is why, in our calculations, the values of the electron (T_e) and ion (T_i) temperatures were taken to be the same.

In Fig. 3 (which is analogous to Fig. 3 from [3]), we illustrate the time evolution of the ion density at different distances from the grid. The time evolutions were calculated for (a) $n_{d0} = 0$ (the electron density being $n_{e0} = 2.3 \times 10^8$ cm $^{-3}$) and (b) $n_{d0} = 1.46 \times 10^4$ cm $^{-3}$ (the electron density being $n_{e0} = 4.6 \times 10^8$ cm $^{-3}$). We can see that the electron and ion charge separation gives rise to oscillations in the shock wave profile and that the dust suppresses these oscillations, as is the case in the experiments of [3]. The theoretically calculated rise time of the shock front is about 5 μ s, which corresponds to the experimental data.

Hence, the theoretical model developed here makes it possible to describe all the main experimental results on dust ion-acoustic shock waves. A further develop-

ment of the model and refinement of the results involve an account of the effects of dust density nonuniformity in experimental devices. Also, we plan to compare theoretical predictions from our model with the data from laboratory experiments on ion acoustic solitons in a dusty plasma that were carried out at the Institute of Space and Astronautical Science (Japan) [10].

We are grateful to R.L. Merlino and Y. Nakamura for fruitful discussions of this study. This work was supported by INTAS (grant no. 97-2149) and INTAS-RFBR (grant no. IR-97-775). S.I. Popel is grateful to the Alexander von Humboldt Foundation for support.

REFERENCES

1. S. I. Popel, M. Y. Yu, and V. N. Tsytovich, *Phys. Plasmas* **3**, 4313 (1996).
2. Q.-Z. Luo, N. D'Angelo, and R. L. Merlino, *Phys. Plasmas* **6**, 3455 (1999).
3. Y. Nakamura, H. Bailung, and P. K. Shukla, *Phys. Rev. Lett.* **83**, 1602 (1999).
4. S. I. Popel, A. P. Golub', T. V. Losseva, and R. Bingham, *Pis'ma Zh. Éksp. Teor. Fiz.* **73**, 258 (2001) [*JETP Lett.* **73**, 223 (2001)].
5. S. I. Popel, A. P. Golub', T. V. Losseva, *et al.*, *Phys. Plasmas* **8**, 1497 (2001).
6. Y. Nakamura and H. Bailung, *Rev. Sci. Instrum.* **70**, 2345 (1999).
7. P. K. Shukla, *Phys. Plasmas* **7**, 1044 (2000).
8. V. N. Tsytovich, *Usp. Fiz. Nauk* **167**, 57 (1997) [*Phys. Usp.* **40**, 53 (1997)].
9. O. Knacke and I. N. Stranski, *Usp. Fiz. Nauk* **68**, 261 (1959); *Prog. Met. Phys.* **6**, 181 (1956).
10. Y. Nakamura and A. Sarma, *Phys. Plasmas* **8**, 3921 (2001).

Translated by O. Khadin

Numerical Modeling of Collapse in Ideal Incompressible Hydrodynamics

V. A. Zheligovsky, E. A. Kuznetsov,* and O. M. Podvigina

International Institute of the Theory of Earthquake Forecasting and Mathematical Geophysics, Russian Academy of Sciences, Moscow, 113556 Russia

* *Landau Institute for Theoretical Physics, Russian Academy of Sciences, Moscow, 117334 Russia*

Received August 24, 2001

The appearance of a singularity in the velocity-field vorticity $\boldsymbol{\omega}$ at an isolated point irrespective of the symmetry of initial distribution is demonstrated numerically. The behavior of maximal vorticity $|\boldsymbol{\omega}|$ near the collapse point is well approximated by the dependence $(t_0 - t)^{-1}$, where t_0 is the collapse time. This is consistent with the interpretation of collapse as the breaking of vortex lines. © 2001 MAIK “Nauka/Interperiodica”.

PACS numbers: 47.15.Ki; 47.32.Cc

1. The problem of collapse in hydrodynamics, i.e., of a process of formation of a singularity in finite time is the key problem for the understanding of the physical origin of developed turbulence. In spite of a certain progress in developing the statistical theory of Kolmogorov spectra in the diagrammatic or functional approaches (see [1] and references therein), the question of whether the Kolmogorov spectrum [2] is a solution to the statistical equations is still open. There is another unsolved important problem of intermittency, which is statistically treated as the existence of a strongly non-Gaussian distribution of turbulent velocity leading to the deviation of the indices of higher correlation functions from the Kolmogorov value [3]. The deviation from the Gaussian distribution gives rise to the nonzero odd correlation functions, which testifies to the strong correlations suggesting the presence of coherent structures in turbulence. Numerical and experimental data indicate (see [3] and references therein) that vorticity in the regime of developed turbulence shows a strongly nonuniform distribution in space and concentrates in quite small areas. What is the origin of the high vorticity concentration? Can it be attributed to collapse, i.e., to the appearance of singularities in vorticity? If so, how can the Kolmogorov spectrum be obtained from this fact? The latter question is not rhetorical, because it is well known that each singularity gives rise to power tails in the spectrum. Therefore, the problem of collapse is a fundamental one in hydrodynamics.

The most popular object for studying collapse in hydrodynamics is a system of two antiparallel vortex tubes with continuously distributed vorticity [4] or, in a more general formulation, flows with high symmetry [5]. As is known, two antiparallel vortex filaments are subject to so-called Crow instability that leads to the stretching of vortex filaments in the direction normal to

the plane of the initial distribution of vortices and to a decrease in the distances between them. Numerical experiments [4] indicate that, at the nonlinear stage of developing this instability, pointlike vorticity singularities are formed in the core of each vortex tube as $|\boldsymbol{\omega}|$ increases near the collapse point following the $(t_0 - t)^{-1}$ law, where t_0 is the time of singularity formation (see also [6]).

2. In this paper, the results of numerical experiment are presented which can be interpreted as the appearance of a singularity in the $\boldsymbol{\omega}(\mathbf{r})$ field at single point in three-dimensional ideal hydrodynamics with the initial data having no definite symmetry. Our approach is based on the representation of the equation for vorticity $\boldsymbol{\omega}(\mathbf{r}, t)$ in terms of vortex lines introduced in [7]

$$\boldsymbol{\omega}(\mathbf{r}, t) = (\boldsymbol{\omega}_0(\mathbf{a}) \cdot \nabla_{\mathbf{a}}) \mathbf{R}(\mathbf{a}, t) / J. \quad (1)$$

Here,

$$\mathbf{r} = \mathbf{R}(\mathbf{a}, t) \quad (2)$$

is the mapping onto the curvilinear coordinate system associated with the vortex lines so that $\mathbf{b} = (\boldsymbol{\omega}_0(\mathbf{a}) \cdot \nabla_{\mathbf{a}}) \mathbf{R}(\mathbf{a}, t)$ is the vector tangent to the vortex line and $J = \det \|\partial \mathbf{R} / \partial \mathbf{a}\|$ is the Jacobian of mapping (2). The dynamics of the vector $\mathbf{R}(\mathbf{a}, t)$ is governed by the equation

$$\partial_t \mathbf{R} = \hat{\Pi} \mathbf{v}(\mathbf{R}, t), \quad (3)$$

where $\mathbf{v}(\mathbf{r}, t)$ is the fluid velocity at the point $\mathbf{r} = \mathbf{R}$ and $\hat{\Pi}$ is the transverse projector to a given vortex line at this point:

$$\Pi_{\alpha\beta} = \delta_{\alpha\beta} - \xi_{\alpha} \xi_{\beta}, \quad \xi = \mathbf{b} / |\mathbf{b}|.$$

Equations (1)–(3) are closed by the relations

$$\boldsymbol{\omega}(\mathbf{r}, t) = \text{curl} \mathbf{v}(\mathbf{r}, t), \quad \text{div} \mathbf{v} = 0. \quad (4)$$

The set of Eqs. (1)–(4) results from the partial integration of the forceless Euler equation

$$\partial_t \boldsymbol{\omega} = \text{curl}[\mathbf{v} \times \boldsymbol{\omega}], \quad \text{div} \mathbf{v} = 0. \quad (5)$$

The vector field $\boldsymbol{\omega}_0(\mathbf{a})$ ($\text{div}_{\mathbf{a}} \boldsymbol{\omega}(\mathbf{a}) = 0$) entering Eq. (1) is a Cauchy invariant characterizing the property of freezing-in vortex lines into the fluid; in particular,

$$\boldsymbol{\omega}_0(\mathbf{a}) = \boldsymbol{\omega}(\mathbf{r}, 0) \text{ for } \mathbf{R}(\mathbf{a}, 0) = \mathbf{a}. \quad (6)$$

As was mentioned in [7, 8], the Jacobian J can take arbitrary values, because this is a mixed Lagrange–Euler description. In particular, J can be zero at a certain point, which means, according to Eq. (1), the appearance of a vorticity singularity. The possibility of such a singularity to appear was demonstrated in [8] for the three-dimensional integrable hydrodynamic equation that relates to the same type of equations as the Euler Eq. (5) but differs from it in the way of matching the (generalized) vorticity and velocity: $\mathbf{v} = \text{curl}(\delta \mathcal{H} / \delta \boldsymbol{\omega})$, $\mathcal{H} = \int |\boldsymbol{\omega}| d\mathbf{r}$.

The appearance of a singularity in vorticity at $J = 0$ implies that one vortex line touches another at a certain point (collapse point). This process is nothing more than the breaking of vortex lines. It is completely characterized by mapping (2), and it is similar to the breaking of dust gas (in the absence of pressure).

3. We assume that collapse in the Euler hydrodynamics arises due to the breaking of vortex lines. Let $t = \tilde{t}(\mathbf{a}) > 0$ be a solution to the equation $J(\mathbf{a}, t) = 0$ and $t_0 = \min_{\mathbf{a}} \tilde{t}(\mathbf{a})$. In this case, the Jacobian J near the minimum point $t = t_0$ and $\mathbf{a} = \mathbf{a}_0$ can be expanded at the generic point as (cf. [8])

$$J = \alpha(t_0 - t) + \gamma_{ij} \Delta a_i \Delta a_j + \dots, \quad (7)$$

where $\alpha > 0$, γ is a positively definite matrix, and $\Delta \mathbf{a} = \mathbf{a} - \mathbf{a}_0$. Expansion (7) is valid if J is an analytic function, which is natural to assume until the singularity arises. In this case, the numerator (vector \mathbf{b}) in Eq. (1) should be nonzero because the condition $J = 0$ for the generic point means that three vectors $\partial \mathbf{R} / \partial a_i$ ($i = 1, 2, 3$) are coplanar but no one of them is zero (otherwise there would be degeneration). At the same time, the equality $J = 0$ in the nondegenerate case implies that one (λ_1) of the eigenvalues of the Jacobi matrix is zero, whereas two other eigenvalues ($\lambda_{2,3}$) are nonzero. Therefore, three directions arise in this problem: one soft direction corresponding to λ_1 and two hard directions corresponding to $\lambda_{2,3}$. As is seen from Eq. (7), the self-similarity $\Delta \mathbf{a} \sim \sqrt{\tau}$ [where $\tau = \alpha(t_0 - t)$ in the auxiliary \mathbf{a} space is identical in all directions. However, as was shown in [8], in the physical space (where the behavior of $\boldsymbol{\omega}$ near the breaking point is the same for the integrable hydrodynamics and the Euler equation), contraction $X_1 \sim \tau^{3/2}$ arises along the soft direction, while $X_{\perp} \sim \tau^{1/2}$ along the two other (hard) directions. As a result, $\boldsymbol{\omega}$ near

the singularity concentrates in a strongly flattened pancake-shaped region

$$\boldsymbol{\omega} = \tau^{-1} \mathbf{g}(\zeta_1, \zeta_{\perp}), \quad \zeta_1 = X_1 \tau^{-3/2}, \quad \zeta_{\perp} = X_{\perp} \tau^{-1/2}. \quad (8)$$

In this case, the vector $\boldsymbol{\omega}$ lies in the pancake plane.

The above analysis is, in essence, based on the behavior of the mapping near a fold and, in this regard, completely fits in the catastrophe theory [9]. In this case, the use of vortex-line representation (1) allows the description of the *incompressible* vector field $\boldsymbol{\omega}(\mathbf{r}, t)$ near the singular point.

4. According to the existing classification of collapses [10], the breaking of vortex lines should be assigned to superweak collapses rather than to weak ones, because the contribution coming from the singularity to enstrophy $I = \int |\boldsymbol{\omega}|^2 d\mathbf{r}$ and characterizing the viscosity-induced dissipation rate is small ($\sim \tau^{1/2}$). In this case, the contribution to the energy is proportional to $\tau^{3/2}$. At the same time, the integral $\int (\nabla \boldsymbol{\omega})^2 d\mathbf{r}$ diverges at $t \rightarrow t_0$. Therefore, in the presence of breaking, the solution $\mathbf{v} = \mathbf{v}(\mathbf{r}, t)$ at $t \geq t_0$ cannot be continued in the Sobolev space $H^2(\mathcal{R}^3)$ with norm $(\sum_{q \leq 2} \int (\nabla^q f)^2 d\mathbf{r})^{1/2}$. According to the theorem proved in [11], this is sufficient for the integral $\int_0^{t_0} \sup_{\mathbf{r}} |\boldsymbol{\omega}| dt = \infty$ to diverge. This criterion, being necessary and sufficient for the collapse, is satisfied for Eq. (8). Another restriction follows from the theorem [12] on the vorticity sense. According to this theorem, the collapse is absent for all $t \in [0, t_0]$ if

$$\int_0^{t_0} \sup |\nabla \xi|^2 dt < \infty, \quad (9)$$

where supremum is taken over a certain region A near the maximum $\boldsymbol{\omega}$ value. The presence of collapse implies that integral (9) diverges at $\tau \rightarrow 0$. Accordingly, the quantity $|\nabla \xi|$ should behave at least as $\tau^{-1/2}$. Evidently, since $\partial \xi / \partial X_{\omega} = 0$, the derivative $\partial \xi / \partial X_{\omega}$ in the pancake plane should either be nonsingular in the direction of vector $\boldsymbol{\omega}$ at distances on the order of $\tau^{1/2}$ and larger or have a singularity weaker than $\tau^{-1/2}$. However, this does not exclude the presence of large gradients of the vector ξ outside the pancake region in the soft direction, e.g., with the behavior $\sup |\partial \xi / \partial X_1| \sim \tau^{-\alpha}$, where $1/2 \leq \alpha < 3/2$. Such a behavior seems to be natural, because the region near the breaking point contracts appreciably when passing from the \mathbf{a} space to the physical space. Therefore, one can conclude that at least three scales— $l_1 \sim \tau^{3/2}$, $l_{\perp} \sim \tau^{1/2}$, and $l_{\text{in}} \sim \tau^{\alpha}$ with $1/2 < \alpha < 3/2$ —must exist in the presence of breaking. The latter scale must ensure the applicability of the theorem [12].

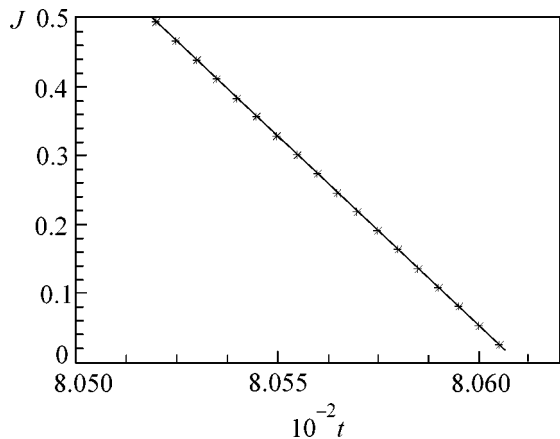


Fig. 1. Minimum (in space) of the $|\omega|^{-1}$ vs. time t as the collapse time is approached.

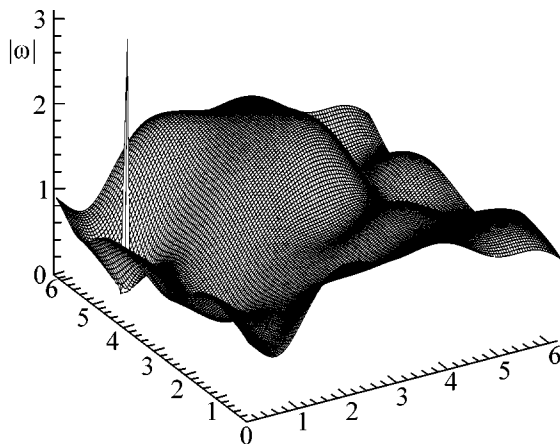


Fig. 2. The quantity $|\omega|$ vs. the coordinates R_1 and R_3 at the $a_2 = \text{const}$ surface passing through the point of J minimum as the collapse is approached ($t = 0.08055$).

5. To verify the above hypothesis, a numerical experiment was carried out on a 128^3 grid for the set of Eqs. (1)–(4). Two indicative features of this set are noteworthy.

First, in contrast to the Euler equation, which has an infinite number of the integrals of motion (Cauchy invariants), the set of Eqs. (1)–(4), being a partially integrated Euler equation, involves the Cauchy invariants in an explicit form. Therefore, this set can be numerically integrated without taking care of their conservation, whereas the numerical integration of the Euler equation itself requires control of the degree of conservation of these invariants, particularly for the collapse problem.

Second, this set allows one to separate the integration of Eq. (3) with respect to time from the integration

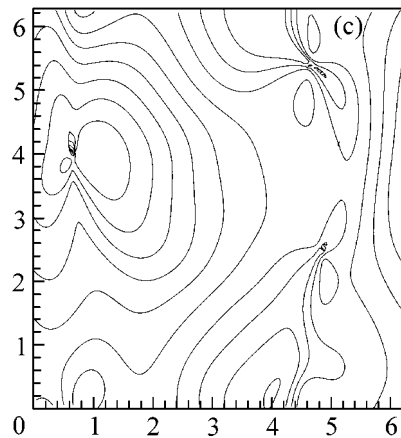
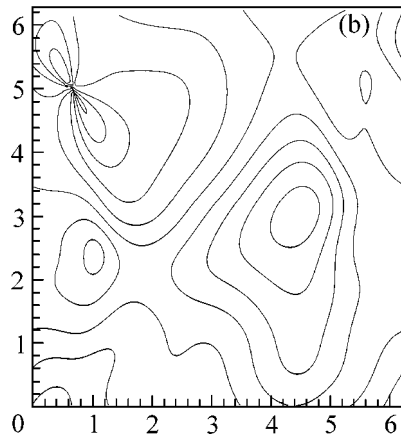
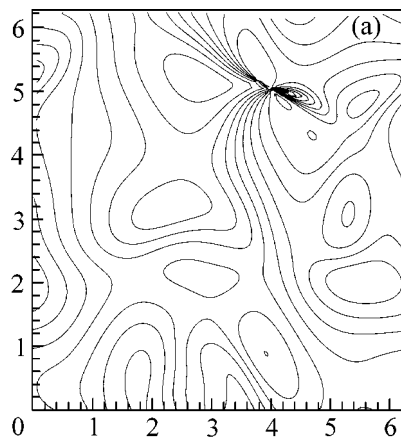


Fig. 3. Contour maps of the function $R_i(a_j, a_k)$, $i \neq j \neq k$, specifying the surface mapping (2) the plane $a_i = \text{const}$ and passing through the point of J minimum; $i =$ (a) 1, (b) 2, (c) 3. [Collapse occurs at the point $\mathbf{R}(\mathbf{a}, t_0)$ with $\mathbf{a} = (7\pi/32; 41\pi/32; 13\pi/8)$.]

of Eq. (4) with respect to spatial variables (inversion of the curl operator). The set of Eqs. (1)–(4) was analyzed with periodic boundary conditions, and the curl operator was inverted by the standard fast Fourier transform method. The most difficult stage in the numerical inte-

gration of Eqs. (1)–(4) was associated with the transition (direct and inverse) from the \mathbf{R} to \mathbf{a} variables. This difficulty was bypassed by using two independent grids for the \mathbf{R} variables: one of them moves according to Eq. (3) and the other is a stationary regular grid geometrically identical with the grid of \mathbf{a} variables. The computation algorithm includes the following steps: (i) new positions of the moving \mathbf{R} grid points are determined by integrating Eq. (3) with respect to time; (ii) the $\boldsymbol{\omega}$ values on the moving \mathbf{R} grid are calculated from Eq. (1) by the finite-difference technique; (iii) the $\boldsymbol{\omega}$ values on the regular \mathbf{R} grid are calculated by linear interpolation from the nearest neighbors (for each point of this grid, the corresponding tetrahedron with vertices at the nearest points of the moving \mathbf{R} grid is preliminarily found); (iv) the velocity \mathbf{v} on the regular \mathbf{R} grid is determined from Eq. (4); (v) the velocity \mathbf{v} on the moving \mathbf{R} grid is determined by linear interpolation (to do this, it is convenient to treat an elementary cube of the regular \mathbf{R} grid as a combination of tetrahedrons with vertices at vertices, face centers, and the center of the elementary cube).

The initial vorticity distribution was taken in the form of a solenoidal field with random Fourier harmonics and an exponentially decaying spectrum cut off at a wavenumber eight, with $\boldsymbol{\omega}_0 \neq 0$ over the entire periodicity cube. The vorticity field thus specified initially had no symmetry. The computation was carried out controlling the energy conservation; it was constant to 1% over the entire integration interval. For these initial conditions, the appearance of an $|\boldsymbol{\omega}|$ peak at a *single* point was observed. At this point, the Jacobian J was minimal (in space) and decreased linearly with high accuracy as a function of time (Fig. 1). During the computation time, the $|\boldsymbol{\omega}|$ maximum increased almost by a factor of 20 and the peak width was equal to three grid-point spacings (strong $|\boldsymbol{\omega}|$ localization at the collapse point is seen in Fig. 2).

To verify that this process can be treated as the breaking of vortex lines, we calculated the time-dependent second-derivative tensor $\partial^2 J / \partial a_\alpha \partial a_\beta = 2\gamma_{\alpha\beta}$ for the Jacobian at the J minimum. We did not find sizable changes in this quantity when the J minimum as a function of time approached its linear asymptotic behavior; this qualitatively agrees with Eq. (7). The final dis-

placement of vortex lines in the vicinity of the collapse point is illustrated in Fig. 3. The spatial distribution of $|\boldsymbol{\omega}(\mathbf{r}, t)|$ near the maximum shows certain anisotropy. However, we cannot state that two *substantially* different scales arise because of the lack of spatial resolution.

Thus, the results of this work can be interpreted as the first numerical observation of the breaking of vortex lines. The collapse is numerically found in the absence of any symmetry in the initial distribution and arises at a single point.

6. The work of E.A.K. was supported by the Russian Foundation for Basic Research (project no. 00-01-00929), the Leading Russian Scientific Schools (project no. 00-15-96007), and the INTAS (grant no. 00-00292).

REFERENCES

1. A. S. Monin and A. M. Yaglom, *Statistical Fluid Mechanics: Mechanics of Turbulence* (Gidrometeoizdat, St. Petersburg, 1996, 2nd ed.; MIT Press, Cambridge, 1975), Vol. 2; V. S. L'vov, Phys. Rep. **257**, 1 (1991).
2. A. N. Kolmogorov, Dokl. Akad. Nauk SSSR **30**, 9 (1941).
3. U. Frisch, *Turbulence. The Legacy of A. N. Kolmogorov* (Cambridge Univ. Press, Cambridge, 1995).
4. R. M. Kerr, Phys. Fluids A **4**, 2845 (1993).
5. R. B. Pelz, Phys. Rev. E **55**, 1617 (1997); O. N. Boratav and R. B. Pelz, Phys. Fluids **6**, 2757 (1994).
6. R. Grauer, C. Marliani, and K. Germaschewski, Phys. Rev. Lett. **80**, 4177 (1998).
7. E. A. Kuznetsov and V. P. Ruban, Pis'ma Zh. Éksp. Teor. Fiz. **67**, 1015 (1998) [JETP Lett. **67**, 1076 (1998)].
8. E. A. Kuznetsov and V. P. Ruban, Zh. Éksp. Teor. Fiz. **118**, 853 (2000) [JETP **91**, 775 (2000)].
9. V. I. Arnold, *Catastrophe Theory* (Znanie, Moscow, 1981; Springer-Verlag, Berlin, 1986).
10. V. E. Zakharov and E. A. Kuznetsov, Zh. Éksp. Teor. Fiz. **91**, 1310 (1986) [Sov. Phys. JETP **64**, 773 (1986)].
11. J. T. Beals, T. Kato, and A. J. Majda, Commun. Math. Phys. **94**, 61 (1984).
12. P. Constantin, Ch. Feferman, and A. J. Majda, Commun. Partial Diff. Eqns. **21**, 559 (1996).

Translated by R. Tyapaev

Trapping, Compression, and Acceleration of an Electron Beam by the Laser Wake Wave

A. G. Khachatryan

Yerevan Physics Institute, Yerevan, 375036 Armenia

Received June 13, 2001; in final form, August 27, 2001

The scheme of laser wake-field acceleration in plasma is proposed and considered for the case where a relatively rare nonrelativistic or weakly relativistic electron beam is initially situated ahead of the intense laser pulse. It is shown that an electron beam is trapped in the region of the first accelerating wake maximum; then it is strongly compressed and accelerated to ultrarelativistic energies. © 2001 MAIK "Nauka/Interperiodica".

PACS numbers: 41.75.Jv; 52.35.Mw; 52.75.Di

1. Plasma wake waves (WWs) excited by intense laser pulses or relativistic electron bunches may produce extraordinarily strong accelerating and focusing fields. The theoretical and experimental studies have shown that the acceleration rate in a WW may be as high as tens of GeV/m, i.e., three orders of magnitude higher than the rates achieved in conventional accelerators (see review [1] and the bibliography presented therein). At present, plasma methods of acceleration are being intensively developed.

The problem of injection of an accelerated bunch into the accelerating WW phase is among the key problems of laser wake-field acceleration (LWFA) (see, e.g., [2] and references cited therein). The previous injection methods were aimed at producing short (of a length much shorter than the plasma wavelength λ_p) and dense bunches of relativistic electrons and injecting them into the accelerating phase with femtosecond synchronization [2–4]. Both the bunch generation and the femtosecond synchronization encounter serious technological problems.

Diffraction broadening of intense laser pulses limits the interaction length with plasma to a value on the order of Rayleigh length $Z_R = \pi r_0^2 / \lambda_L$ (r_0 is the focal spot radius and λ_L is the laser wavelength), which is ordinarily equal to several millimeters. To prevent or suppress the diffraction spreading of a laser pulse, the plasma channel with a density minimum on its axis is ordinarily used [1, 5]. The amplitude of the accelerating field excited in the plasma channel decreases in wake with distance from the laser pulse [6]. In addition, a radial change in the plasma wavelength $\lambda_p \sim [n_p(r)]^{-1/2}$ [where $n_p(r)$ is the plasma electron density] in the channel leads to phase front curving in WW and field oscillations in the transverse direction, which is highly undesirable from the viewpoint of charged-bunch acceleration. These effects become even stronger with increasing distance from the laser pulse [6]. In the case

of nonlinear WWs, these phenomena also strengthen because of a nonlinear increase in the wavelength with amplitude, the latter being maximal on the axis [7]. Therefore, the first accelerating maximum behind the laser pulse is most preferable for the acceleration of charged particles. Based on this premise and on the above-mentioned injection problems, I propose and consider in this work the LWFA scheme where the nonrelativistic or weakly relativistic electron beam, being initially situated ahead of an intense laser pulse, is trapped, compressed, and accelerated in the region of the first accelerating wake-field maximum. The electron beam length may be much larger, while the density much lower than that required in other injection methods. The proposed LWFA scheme offers the following advantages: (i) there is no need for the injection of a relatively dense short (on the order of several micrometers) relativistic electron bunch into the WW; (ii) there is no need for the femtosecond synchronization of the injected bunch and WW; (iii) efficient compression; and (iiii) energetic separation of the initial electron beam.

2. In this work, I will restrict myself to the one-dimensional theory and a uniform plasma; i.e., the transverse changes in the laser pulse amplitude and plasma density will be ignored. The one-dimensional nonlinear WW excited by a linearly polarized laser pulse is described by the equation (see, e.g., [1])

$$\frac{d^2 \Phi}{d\xi^2} + \beta_g \gamma_g^2 \left\{ 1 - \beta_g \frac{\Phi / (1 + a^2/2)^{1/2}}{[\Phi^2 / (1 + a^2/2) - \gamma_g^{-2}]^{1/2}} \right\} = 0, \quad (1)$$

where $\Phi = 1 + e\psi/m_e c^2$ is the dimensionless potential, $a = eE_0/m_e c\omega_L$, E_0 is the electric field amplitude in the laser pulse, ω_L is the laser frequency, $\xi = k_p(z - v_g t)$, $k_p = \omega_p/v_g$, $\omega_p = (4\pi n_p e^2/m_e)^{1/2}$ is the plasma frequency, v_g is the pulse group velocity (which is equal to the WW phase velocity), $\beta_g = v_g/c$, and $\gamma_g = (1 - \beta_g^2)^{-1/2}$ is

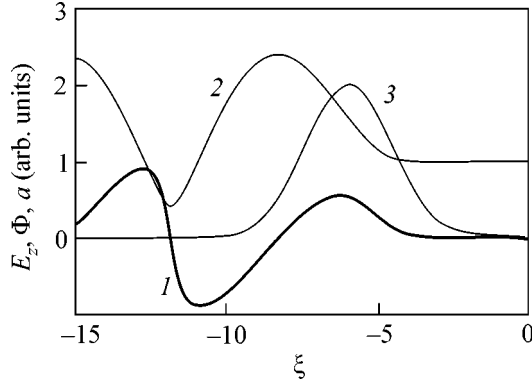


Fig. 1. One-dimensional wake wave excited by a laser pulse with dimensionless peak amplitude $a_0 = 2$. Here (and in all further figures), $\sigma = 2$ and $\gamma_g = 10$. Curve 1 is the electric field $E_z(\xi)$, curve 2 is the wake-field potential $\Phi(\xi)$, and curve 3 is the laser pulse amplitude $a(\xi)$.

the relativistic factor which is approximately equal to ω_L/ω_p at $\gamma_g \gg 1$. The WW electric field normalized to the nonrelativistic wake-breaking field $E_{WB} = m_e v_g \omega_p / e$ can be found from the equation $E_z = -(1/\beta_g^2) d\Phi/d\xi$. The equation of motion for a test electron in the laser pulse field and the WW excited by it can be written in the form

$$\frac{dp}{d\tau} = -\frac{1}{4\beta_g \gamma} \frac{da^2}{d\xi} - \beta_g E_z, \quad (2)$$

where the first term on the right-hand side is the relativistic ponderomotive force averaged over the fast laser oscillations; $\beta = v/c$ and $p = P/m_e c$ are the dimensionless electron velocity and momentum, respectively; $\gamma = (1 + p^2 + a^2/2)^{1/2} = [(1 + a^2/2)/(1 - \beta^2)]^{1/2}$ is the electron relativistic factor; and $\tau = \omega_p t$. Multiplying Eq. (2) by β , one obtains after simple mathematics the following integral of motion (see also [8, 9]):

$$\gamma - \beta_g p - \Phi = \text{const.} \quad (3)$$

Let us consider an electron which is initially situated ahead of the pulse at a certain point ξ_0 , where $\Phi = 1$ and $a = 0$. If the electron velocity is lower than v_g , it will fall with time within the pulse and WW fields and, thus, can be trapped. At the trapping point (or, what is the same, at the reflection point), the electron velocity becomes equal to v_g , and Eq. (3) gives

$$S \equiv (1 + a_r^2/2)^{1/2} / \gamma_g - (\Phi_r - 1) = (1 + p^2)^{1/2} - \beta_g p. \quad (4)$$

In Eq. (4), a_r and Φ_r are the pulse amplitude and the potential at the reflection point ξ_r , respectively, and p is the momentum of the test electron ahead of the pulse at the point ξ_0 . From Eq. (4) one has

$$p_{1,2} = \gamma_g [\beta_g \gamma_g S \pm (\gamma_g^2 S^2 - 1)^{1/2}]. \quad (5)$$

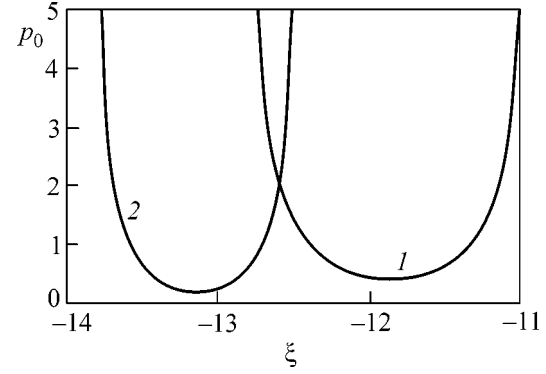


Fig. 2. Initial electron momentum p_0 as a function of the trapping point near the first accelerating maximum; $a_0 =$ (1) 2 and (2) 3.

The minus sign in Eq. (5) corresponds to the initial momentum p_0 (at the point ξ_0) of the electron trapped at the point ξ_r , and the plus sign corresponds to the final momentum of the electron which was initially situated at the point ξ_r . The equation of motion (2) can be recast as

$$\frac{d^2 \xi}{d\tau^2} + \frac{(1 - \beta_g \beta) da^2}{4\beta_g^2 \gamma^2 d\xi} + \frac{(1 - \beta^2)}{\gamma} E_z = 0, \quad (6)$$

where ξ is the coordinate of the test electron in the coordinate system comoving with the laser pulse. The dimensionless electron velocity is found from the equation $\beta = \beta_g (1 + d\xi/d\tau)$.

3. Equations (1) and (6) were solved numerically for the Gaussian pulse profile:

$$a = a_0 \exp(-\xi^2/\sigma^2). \quad (7)$$

The σ value was taken to be two, and $\gamma_g = 10$. A laser pulse with $a_0 = 2$ and the nonlinear WW excited by it are shown in Fig. 1. Figure 2 presents the initial electron momentum p_0 as a function of the trapping point near the first accelerating WW maximum. The minimal value p_{\min} corresponds to the trapping point, where the potential achieves its minimum and $E_z = 0$. Curves 1 and 2 in Fig. 2 has minima at different points because of a nonlinear increase in the WW length with increasing amplitude (the dependence of the wavelength on the amplitude can be found in [10]). The p_{\min} value and the WW amplitude as functions of a_0 are shown in Fig. 3. One can see that the laser pulse with $a_0 \sim 1$ (which corresponds to the pulse peak intensity $I_{\max} \sim 10^{18}$ W/cm² at the laser wavelength $\lambda_L = 1$ μ m or $I_{\max} \sim 10^{16}$ W/cm² at $\lambda_L = 10$ μ m) provides trapping of the initially nonrelativistic or weakly relativistic electrons by the WW. For instance, $p_{\min} \approx 0.4$ for the WW presented in Fig. 1.

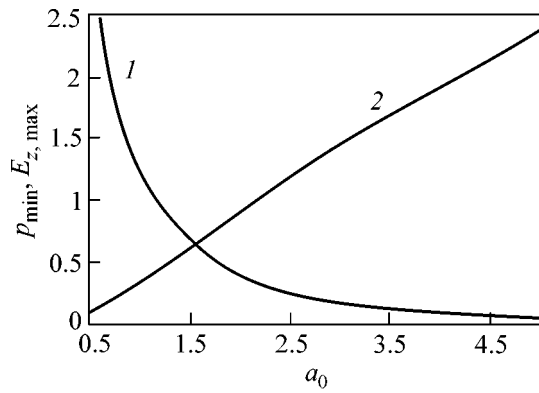


Fig. 3. (1) Minimal momentum p_{\min} of electrons trapped by the wake wave and (2) amplitude $E_{z, \max}$ of its electric field as functions of the peak amplitude a_0 of laser pulse.

Therefore, the particles with $p < p_{\min}$ are not trapped by the wave and can be found behind the WW. This fact may be used for the experimental determination of the WW amplitude from the $p_{\min}(E_{z, \max})$ dependence (Fig. 3). The numerical results show that electrons with $v_0 < v_g$ cannot be trapped in the region of laser pulse because of the decelerating wake field. Only the electrons with initial velocity $v_0 \approx v_g$ can be trapped by the

leading edge of the pulse, where $E_z \approx 0$. Figure 4 illustrates the behavior of electrons of an extended monochromatic electron beam (with $p_0 = 0.5$) in a wake field shown in Fig. 1. The initial bunch length $L_0 = 5$ corresponds, approximately, to the length λ_p of a linear plasma wave. For $\tau = 50$, $L \approx 0.027$ and for $\tau = 100$, $L \approx 0.04$, which is much shorter than both λ_p and λ_L (recall that, in our case, $\gamma_g = 10 \approx \lambda_p/\lambda_L$). Although the energy spread for the accelerated electrons $\Delta\gamma$ slightly grows with τ , the relative energy spread $\varepsilon = \Delta\gamma/\gamma$ drops; at $\tau = 50$, $\varepsilon \approx 0.26$, and at $\tau = 100$, $\varepsilon \approx 0.14$. Thus, one has a substantial (by approximately two orders of magnitude) compression and strong acceleration (with a rate equal to approximately 2 MeV over a length of λ_p) of the initially nonrelativistic ($\gamma_0 \approx 1.12$) electron beam. The energy spread in the trapped bunch depends both on the initial energy spread and on the initial electron beam length; the particles at the trailing part of the bunch are trapped first and, hence, are more energetic at a given τ . At $\tau \ll \tau_a$ (τ_a is the acceleration time, i.e., the time it takes for the trapped electrons to leave the accelerating phase of the wave), for the energy spread of the initially monochromatic beam, one can write: $\Delta\gamma \sim E_z \Delta\tau \approx E_z L_0 (1 - v_0/v_g)^{-1} (\Delta\tau$ is the beam duration) and $\varepsilon \sim L_0 (1 - v_0/v_g)^{-1} (\tau - \tau_{tr})$ (τ_{tr} is the time it takes for the electrons to be trapped by the wave), which is con-

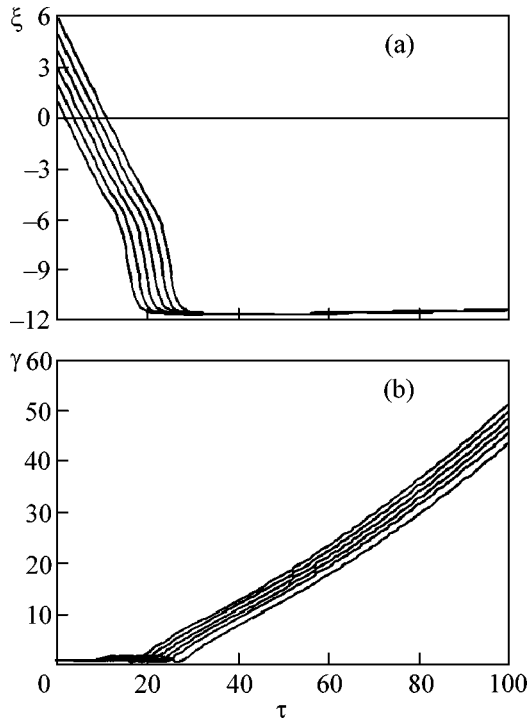


Fig. 4. Trapping and acceleration of the initially monochromatic electron beam by the wake wave shown in Fig. 1. Electron momentum $p_0 = 0.5$ and $\xi_0 = 1, 2, 3, 4, 5,$ and 6 . Time variation of the (a) coordinate and (b) relativistic factor.

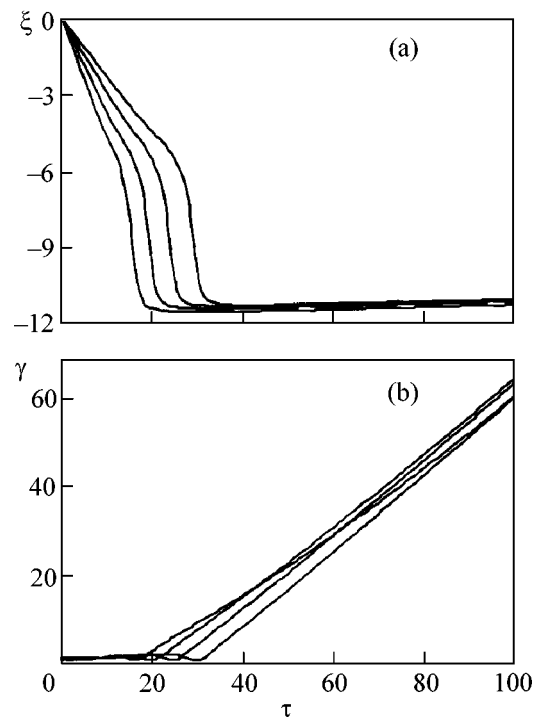


Fig. 5. Behavior of the electrons with $\xi_0 = 0$ and initial momenta $p_0 = 0.6, 0.8, 1,$ and 1.2 in the wake field shown in Fig. 1. Electrons with smaller initial momentum are trapped first; electron (a) coordinate and (b) relativistic factor.

firmed by the numerical results. For the density of a trapped bunch, one has $n_b(\tau) \approx n_{b0}L_0/L(\tau)$, where n_{b0} is the initial density of the electron beam. Figure 5 illustrates the behavior of the electrons of a beam with initial momentum spread $0.6 \leq p_0 \leq 1.2$ in the WW shown in Fig. 1. The length of the captured bunch is shorter than λ_p by approximately a factor of 27, which is by an order of magnitude greater than for the monochromatic beam presented in Fig. 4. For $\tau = 100$, the relative energy spread in the accelerated beam is lower than 0.1, i.e., it is an order of magnitude lower than the spread in the initial electron beam.

The trapped bunch also excites WW. Since the accelerating bunch is short ($L \ll \lambda_p$), one has the following for the corresponding WW amplitude normalized to E_{WB} [11]: $E_{b, \max} = k_p(N_b/n_p)$, where N_b is the number of bunch electrons per unit area. Note that this expression is valid for both linear and nonlinear waves [11]. Since $N_b \sim n_{b0}L_0/k_p$, one has $E_{b, \max} \sim L_0(n_{b0}/n_p)$. For the WW excited by an intense laser pulse, the plasma density equals $\sim 10^{16} - 10^{18} \text{ cm}^{-3}$. Such a density is caused by the length of intense laser pulses, which, in turn, should be equal to approximately $\lambda_p/2$. In our case, to prevent strong energy spread in the accelerated bunch, L_0 should not be too large; it should be shorter than ~ 10 . Then, for $n_{b0} < 10^{14} \text{ cm}^{-3}$, the bunch wake field can be ignored compared to the laser WW.

The resulting short relativistic and dense electron bunch may be used for further acceleration in a multi-stage laser wake-field accelerator [12]. Note also that the suggested scheme of electron trapping and acceleration by the laser WW allows the particles of the initial bunch to be energetically separated, because both slow (with $p_0 < p_{\min}$) and fast (with $p_0 \geq \beta_g \gamma_g$) electrons cannot be trapped.

4. In summary, the results presented in this work demonstrate that an initially nonrelativistic or weakly relativistic electron beam can be efficiently compressed and accelerated due to the interaction with the laser WW. The above scheme removes stringent requirements that are imposed by the other injection methods upon the bunch injected into the wave. In this scheme, the use of an initially nonrelativistic electron beam (with $\gamma_0 \sim 1-1.5$) allows it to be compressed in a much shorter time and more (by an order of magnitude) efficiently than for a short ($L_0 \ll \lambda_p$) relativistic ($\gamma_0 = 100$)

bunch compressed in the WW due to the longitudinal gradient of the accelerating field [13].

I have considered the one-dimensional case. For a laser pulse with the finite transverse size, one should include the transverse force acting on electrons. The numerical results obtained for the nonlinear wake waves excited by the cylindrically symmetric pulses suggest that the radial force maintains focusing all the way from the pulse leading edge to the first accelerating maximum in the wake [7]. The preliminary results obtained for a three-dimensional WW excited in plasma channel have shown that the trapped bunch is efficiently compressed in both longitudinal and transverse directions; these results will be published elsewhere.

I am grateful to B. Hafizi, R. Hubbard, and P. Sprangle (Naval Research Laboratory, Washington, DC) for discussions.

REFERENCES

1. E. Esarey, P. Sprangle, J. Krall, and A. Ting, IEEE Trans. Plasma Sci. **24**, 252 (1996).
2. C. I. Moore, A. Ting, S. J. McNaught, *et al.*, Phys. Rev. Lett. **82**, 1688 (1999).
3. D. Umstadter, J. K. Kim, and E. Dodd, Phys. Rev. Lett. **76**, 2073 (1996).
4. E. Esarey, R. F. Hubbard, W. P. Leemans, *et al.*, Phys. Rev. Lett. **79**, 2682 (1997).
5. E. Esarey, P. Sprangle, J. Krall, and A. Ting, IEEE J. Quantum Electron. **33**, 1879 (1997).
6. N. E. Andreev, L. M. Gorbunov, V. I. Kirsanov, *et al.*, Phys. Plasmas **4**, 1145 (1997).
7. A. G. Khachatryan, Phys. Rev. E **60**, 6210 (1999).
8. C. Du and Z. Xu, Phys. Plasmas **7**, 1582 (2000).
9. A. J. W. Reitsma, V. V. Goloviznin, L. P. J. Kamp, and T. J. Schep, Phys. Rev. E **63**, 046502 (2001).
10. A. G. Khachatryan, Phys. Plasmas **4**, 4136 (1997).
11. R. D. Ruth, A. W. Chao, P. L. Morton, and P. B. Wilson, Part. Accel. **17**, 171 (1985).
12. S. Cheshkov, T. Tajima, W. Horton, and K. Yokoya, Phys. Rev. ST Accel. Beams **3**, 071301 (2000).
13. N. E. Andreev, S. V. Kuznetsov, and I. V. Pogorelsky, Phys. Rev. ST Accel. Beams **3**, 021301 (2000).

Translated by V. Sakun

Influence of Ultrashort Laser Pulse Duration on the X-ray Emission Spectrum of Plasma Produced in Cluster Target

A. I. Magunov¹, T. A. Pikuz², I. Yu. Skobelev², A. Ya. Faenov², F. Blasco³, F. Dorchiev³, T. Caillaud³, C. Bonte³, F. Salin³, C. Stenz³, P. A. Loboda⁴, I. A. Litvinenko⁴, V. V. Popova⁴, G. V. Baïdin⁴, G. C. Junkel-Vives⁵, and J. Abdallah, Jr.⁵

¹*Institute of General Physics, Russian Academy of Sciences, ul. Vavilova 38, Moscow, 119991 Russia*

²*Research Institute of Physicotechnical and Radio Engineering Measurements, State Scientific Center, Mendeleevo, Moscow region, 141570 Russia*

³*CELIA, 33405 Talence, France*

⁴*All-Russia Research Institute of Technical Physics, Russian Federal Nuclear Center, Snezhinsk, Chelyabinskaya region, 456770 Russia*

⁵*Theoretical Division, T-4, Los Alamos National Laboratory, Los Alamos NM 87545, USA*

Received August 29, 2001

Line emission spectrum of a laser plasma produced in an argon cluster jet target was measured on the $n^1P_1-1^1S_0$ ($n = 5-9$) transitions of the helium-like Ar XVII ion for a pulse duration varying from 45 fs to 1.1 ps and a constant fluence of $\sim 10^5$ J/cm². The independent modeling of the relative intensities of the transitions from the $n = 5, \dots, 10$ levels, as well as of the $2^1P_1-1^2S_0$ and $2^3P_1-1^2S_0$ lines and dielectronic satellites indicates that the electron temperature is anomalously low and that the electron density in emitting plasma increases with shortening the laser pulse. The excitation from the ground state by a small fraction of hot electrons is expected to be the main channel of populating the Ar XVII levels. © 2001 MAIK "Nauka/Interperiodica".

PACS numbers: 52.25.Os; 52.50.Jm; 32.30.Rj; 41.50.+h

1. At present, much importance is attached to studying the interaction of high-intensity ultrashort laser pulses with clusters [1–9]. A cluster target combines the main laser mechanisms of plasma formation in gas and solid targets (optical ionization and resonance absorption). It has been found experimentally that the interaction of ultrashort laser pulses with cluster targets is characterized by highly efficient absorption. This property is particularly important in the fabrication of high-intensity X-ray sources for microlithography and medical and biomolecular studies. Unfortunately, the experimental results obtained to date are not systematic because they depend on a wide range of parameters that characterize the laser pulse and the targets. This strongly hampers the analysis of diversified physical processes occurring in plasma and the possibility of detailed verification of the theoretical models [10, 11] describing the specific features of plasma formation by ultrashort pulses, e.g., the important role of a prepulse was examined in [7, 9].

In the experimental studies of the femtosecond laser cluster-target plasma, X-ray spectroscopy is one of a few methods that can be used to gain information about the plasma parameters and the processes occurring in it. Recently [12], the intensity of X-ray emission from Ar and Kr cluster plasma was studied as a function of the laser pulse duration at a fixed energy. The results of

these measurements revealed two laser absorption regimes for different pulse durations and target sizes: bulk and surface absorption.

This work reports the results of measuring the X-ray emission spectra of plasma produced by laser pulses with a duration from 45 fs to 1.1 ps, a fluence of 10^5 J/cm² in the focal plane, and a high contrast of $\sim 10^5$ in an Ar gas-jet target with a high cluster content. The use of a high-resolution curved-crystal spectrograph [13] made it possible to detect the resonant series of the He-like argon ion, including the transitions from its n^1P_1 ($n \geq 5$) levels and to obtain the detailed structure for the dielectronic satellites of the $2^1P_1-1^1S_0$ line. The experimental results on the widths and relative intensities of these lines as functions of pulse duration were modeled with allowance for the main line-broadening mechanisms and the steady-state impact-radiation kinetics. The computations show that, as the pulse duration shortens, the main contribution to the time-integrated intensity of the plasma line emission comes from the more and more dense (supercritical) plasma region. The temperature of the main fraction of electrons changes only weakly and is anomalously low, as compared to the usual temperature observed for nanosecond plasma.

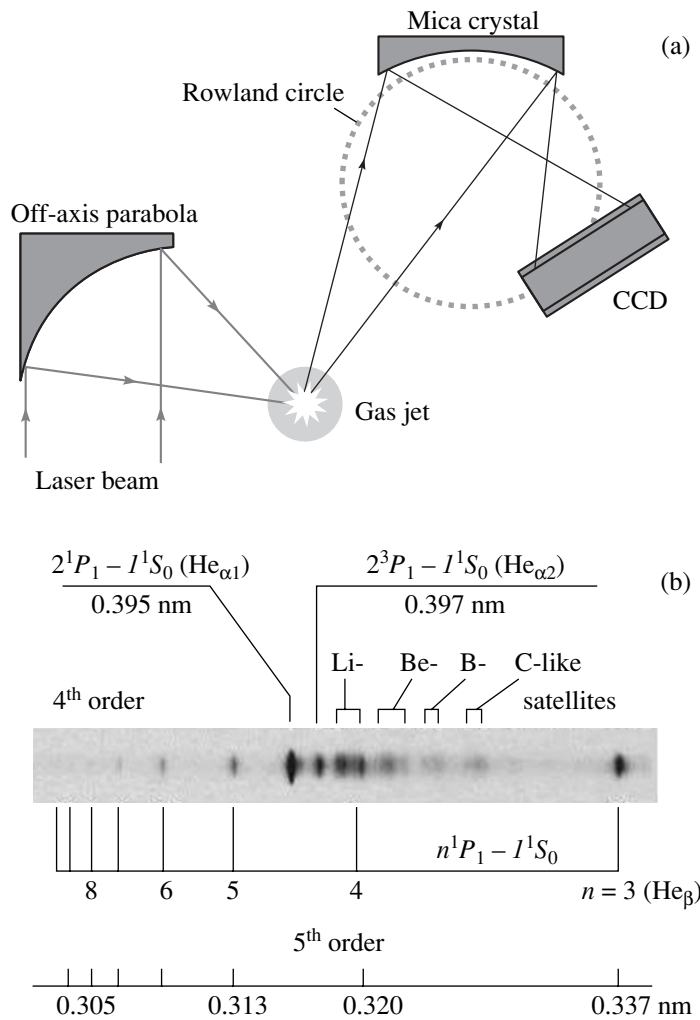


Fig. 1. (a) Scheme for measuring the X-ray emission spectra of laser plasma in the argon jet target. (b) Argon plasma spectrogram for a laser pulse duration of 1.1 ps.

2. Experiments were performed on the laser system of the University of Bordeaux with the four-stage amplification of a chirped pulse by Ti-sapphire rods. The characteristics of the laser system are described in more detail in [14]. In our experiments (Fig. 1a), the pulse energy at the output was 15 mJ with a contrast of $\sim 10^5$ relative to the energy of the prepulses produced by a regenerative amplifier that is incorporated into the system. The laser beam was focused by an off-axis parabolic mirror. The focal spot radius in vacuum was $6 \mu\text{m}$ at the $1/e^2$ level, which corresponded to a maximal fluence of 10^5 J/cm^2 in the spot. The variation of the pulse duration from 45 fs to 1.1 ps corresponded to a change in the maximum intensity from 3×10^{15} to 10^{17} W/cm^2 , which was sufficient for the tunnel ionization of the F-like and P-like argon ion, respectively [15].

A pulsed gas jet of Ar atoms expanded into a vacuum chamber from a cylindrical supersonic nozzle with a diameter of 2.5 mm and Mach number $M = 2.5$ served

as the target. The maximal gas pressure in the valve was 60 atm, and the jet divergence angle was 22° . Under these conditions, van der Waals forces led to the formation of atomic clusters in the jet [8, 16], with the maximum electron density much greater than its critical value $N_{e,cr} \approx 1.7 \times 10^{21} \text{ cm}^{-3}$ (for $\lambda_{\text{las}} = 0.8 \mu\text{m}$). The cluster formation was confirmed indirectly by the lack of X-ray emission at a low contrast, i.e., when the clusters were destroyed by the prepulse.

The X-ray spectra were measured using focusing spherical ($R = 150 \text{ mm}$) crystal (mica) spectrographs [17] (Fig. 1a) in the frequency range 0.305–0.425 nm (fourth- and fifth-order reflections) with the resolution $\lambda/\Delta\lambda \approx 3000\text{--}5000$. The spectrographs were set at a right angle to the laser beam axis and provided the spatial resolution either along this axis or perpendicular to it. The spectra were recorded by a CCD chamber, ahead of which a 2- μm -thick polypropylene layer filter coated on both sides with 0.4- μm aluminum layers was placed.

The plasma spectrogram for the pulse with a duration of 1.1 ps is shown in Fig. 1b.

3. The observed intensities of the Ar XVII $2^{1,3}P_1-1^1S_0$ lines and the dielectronic Li- and Be-like satellites are shown in Fig. 2 for pulse durations of 1.1 ps, 700 fs, and 45 fs. The results of calculations by the formula

$$I(\lambda) = C_1 I(\lambda, N_{e1}, T_{e1}) + C_2 I(\lambda, N_{e2}, T_{e2}) \quad (1)$$

are presented in the same figure for two sets of plasma parameters. It was assumed that these lines had a Doppler contour (including the instrumental width). The temperatures and the electron densities giving the best agreement with the observed relative line intensities are presented in the table. The level populations and the charge composition were calculated using the steady-state impact-radiation kinetic model. The inelastic transition rates for the electron-ion collisions were calculated using the distribution function $F(E) = F_M(E, T_e) + f\delta(E - E_{\text{hot}})$, where the contribution from hot electrons with energies $E_{\text{hot}} = 5$ keV was included as a small addition to the Maxwellian distribution F_M . The values of the weight multiplier f are given in the table. Previous calculations with this model [18] have shown that even a small amount of hot electrons with these parameters makes a sizable contribution not only to the satellites but also to the resonance lines of the He-like ions with atomic numbers $Z_n = 10-20$. Since E_{hot} is on the order of ionization potential of these ions, these electrons are expected to efficiently excite the Rydberg states n^1P_1 with $n \geq 4$ as well.

Figure 3 shows the measured plasma emission spectra for various pulse durations in the range of the $n^1P_1-1^1S_0$ ($n \geq 5$) transitions of the He-like argon ion. The observed spectra were approximated by the sum of two terms in Eq. (1) with the same N_e and T_e values and the same fraction of hot electrons as is given in the table. The method of calculating $I(\lambda, N_e, T_e)$ for a He-like ion with high n was described in more detail in [14]. The line contours of Ar XVII were determined with inclusion of the Stark shift in an ionic microfield, the impact broadening due to elastic electron-ion collisions, and the Doppler broadening [19]. The latter was taken into account in combination with the spectral resolution, which corresponded to the effective ion temperature $T_i = 2$ keV. The distribution function for the ionic microfield was taken with regard to the ion correlations and the Debye screening [20, 21]. The coefficients C_1 and C_2 were derived from the widths and relative intensities of the observed lines. The fraction of hot electrons substantially affects the relative populations of Rydberg levels.

One can see from Figs. 2 and 3 that the results of independent calculations with the chosen plasma parameters reproduce well the experimental data. The calculations of the resonance line contours for $n \geq 5$ indicate that the shortening of the pulse duration brings about an increase in the plasma electron density which

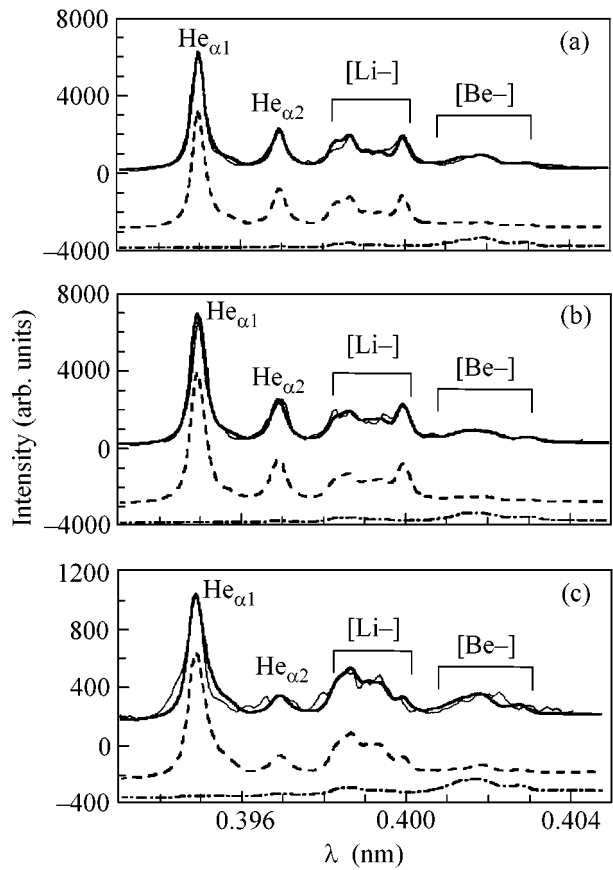


Fig. 2. Comparison of the measured spectra of Ar plasma with the results of model calculations (plasma parameters are given in the table) for the $\text{He}_{\alpha 1}$ and $\text{He}_{\alpha 2}$ ($2^{1,3}P_1-1^1S_0$) lines of the He-like Ar XVII ion and for the dielectronic Li- and Be-like satellites at different pulse durations: (a) 1.1 ps, (b) 700 fs, and (c) 45 fs. The tin solid line is for the experiment, the thick solid line is for the calculation, the dashed line is for the high-density contribution, and the dash-dotted line is for the low-density contribution.

makes the main contribution to the observed spectrum. Moreover, the relative contribution of the subcritical electron density (gas phase) decreases with pulse shortening. It follows from the well-known Inglis-Teller limit (see, e.g., [19]) that the transition lines with high n disappear with increasing plasma density. In our case,

Table

τ_{las} (fs)	N_e (cm^{-3})	T_e (eV)	f
1100	3×10^{19}	130	10^{-8}
	3×10^{21}	200	3×10^{-4}
700	3×10^{19}	130	3×10^{-7}
	4×10^{21}	215	3×10^{-4}
45	3×10^{19}	130	10^{-7}
	10^{22}	200	7×10^{-5}

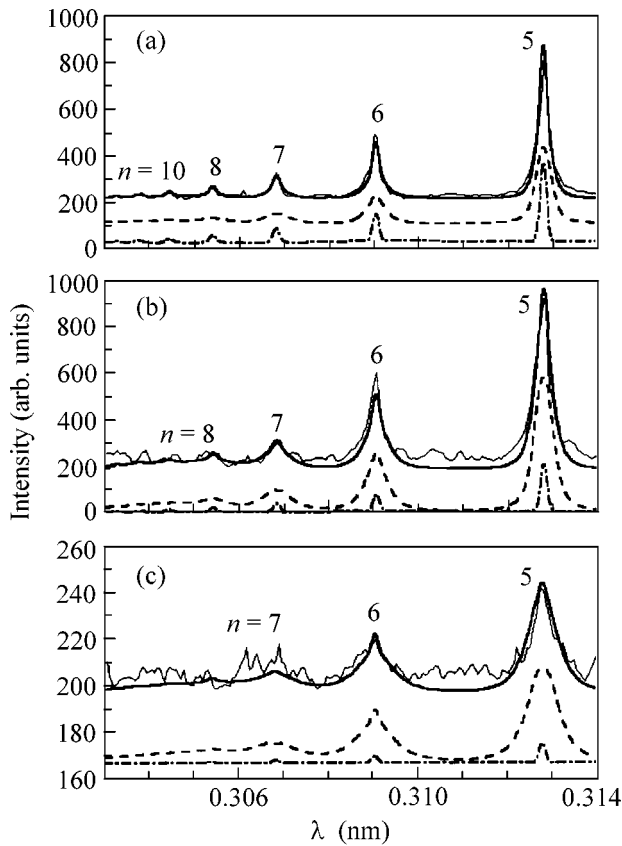


Fig. 3. The same as in Fig. 2, but for the $n^1P_{1-1}^1S_0$ ($n \geq 5$) lines.

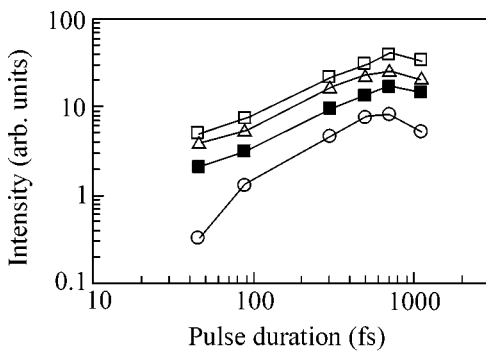


Fig. 4. Emission intensities of the He-like Ar XVII lines vs. pulse duration at a fixed energy. The symbols correspond to the following lines: (□) He_{α_1} , (■) He_{α_2} , (△) He_{β} , and (○) $5^1P_{1-1}^1S_0$.

this may be due to the fact that the clusters do not fully decompose during the decay of plasma emission on the He-like transitions. For pulse durations of ~ 1 ps, the laser absorption proceeds in parallel with the cluster

decomposition, which is seen from a decrease in the dominant electron density of emitting plasma. For all durations, the electron temperature is too low to ionize and efficiently excite the He-like argon ion, so the observed line emission may be due only to the population of Rydberg levels through the excitation by a small fraction of hot electrons that are generated in the spatially inhomogeneous intense laser field. Because the common electron temperature is established rather slowly (especially for gas densities), the influence of hot electrons on the plasma relaxation kinetics can manifest itself for a longer time than the laser pulse duration.

The ratio of emission intensities for different pulse durations is in agreement with the results obtained in [12]. The observed intensities of different lines are shown in Fig. 4 as functions of the pulse duration. In particular, in the range studied, from 45 fs to 1 ps the absolute X-ray yield shows a nonmonotonic behavior with a maximum near 700 fs. This may be due to a decrease in the efficiency of laser absorption at the shorter and longer durations.

4. In summary, it has been shown that the model suggested in our previous works [7, 9] for cluster heating by ultrashort laser pulses adequately describes not only the intensities of resonance lines and their satellites but also the contours of the He-like Ar XVII Rydberg lines ($n = 5, \dots, 10$), the latter being recorded with a high resolution for the first time. The results of measurements and calculations suggest that the shortening of the laser pulse leads to an increase in the plasma electron density. The main contribution to the X-ray yield comes from the plasma with supercritical electron density. The observed emission lines are due to the excitation of the upper levels of the Ar ion by a small fraction of hot electrons that are generated in the laser field. For the pulse durations shorter than 700 fs, the intensity of plasma X-ray emission decreases. This may be crucial for the design of X-ray sources based on the femtosecond laser plasma.

This work was supported in part by the Ministry of Energetics of the USA, the Fond European de Developement Economique Regional and Conseil Regional d'Aquitaine (France), and the NATO (grant no. PST.CLG.977637). A.Ya.F. and T.A.P. are grateful to CRDF for the grant that made it possible to present this work at International Conferences.

REFERENCES

1. A. McPherson, T. S. Luk, B. D. Thompson, *et al.*, *Appl. Phys. A* **A57**, 337 (1993).
2. A. McPherson, T. S. Luk, B. D. Thompson, *et al.*, *Phys. Rev. Lett.* **72**, 1810 (1994).
3. T. Ditmire, T. Donnelly, A. M. Rubenchik, *et al.*, *Phys. Rev. A* **53**, 3379 (1996).
4. M. Lezius, S. Dobosz, D. Normand, and M. Schmidt, *Phys. Rev. Lett.* **80**, 261 (1998).

5. T. Ditmire, J. Zweiback, V. P. Yanovsky, *et al.*, *Nature* **398**, 489 (1999).
6. S. Dobosz, M. Schmidt, M. Perdrix, *et al.*, *Zh. Éksp. Teor. Fiz.* **115**, 2051 (1999) [*JETP* **88**, 1122 (1999)].
7. T. Auguste, P. D'Oliveira, S. Hulin, *et al.*, *Pis'ma Zh. Éksp. Teor. Fiz.* **72**, 54 (2000) [*JETP Lett.* **72**, 38 (2000)].
8. G. C. Junkel-Vives, J. Abdallah, Jr., F. Blasco, *et al.*, *Phys. Rev. A* **64**, 021201 (2001).
9. J. Abdallah, Jr., A. Ya. Faenov, I. Yu. Skobelev, *et al.*, *Phys. Rev. A* **63**, 032706 (2001).
10. I. Last and J. Jortner, *Phys. Rev. A* **62**, 013201 (2000).
11. V. P. Krainov and A. S. Roshchupkin, *J. Phys. B* **34**, L297 (2001).
12. E. Parra, I. Alexeev, J. Fan, *et al.*, *Phys. Rev. E* **62**, R5931 (2000).
13. I. Yu. Skobelev, A. Ya. Faenov, B. A. Bryunetkin, *et al.*, *Zh. Éksp. Teor. Fiz.* **108**, 1263 (1995) [*JETP* **81**, 692 (1995)].
14. C. Stenz, V. Bagnoud, F. Blasco, *et al.*, *Quantum Electron.* **30**, 721 (2000).
15. M. V. Ammosov, N. B. Delone, and V. P. Kraĭnov, *Zh. Éksp. Teor. Fiz.* **91**, 2008 (1986) [*Sov. Phys. JETP* **64**, 1191 (1986)].
16. A. S. Boldarev, V. A. Gasilov, F. Blasco, *et al.*, *Pis'ma Zh. Éksp. Teor. Fiz.* **73**, 583 (2001) [*JETP Lett.* **73**, 514 (2001)].
17. F. Blasco, C. Stenz, F. Salin, *et al.*, *Rev. Sci. Instrum.* **72**, 1956 (2001).
18. G. C. Junkel-Vives, J. Abdallah, Jr., F. Blasco, *et al.*, *J. Quant. Spectrosc. Radiat. Transf.* **71**, 417 (2001).
19. H. R. Griem, *Spectral Line Broadening by Plasmas* (Academic, New York, 1974; Mir, Moscow, 1978).
20. R. J. Tighe and C. F. Hooper, Jr., *Phys. Rev. A* **14**, 1514 (1976).
21. P. A. Loboda, V. V. Popova, and M. K. Shinkarev, *J. Quant. Spectrosc. Radiat. Transf.* **58**, 757 (1997).

Translated by V. Sakun

Theory of Faraday Rotation Beats in Quantum Wells with Large Spin Splitting

V. N. Gridnev

Ioffe Physicotechnical Institute, Russian Academy of Sciences, Politekhnikeskaya ul. 26, St. Petersburg, 194021 Russia
e-mail: gridnev@pop.ioffe.rssi.ru

Received July 11, 2001; in final form, August 22, 2001

Spin dynamics of conduction electrons in a quantum well with a zinc blende structure is considered theoretically for the case where spin splitting exceeds the collisional broadening of energy levels. It is shown that, under certain conditions, the spin density component normal to the quantum well plane may oscillate with time even in the absence of an external magnetic field. These oscillations can be excited and detected using nonlinear two-pulse spectroscopy. Contrary to the case of small spin splitting, the external transverse magnetic field strongly affects spin dynamics in this regime. © 2001 MAIK “Nauka/Interperiodica”.

PACS numbers: 76.20.+q; 78.20.Ls; 73.21.Fg; 78.47.+p

In recent years, considerable interest has been shown in the properties of coherent spin states in semiconductors and hybrid ferromagnet–semiconductor systems [1–3]. These states have finite lifetimes, because thermal fluctuations break coherence with a rate strongly depending on the properties of a particular system. The revelation of the factors influencing the rate of spin coherence breakdown is one of the topical problems of the new direction in solid-state physics—spintronics.

Nonlinear optical two-pulse spectroscopy is an efficient method for investigating spin dynamics. In this method, the first light pulse is circularly polarized and creates an electron-excited spin density (spin orientation) \mathbf{S}_0 , whose degree is characterized by the optical rotation θ of the second linearly polarized light pulse.

The use of the methods of nonlinear pulsed spectroscopy allowed for the measurements of not only the averaged quantities but also their time evolution. For example, the dependence of the angle of rotation of polarization plane θ on the delay time t_d between the pulses characterizes the time evolution of spin orientation $\mathbf{S}(t)$. The character of this evolution depends on the magnitude and direction of an external magnetic field \mathbf{B} . Spin coherence manifests itself as oscillations of the Faraday rotation as a function of delay time t_d in a transverse (to the light direction) magnetic field. These oscillations are associated with the quantum beats between the electronic Zeeman sublevels, and their damping characterizes the spin coherence breakdown with time [4].

In this work, new potentials for studying the spin dynamics in semiconducting heterostructures are suggested on the basis of an analysis of the time dependence $\mathbf{S}(t)$. In particular, the oscillations of $S_z(t)$ in a quantum well (the z axis is aligned with the normal to

the quantum well) will be analyzed, and it will be shown that spin splitting in a conduction band can give rise to such oscillations even in the absence of an external magnetic field.

It should be noted at this point that spin relaxation processes in semiconductors were extensively studied previously in the context of a widely used optical orientation method [5]. The understanding attained in these works as to the mechanisms of these processes serves as a basis for the current study. However, previous theoretical calculations of the optical effect caused by spin relaxation started from the assumption that the light sources used for optical pumping were continuous. The corresponding measured quantities, e.g., the degree of luminescence polarization, were averaged over the electron lifetime in the conduction band. With this averaging, one inevitably loses part of the information about the spin relaxation mechanisms. Because of this, the elaboration of new experimental methods and, in particular, the method of nonlinear pulsed spectroscopy necessitates, in some cases, additional theoretical analysis of the spin dynamics of photoexcited electrons.

Let us consider the time evolution of spin density for optically oriented electrons in the conduction band of a quantum well with the zinc blende structure in an external magnetic field \mathbf{B} parallel to the plane of the quantum well. If one neglects all relaxation processes except the spin relaxation, the time-dependent average electron spin \mathbf{S} is usually calculated from the equation [5]

$$\frac{d\mathbf{S}}{dt} = \Omega_L \times \mathbf{S} - \frac{\mathbf{S}}{\tau_s(\mathbf{B})}, \quad (1)$$

where $\Omega_L = g\mu_B\mathbf{B}/\hbar$ and $\tau_s(\mathbf{B})$ is the spin relaxation time, which depends, apart from the purely microscopic factors, on the magnitude of \mathbf{B} and its orientation

about $S(0)$. In the Voigt geometry $\mathbf{B} \parallel x$ and $\mathbf{S}(0) \parallel z$, Eq. (1) gives

$$S_z(t) = S_z(0) \cos(\Omega_L t) \exp(-t/\tau_s). \quad (2)$$

In this case, τ_s is the spin coherence decay time. Since the Faraday rotation $\theta(t_d) \sim S_z(t_d)$, one can determine τ_s by measuring the damping of the $\theta(t_d)$ oscillations (for more detail, see [4]). This method was used in the study of spin coherence in bulk semiconductors [6], quantum wells [1, 7], and quantum dots [8].

However, relation (2) and underlying Eq. (1) apply only under certain conditions that depend on the mechanism of electron spin relaxation. The experimental determination of the dominant spin relaxation mechanism is a challenge for each particular sample, because the variation of the sample parameters, such as dopant concentration and temperature, changes appreciably the relative role of different mechanisms [5, 9]. In the samples with high mobility and at high temperatures, the D'yakonov-Perel' (DP) relaxation mechanism based on the spin-orbit (spin) splitting of the conduction band prevails [10]. This splitting is described by the following term in the electron Hamiltonian:

$$V_s = \frac{\hbar}{2} \Omega_s(\mathbf{k}) \boldsymbol{\sigma}, \quad (3)$$

where \mathbf{k} is the electron wave vector, $\boldsymbol{\sigma} = \{\sigma_x, \sigma_y, \sigma_z\}$ are the Pauli matrices, and $\Omega_s(\mathbf{k})$ can be regarded as a \mathbf{k} -dependent effective magnetic field. In quantum wells, the two-dimensional vector $\Omega_s(\mathbf{k})$ depends linearly on k_x and k_y at small \mathbf{k} , and, in the general case, it contains two contributions, one of which (bulk) is caused by the absence of an inversion center in the zinc blende structure [11] and the other (surface) occurs only in the asymmetrical quantum wells [12]. The relative magnitude of these contributions may be different; however, an important point is that, at a given electron energy, the electron spin splitting in a sufficiently narrow quantum well is larger than in the bulk material [13], and, as a consequence, the role of the DP spin-relaxation mechanism in quantum wells increases. This mechanism becomes more efficient with increasing parameter $\Omega_s \tau$, where τ is the momentum relaxation time. At $\Omega_s \tau \geq 1$, the spin relaxation time $\tau_s \sim \tau$. The experimental measurements of the spin splitting in quantum wells [14, 15] give $\hbar \Omega_s \approx 1$ meV for $k \approx 10^{-6}$ cm $^{-1}$. At $\tau \approx 1$ ps, $\Omega_s \tau \sim 1$, and the spin-orbit interaction (3) cannot be regarded as a small perturbation.

Under these conditions, simple Eq. (1) for the damped electron spin precession in a magnetic field is no longer valid, because the interaction (3) induces spin precession by itself, i.e., even in the absence of a magnetic field. A consistent analysis of this issue requires the nonperturbative approach to the spin splitting [10, 13].

To calculate the average spin $S(t)$, it is necessary to find the electron spin density matrix $\rho_{ss'}(\mathbf{k})$, where

$s, s' = \pm 1/2$, and \mathbf{k} is the two-dimensional wave vector in the plane of quantum well. The spin $S(t)$ is related to $\rho_{ss'}(\mathbf{k})$ by the formula

$$\mathbf{S}(t) = \text{Tr} \boldsymbol{\sigma} \int \frac{d\mathbf{k}}{(2\pi)^2} \hat{\rho}(\mathbf{k}, t). \quad (4)$$

The density matrix $\hat{\rho}(\mathbf{k}, t)$ can be conveniently written as

$$\rho_{ss'}(\mathbf{k}, t) = \frac{1}{2} [n(\mathbf{k}, t) \delta_{ss'} + \boldsymbol{\sigma}_{ss'} \cdot \mathbf{S}(\mathbf{k}, t)]. \quad (5)$$

The vector $\mathbf{S}(\mathbf{k}, t)$ determines the spin density and satisfies the following equation [10, 16]:

$$\begin{aligned} \frac{d\mathbf{S}(\mathbf{k})}{dt} &= \Omega(\mathbf{k}) \times \mathbf{S}(\mathbf{k}) \\ &+ \int \frac{d\mathbf{k}'}{(2\pi)^2} W(\mathbf{k}, \mathbf{k}') (\mathbf{S}(\mathbf{k}') - \mathbf{S}(\mathbf{k})), \end{aligned} \quad (6)$$

where $W(\mathbf{k}, \mathbf{k}')$ is the scattering probability and $\Omega(\mathbf{k}) = \Omega_L + \Omega_s(\mathbf{k})$. Assume that the scattering is elastic, i.e., that $W(\mathbf{k}, \mathbf{k}')$ depends only on the angle between \mathbf{k} and \mathbf{k}' . On the right-hand side of Eq. (6), the term accounting for the electron generation is omitted, because, for a sufficiently short pump pulse with $\tau_p \approx 100$ fs, the electron generation can be taken into account by writing the initial condition as $S_z^0(0) = S_0$. To simplify the calculation, we assume that the effective magnetic field $\Omega_s(\mathbf{k})$ in Eq. (3) is the sum of contributions from either of two mechanisms: surface with $\Omega_s(\mathbf{k}) \sim \{k_y, -k_x\}$ or bulk with $\Omega_s(\mathbf{k}) \sim \{k_x, -k_y\}$ (the orientation of the quantum well is assumed to be [001]). In either of these cases, $\Omega_s(\mathbf{k}) = |\Omega_s(\mathbf{k})|$ is independent of the \mathbf{k} and $\Omega_s(\mathbf{k})$ directions and can be represented in the form

$$\Omega_s(\mathbf{k}) = \mathbf{a} e^{i\phi} + \mathbf{a}^* e^{-i\phi}, \quad (7)$$

where the angle ϕ specifies the direction of vector \mathbf{k} in the plane of a quantum well, and the two-dimensional complex vector \mathbf{a} satisfies the condition $\mathbf{a}^2 = 0$ and depends linearly on \mathbf{k} .

Following [16], let us expand $\mathbf{S}(\mathbf{k})$ and $W(\mathbf{k}, \mathbf{k}')$ in the Fourier series,

$$\mathbf{S}(\mathbf{k}) = \sum_n \mathbf{S}^n e^{in\phi},$$

$$W(\phi - \phi') = \sum_n W_n e^{in(\phi - \phi')}.$$

After substitution of these expansions into Eq. (6), one obtains the infinite set of linear differential equations for the coefficients $\mathbf{S}^n(t)$. This set of equations should be used to find the z component of the total spin $S_z^0(t)$ that is responsible for the Faraday rotation. The method of solving this set depends on the value of parameter

$\kappa = \Omega_s \tau$, where τ is the momentum relaxation time. If $\kappa \ll 1$, then $S_z^{n+1} \sim \kappa S_z^n$ and, as long as we are interested in the relaxation of S_z^0 , all terms \mathbf{S}^n with $|n| \geq 2$ can be ignored in the resulting set of equations. In this case, \mathbf{S}^0 and $\mathbf{S}^{\pm 1}$ satisfy the following set of equations:

$$d\mathbf{S}^0/dt = \mathbf{a} \times \mathbf{S}^{-1} + \mathbf{a}^* \times \mathbf{S}^{+1} + \Omega_L \times \mathbf{S}^0, \quad (8)$$

$$d\mathbf{S}^{+1}/dt = \mathbf{a} \times \mathbf{S}^0 + \Omega_L \times \mathbf{S}^{+1} - \mathbf{S}^{+1}/\tau, \quad (9)$$

$$d\mathbf{S}^{-1}/dt = \mathbf{a}^* \times \mathbf{S}^0 + \Omega_L \times \mathbf{S}^{-1} - \mathbf{S}^{-1}/\tau, \quad (10)$$

where

$$\tau^{-1} = \int \frac{d\phi}{2\pi} W(\phi) [1 - \cos(\phi)]$$

is the momentum relaxation rate.

The spin dynamics is determined by the eigenfrequencies of the set of Eqs. (8)–(10). A remarkable feature of this set is that at $\Omega_L = 0$, i.e., in the absence of an external magnetic field, it provides an exact and closed equation for S_z^0 , which is valid for any value of parameter κ . The corresponding eigenfrequency is given by the expression

$$\omega_{\perp} = \frac{i}{2\tau} (1 - \sqrt{1 - 4\kappa^2}). \quad (11)$$

At $\kappa \ll 1$, the eigenvalue $-i\omega_{\perp} = 1/\tau_{\perp} = \kappa\Omega_s$ is equal to the relaxation rate of the spin z component in a quantum well dominated by the DP mechanism [13]. In the opposite limit $\kappa \gg 1$, one obtains from Eq. (11)

$$\omega_{\perp} = i/2 + \Omega_s. \quad (12)$$

Therefore, at large spin splitting and high mobility, the spin z component oscillates with frequency Ω_s even in the absence of an external magnetic field, with the damping time of these oscillations being $\tau_s = 2\tau$. Note that the eigenfrequency corresponding to the spin x and y components is obtained from Eq. (11) by replacing $\Omega_s \rightarrow \Omega_s/\sqrt{2}$. The resulting relaxation rate for these spin components is half as large at $\kappa \ll 1$ [13], and the precessional frequency is lower by a factor of $\sqrt{2}$ at $\kappa \gg 1$.

Let us now consider the influence of a transverse magnetic field on the eigenfrequency (11). At $\mathbf{B} \neq 0$, the spin components, normal and parallel to the plane of the quantum well, are coupled to each other, so that one fails to obtain an analytical solution to the kinetic Eq. (6). The eigenfrequencies of the set of Eqs. (8)–(10) were calculated numerically for $\kappa \ll 1$. Of interest were those eigenfrequencies which corresponded at zero magnetic field to the relaxation rates $1/\tau_{\perp} = \kappa\Omega_s$ and $1/\tau_{\parallel} = \kappa\Omega_s/2$ for the perpendicular and parallel spin-density components, respectively. The numerical analysis showed that, as the magnetic field increases,

the relaxation modes transform to the oscillation ones with frequency Ω_L , while the relaxation times corresponding to these modes approach a constant value τ_{\parallel} at $\Omega_L \gg 1/\tau$. The fact that τ_s shows little dependence on B can be explained by the mutual compensation of two factors acting in opposite directions. As B increases, the precession axis $\Omega_s + \Omega_L$ becomes more and more closer to Ω_L , leading to a decrease in the DP spin relaxation rate [17]. On the other hand, the growing velocity of spin precession in the magnetic field brings about an increase in the spin relaxation rate. Since only the first of these factors is operative in the longitudinal magnetic field, the spin relaxation time in the longitudinal field increases with increasing B [17].

Let us now consider the influence of a transverse magnetic field on the electron spin dynamics in the limit $\kappa \gg 1$. On the qualitative level, this influence can be understood if one ignores the collision integral in kinetic Eq. (6). In this case, the velocity and sense of spin precession for an electron with momentum \mathbf{k} are given by the vector $\Omega(\mathbf{k}) = \Omega_s(\mathbf{k}) + \Omega_L$. Hence, the precessional frequency in our model becomes dependent at $\mathbf{B} \neq 0$ on the direction of \mathbf{k} . To simplify calculations, let us ignore the fact that the initial photoelectron energy distribution has a finite width due to the finite pump pulse duration. Then, one has for the resulting spin z component

$$S_z(t) = S_z(0) \int \frac{d\phi}{2\pi} e^{-i\Omega(\mathbf{k})t}. \quad (13)$$

If $\Omega_s(\mathbf{k}) \sim \Omega_L$, then the terms with different \mathbf{k} 's in Eq. (13) interfere with each other, resulting in a fast decay of $S_z(t)$ even at $t \sim \Omega_s^{-1} \ll \tau$. In actuality, this decrease in $S_z(t)$ is not a damping, i.e., not an irreversible process, but it is merely the initial stage of a certain quasiperiodic process with a broad distribution of precessional frequencies. However, due to the presence of a weak but, nevertheless, real damping, the initial decay of $S_z(t)$ will not differ in appearance from the irreversible damping. Such a behavior becomes most pronounced if the spin and Zeeman splittings are identical. In this case, one obtains from Eq. (13)

$$S_z(t) = S_z(0) J_0(2\Omega_L t), \quad (14)$$

where $J_0(z)$ is the zero-order Bessel function, whose first zero is situated at $z \approx 2.4$.

It is worth noting that the assumption about the dominance of any one spin-splitting mechanism (surface or bulk) automatically implies that the spin splitting is independent of the \mathbf{k} direction (in the linear approximation in \mathbf{k}). The breaking of this condition does not change qualitatively the conclusions drawn for $\kappa \ll 1$, but it is crucial for $\kappa \gg 1$. In this case, the interference of oscillations of the electrons with different \mathbf{k} 's in Eq. (13) becomes destructive even in the absence of the magnetic field, so that $S_z(t)$ may decrease to zero in a time that is appreciably shorter than τ . As the mag-

netic field increases to a level at which $\Omega_L \gg \Omega_s$, the regime is restored with the relaxation time $\tau_s \sim \tau$. Note that, due to a small value of $\Omega_s(\mathbf{k})$ in a bulk material, the spin dynamics in it will have a relaxational character, so that the strong anisotropy of $\Omega_s(\mathbf{k})$ will not lead to the above-mentioned features in the time dependence $S(t)$.

We note in conclusion that, in spite of the model character of the results obtained in this work, they indicate new potentials of nonlinear two-pulse spectroscopy for studying spin dynamics in semiconducting heterostructures. This method can be used in the search for and study of heterostructures with large spin splitting, where the electron spin dynamics displays a number of indicative features. When performing experimental studies of the effects considered in this work, one should take into account that, if the photoelectron thermalization is too fast and proceeds in a time comparable to the oscillation period, then the oscillations of the total electron spin become hard to observe. This problem is typical for all experimental studies of spin coherence. To minimize the destructive effect of thermalization, it is necessary that the photoelectron energy is not too high. In particular, it must be lower than the energy of optical phonons. If this condition is met, then the oscillations with a period of ~ 1 ns can be observed [6]. However, a decrease in the photoelectron energy in the undoped samples leads to a substantial decrease in the photoelectron momentum and, as a result, to a decrease in the spin splitting. It is thus reasonable to use doped samples for the experimental observation of the oscillations in the Faraday rotation caused by the spin splitting of the conduction band.

This work was supported by the Russian Foundation for Basic Research and the programs "Fundamental Spectroscopy" and "Laser Optics."

REFERENCES

1. D. D. Awschalom and J. M. Kikkawa, *Phys. Today* **52**, 33 (1999).
2. A. Imamoglu, D. D. Awschalom, G. Burkard, *et al.*, *Phys. Rev. Lett.* **83**, 4204 (2001).
3. P. Šeba, P. Exner, K. N. Pichugin, *et al.*, *Phys. Rev. Lett.* **86**, 1598 (2001).
4. L. J. Sham, *J. Magn. Magn. Mater.* **200**, 219 (1999).
5. *Optical Orientation*, Ed. by F. Meier and B. P. Zakharchenya (North-Holland, Amsterdam, 1984; Nauka, Leningrad, 1989).
6. J. M. Kikkawa and D. D. Awschalom, *Phys. Rev. Lett.* **80**, 4313 (1998).
7. S. A. Crooker, D. D. Awschalom, J. J. Baumberg, *et al.*, *Phys. Rev. B* **56**, 7574 (1997).
8. J. A. Gupta, D. D. Awschalom, X. Peng, *et al.*, *Phys. Rev. B* **59**, R10421 (1999).
9. L. Viña, *J. Phys.: Condens. Matter* **11**, 5929 (1999).
10. M. I. D'yakonov and V. I. Perel', *Zh. Éksp. Teor. Fiz.* **60**, 1954 (1971) [*Sov. Phys. JETP* **33**, 1053 (1971)]; *Fiz. Tverd. Tela (Leningrad)* **13**, 3581 (1971) [*Sov. Phys. Solid State* **13**, 3023 (1971)].
11. G. Dresselhaus, *Phys. Rev.* **100**, 580 (1955).
12. Yu. A. Bychkov and É. I. Rashba, *Pis'ma Zh. Éksp. Teor. Fiz.* **39**, 66 (1984) [*JETP Lett.* **39**, 78 (1984)].
13. M. I. D'yakonov and V. Yu. Kachorovskii, *Fiz. Tekh. Poluprovodn. (Leningrad)* **20**, 178 (1986) [*Sov. Phys. Semicond.* **20**, 110 (1986)].
14. B. Jusserand, D. Richards, G. Allan, *et al.*, *Phys. Rev. B* **52**, 4707 (1995).
15. P. Ramvall, B. Kowalski, and P. Omling, *Phys. Rev. B* **55**, 7160 (1997).
16. M. Z. Maialle, E. A. de Andrada, and L. J. Sham, *Phys. Rev. B* **47**, 15776 (1993).
17. E. L. Ivchenko, *Fiz. Tverd. Tela (Leningrad)* **15**, 1566 (1973) [*Sov. Phys. Solid State* **15**, 1047 (1973)].

Translated by V. Sakun

Phase Transition in Strongly Degenerate Hydrogen Plasma¹

V. S. Filinov, V. E. Fortov, M. Bonitz^{1*}, and P. R. Levashov

High Energy Density Research Center, Joint Institute for High Temperatures, Russian Academy of Sciences,
ul. Izhorskaya 13/19, Moscow, 127412 Russia

¹ Fachbereich Physik, Universität Rostock, D-18051 Rostock, Germany

*e-mail: michael.bonitz@physik.uni-rostock.de

Received August 22, 2001

Direct fermionic path-integral Monte Carlo simulations of strongly coupled hydrogen are presented. Our results show evidence for the hypothetical plasma phase transition. Its most remarkable manifestation is the appearance of metallic droplets, which are predicted to be crucial for the electrical conductivity and allow one to explain the rapid increase found in recent shock compression measurements. © 2001 MAIK “Nauka/Interperiodica”.

PACS numbers: 52.25.Kn; 52.65.Pp

Hydrogen at high pressures remains the subject of many investigations (see, e.g., [1, 2] for an overview). Many interesting phenomena, such as the metal–insulator transition (MIT), the Mott effect and the plasma phase transition (PPT) have been predicted. They occur in situations where both quantum and Coulomb effects are important, making a theoretical analysis difficult. Among the most promising theoretical approaches to such systems is the path-integral quantum Monte Carlo (PIMC) method [3, 4], which has seen remarkable progress recently (e.g., [4, 5]). However, for Fermi systems, these simulations are substantially hampered by the so-called fermion sign problem. Additional assumptions, such as fixed node and restricted path concepts, have been introduced to overcome this difficulty [4]. It can be shown, however, that such assumptions do not reproduce the correct ideal Fermi gas limit [6].

Recently, we presented a new path-integral representation which avoids additional approximations, (direct path-integral Monte Carlo, DPIMC) which has successfully been applied to strongly coupled hydrogen [7–9] (see below). In this work, we apply the DPIMC method to the analysis of dense liquid hydrogen in the region of the hypothetical plasma phase transition [1, 10, 11, 12]. Computing the equation of state and the internal energy, we find clear indications for the existence of the PPT—its first confirmation by a *first-principle* method. It is shown that the PPT manifests itself by the formation of large metallic droplets, which are crucial for plasma transport properties.

It is well known that the thermodynamic properties of a quantum system are fully determined by the partition function Z . For a binary mixture of N_e electrons and

N_i protons, Z can be written as

$$Z(N_e, N_i, V, \beta) = Q(N_e, N_i, \beta) / N_e! N_i!, \quad (1)$$

$$Q(N_e, N_i, \beta) = \sum_{\sigma} \int d\mathbf{q} d\mathbf{r} \rho(\mathbf{q}, \mathbf{r}, \sigma; \beta).$$

Here, $\mathbf{q} \equiv \{\mathbf{q}_1, \mathbf{q}_2, \dots, \mathbf{q}_{N_i}\}$ are the coordinates of the protons; $\sigma \equiv \{\sigma_1, \dots, \sigma_{N_e}\}$ and $\mathbf{r} \equiv \{\mathbf{r}_1, \dots, \mathbf{r}_{N_e}\}$ are the electron spins and coordinates, respectively; and $\beta = 1/k_B T$. The density matrix ρ in Eq. (1) is represented in the common way by a path integral [13]:

$$\rho(\mathbf{q}, \mathbf{r}, \sigma; \beta) = \frac{1}{\lambda_i^{3N_i} \lambda_\Delta^{3N_e}} \sum_P (\pm 1)^{\kappa_P} \times \int_V d\mathbf{r}^{(1)} \dots d\mathbf{r}^{(n)} \rho(\mathbf{q}, \mathbf{r}, \mathbf{r}^{(1)}; \Delta\beta) \dots \dots \rho(\mathbf{q}, \mathbf{r}^{(n)}, \hat{P}\mathbf{r}^{(n+1)}; \Delta\beta) \mathcal{S}(\sigma, \hat{P}\sigma'), \quad (2)$$

where $\Delta\beta \equiv \beta/(n+1)$ and $\lambda_\Delta^2 = 2\pi\hbar^2\Delta\beta/m_e$. Further, $\mathbf{r}^{n+1} \equiv \mathbf{r}^n$, $\sigma' = \sigma$; i.e., electrons are represented by fermionic loops with the coordinates (beads) $[\mathbf{r}] \equiv [\mathbf{r}, \mathbf{r}^{(1)}, \dots, \mathbf{r}^{(n)}, \mathbf{r}]$. The electron spin gives rise to the spin part of the density matrix \mathcal{S} , whereas exchange effects are accounted for by the permutation operator \hat{P} and the sum over the permutations with parity κ_P .

Following [3], we use a modified representation (3) of the high-temperature density matrices on the right-hand side of Eq. (2), which is suitable for the efficient direct fermionic PIMC simulation of plasmas. With the error of the order $\epsilon \sim (\beta R y)^2 \chi / (n+1)$, which vanishes

¹ This article was submitted by the authors in English.

with a growing number of beads, we obtain the approximation

$$\sum_{\sigma} \rho(q, r, \sigma; \beta) = \frac{1}{\lambda_i^{3N_i} \lambda_{\Delta}^{3N_e}} \sum_{s=0}^{N_e} \rho_s(q, [r], \beta),$$

$$\rho_s(q, [r], \beta) = \frac{C_{N_e}^s}{2^{N_e}} e^{-\beta U(q, [r], \beta)} \prod_{l=1}^n \prod_{p=1}^{N_e} \phi_{pp}^l \det |\Psi_{ab}^{n,1}|_s, \quad (3)$$

$$U(q, [r], \beta) = U^i(q) + \sum_{l=0}^n \frac{U_l^e([r], \beta) + U_l^{ei}(q, [r], \beta)}{n+1},$$

where χ is the degeneracy parameter and U^i , U_l^e , and U_l^{ei} denote the sum of the binary Kelbg potentials Φ^{ab} [14, 15] between protons, electrons at vertex “ l ,” and electrons (vertex “ l ”) and protons, respectively.

In Eq. (3), $\phi_{pp}^l \equiv \exp[-\pi |\xi_p^{(l)}|^2]$ arises from the kinetic-energy part of the density matrix of the electron with index p , and we introduced dimensionless distances between the neighboring vertices on the loop, $\xi^{(1)}, \dots, \xi^{(n)}$. Finally, the exchange matrix is given by

$$\|\Psi_{ab}^{n,1}\|_s \equiv \left\| \exp \left\{ -\frac{\pi}{\lambda_{\Delta}^2} |(r_a - r_b) + y_a^n|^2 \right\} \right\|_s,$$

$$\text{with } y_a^n = \lambda_{\Delta} \sum_{k=1}^n \xi_a^{(k)},$$

where the subscript s denotes the number of electrons having the same spin projection. From the above Eqs. (1)–(3), one readily computes the internal energy and the equation of state:

$$\beta E = \frac{3}{2} (N_e + N_i) - \beta \frac{\partial \ln Q}{\partial \beta}, \quad (4)$$

$$\beta p = \frac{\partial \ln Q}{\partial V} = \left[\frac{\alpha}{3V} \frac{\partial \ln Q}{\partial \alpha} \right]_{\alpha=1}. \quad (5)$$

In our simulations, we used $N_e = N_i = 50$ and $n = 20$. To test the MC procedure, we considered a mixture of *ideal* degenerate electrons and classical protons, for which the thermodynamic quantities are known analytically. The agreement, up to the degeneracy parameter χ as large as 10, was very good and improved with increasing number of particles [7]. Further, the method was successfully tested in applications to electrons in a harmonic trap [16]. For the case of *interacting* electrons and protons in dense hydrogen, we previously performed a series of calculations over a wide range of the classical coupling parameter Γ and degeneracy χ for temperatures $T \geq 10000$ K. The analysis of the results clearly showed a number of interesting phenomena,

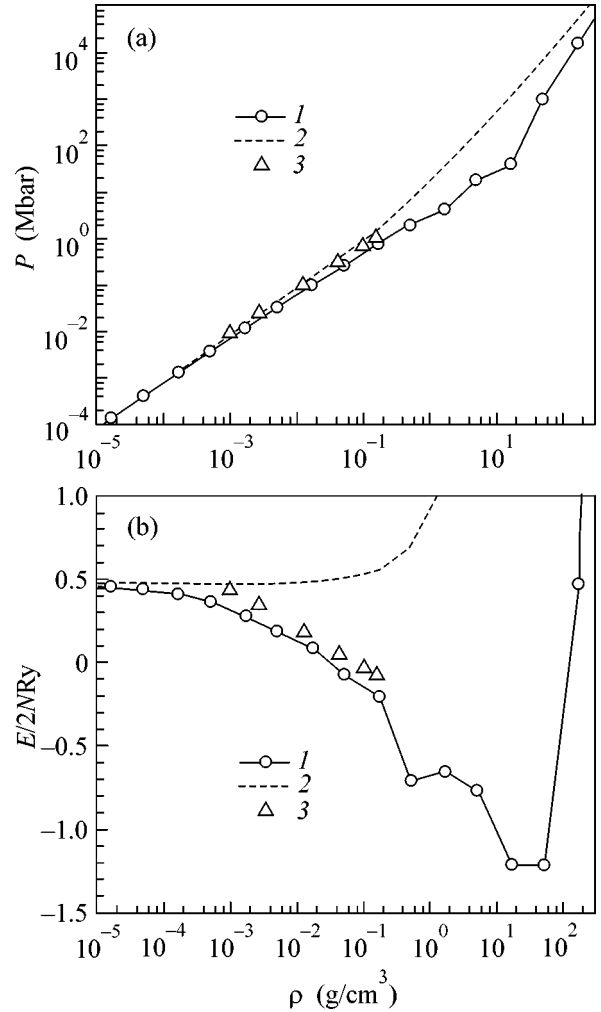


Fig. 1. (a) Pressure and (b) internal energy for hydrogen plasma at $T = 5 \times 10^4$ K vs. density. (1) Direct PIMC simulation of this work, (2) ideal plasma, and (3) restricted PIMC computations at $T = 6.25 \times 10^4$ K [17].

such as formation and decay of hydrogen bound states [8, 9, 15], including hydrogen atoms, molecules, molecular ions, clusters and, further, at high densities, pairing of electrons and ordering of protons into a Wigner crystal [9].

In this work, we present new results which concentrate on the hypothetical plasma phase transition [10]. For this purpose, we analyze the plasma properties and compute the equation of state (5) and internal energy (4) of dense hydrogen along two isotherms, $T = 10^4$ K and 5×10^4 K. Figure 1 shows pressure and energy vs. density at $T = 5 \times 10^4$ K. For comparison, we also include the results for an ideal plasma. As expected, due to Coulomb interaction and bound-state formation, the nonideal plasma results are below the ideal ones. We mention that our results are in good agreement with the restricted path-integral calculations of Militzer and Ceperley (Fig. 1a contains available data points for a

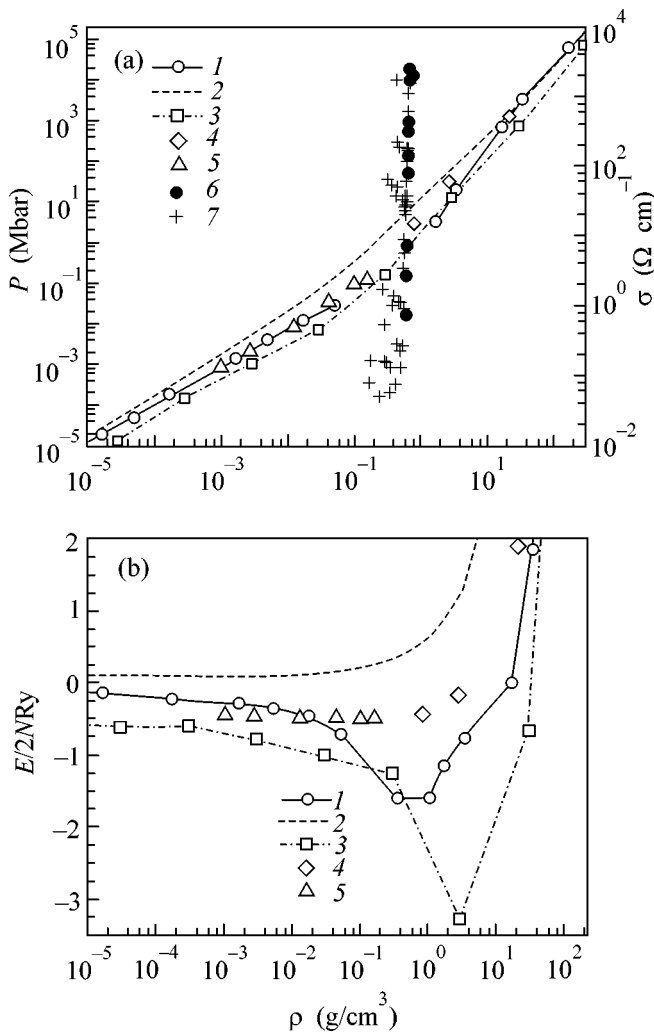


Fig. 2. (a) (1–5) Pressure and (6, 7) electrical conductivity and (b) internal energy for hydrogen at $T = 10^4$ K vs. density. (1) Direct PIMC simulation of this work, (2) ideal plasma, (3) direct PIMC simulation of a mixture consisting of 25% helium and 75% hydrogen, (4) density functional theory [20], (5) restricted PIMC computations [17], (6, 7) electrical conductivity of hydrogen (right axis), (6) [18], and (7) [19].

slightly higher temperature of 6.25×10^4 K [17]). For higher temperatures, agreement is very good [15]. More importantly, at this temperature, pressure increases monotonically with density, and, at high densities, a continuous increase in the degree of ionization (Mott effect) is found.

However, at $T = 10^4$ K, the properties of the hydrogen plasma change qualitatively (cf. Figs. 2, 3). While the overall trend of the pressure (Fig. 2a) is still a monotonic increase, in the density region of $0.1 \dots 1.5 \text{ g/cm}^3$ the plasma exhibits unusual behavior. Inside this region, the Monte Carlo simulations do not converge to an equilibrium state; the pressure strongly fluctuated

and reached even negative values. Such behavior is typical for Monte Carlo simulations of metastable systems.

Note that no such peculiarities appear for densities below and above this interval, as well as for the isotherm $T = 5 \times 10^4$ K and for higher temperatures.

These facts suggest that our simulations encountered the plasma phase transition predicted by many chemical models of partially ionized hydrogen, e.g., in [1, 10, 11, 12]. According to these models, this is a first-order transition with two coexisting phases of different degrees of ionization. While canonical Monte Carlo simulations do not yield the coexisting phases and the coexistence pressure directly, they allow one to analyze in detail the actual microscopic particle configurations. A typical particle arrangement inside the instability region, $T = 10^4$ K and $\rho = 0.3346 \text{ g/cm}^3$, is shown in Fig. 3. Obviously, the protons arrange themselves into large clusters (droplets), with the electrons (the piecewise linear lines show their closed fermionic path) being fairly delocalized over the cluster. This is a clear precursor of the metal-like state, which is found in the simulations for densities above the instability region.

As mentioned above, the plasma phase transition appears in many chemical models in the same density–temperature range. However, these simple approaches become questionable in the region of pressure ionization and dissociation, where the consistent treatment of all possible pair interactions, including charge–charge, neutral–neutral, and charge–neutral, is crucial. Furthermore, these approaches neglect larger bound aggregates such as clusters, which our simulations reveal to be crucial in the metastable region. We mention that indirect indications for a phase transition have been found in recent density-functional studies [20]. In this work, the thermodynamic properties of hydrogen in the metallic phase were computed (see data points in Fig. 2), and enhanced long-wavelength ion density fluctuations were observed as the density was reduced to $\rho = 0.799 \text{ g/cm}^3$ (the lowest density explored). This led to unusual behavior of the ion–ion structure factor and the effective potential, which the authors of [20] interpreted as a possible precursor to an incipient metal-to-insulator transition.

Our simulations suggest that the existence of the PPT should have a noticeable influence on the transport properties. In fact, when the density changes from $0.1 \dots 1.5 \text{ g/cm}^3$, hydrogen transforms from a neutral into a metallic fluid. Accordingly, electrical conductivity should increase rapidly. Indeed, shock compression experiments have revealed a dramatic increase in the electrical conductivity by 4–5 orders of magnitude in a very narrow density range of $0.3 \text{--} 0.5 \text{ g/cm}^3$ [18, 19]. So far, theoretical models cannot reproduce this behavior correctly, predicting either a too early (hopping conductivity in the molecular fluid) or too late (free electron conductivity) increase [21]. But, seeing as the experimental data (black circles and crosses in Fig. 2a) are located right inside the PPT region, one has to take

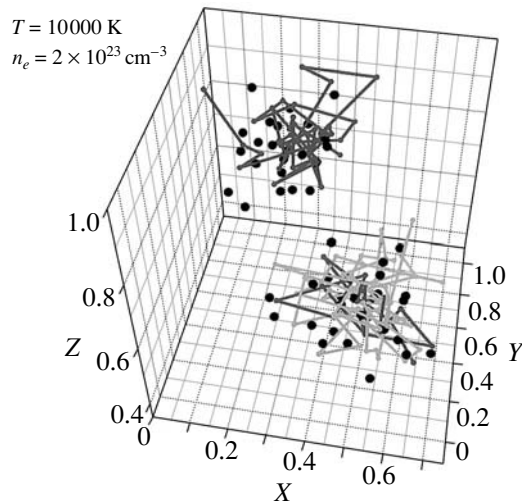


Fig. 3. Snapshot of a Monte Carlo cell at $T = 10^4$ K and $\rho = 0.3346$ g/cm³. Black circles are protons, and dark and light broken lines are representations of electrons as fermionic loops with different spin projections.

into account a third conductivity mechanism—charge transport via electron hopping between individual metal-like droplets. Obviously, this mechanism will be effective in between the regions where the two other effects dominate and thus should allow for a much better agreement with the experiments.

Finally, we mention that our simulations predict a PPT for pure hydrogen plasma only. In contrast, no PPT was found for a binary mixture of 25% of helium and 75% of hydrogen atoms (cf. Fig. 2).

In summary, we have presented direct path-integral Monte Carlo simulations of dense fluid hydrogen in the region of the MIT. Our results give evidence for the plasma phase transition, which, to the best of our knowledge, is its first prediction by a *first principle* theory. Most importantly, we found clear evidence for the formation of large metallic droplets which are predicted to play a crucial role in transport and optics in the region of the MIT at low temperatures. In further investigations, we will focus on a more precise analysis of the MIT and the plasma phase transition, including determination of its critical point and the transport and optical properties of the droplets.

This paper is dedicated to Werner Ebeling on the occasion of his 65th birthday. We are grateful to W. Ebeling, D. Kremp, W.D. Kraeft, and S. Trigger for

stimulating discussions. We also wish to thank D. Ceperley and B. Militzer for useful critical remarks.

REFERENCES

1. W. D. Kraeft, D. Kremp, W. Ebeling, and G. Röpke, *Quantum Statistics of Charged Particle Systems* (Akademie-Verlag, Berlin, 1986).
2. *Strongly Coupled Coulomb Systems*, Ed. by G. Kalman (Pergamon, New York, 1998).
3. V. M. Zamalin, G. E. Norman, and V. S. Filinov, *The Monte-Carlo Method in Statistical Thermodynamics* (Nauka, Moscow, 1977).
4. D. Ceperley, in *The Monte-Carlo and Molecular Dynamics of Condensed Matter Systems*, Ed. by K. Binder and G. Ciccotti (SIF, Bologna, 1996), p. 447.
5. *Classical and Quantum Dynamics of Condensed Phase Simulation*, Ed. by B. J. Berne, G. Ciccotti, and D. F. Coker (World Scientific, Singapore, 1998).
6. V. S. Filinov, *J. Phys. A* **34**, 1665 (2001).
7. V. S. Filinov, P. R. Levashov, V. E. Fortov, and M. Bonitz, in *Progress in Nonequilibrium Green's Functions*, Ed. by M. Bonitz (World Scientific, Singapore, 2000).
8. V. S. Filinov, V. E. Fortov, M. Bonitz, and D. Kremp, *Phys. Lett. A* **274**, 228 (2000).
9. V. S. Filinov, M. Bonitz, and V. E. Fortov, *Pis'ma Zh. Éksp. Teor. Fiz.* **72**, 361 (2000) [*JETP Lett.* **72**, 245 (2000)].
10. G. E. Norman and A. N. Starostin, *Teplofiz. Vys. Temp.* **8**, 413 (1970).
11. M. Schlanges, M. Bonitz, and A. Tschtschjan, *Contrib. Plasma Phys.* **35**, 109 (1995).
12. D. Saumon and G. Chabrier, *Phys. Rev. A* **46**, 2084 (1992).
13. R. P. Feynman and A. R. Hibbs, *Quantum Mechanics and Path Integrals* (McGraw-Hill, New York, 1965).
14. G. Kelbg, *Ann. Phys. (Leipzig)* **12**, 219 (1963); **13**, 354 (1963); **14**, 394 (1964).
15. For a detailed discussion, see V. S. Filinov, M. Bonitz, W. Ebeling, and V. E. Fortov, *Plasma Phys. Controlled Fusion* **43**, 743 (2001).
16. A. Filinov, M. Bonitz, and Yu. E. Lozovik, *Phys. Rev. Lett.* **86**, 3851 (2001).
17. B. Militzer and D. M. Ceperley, *Phys. Rev. E* **63**, 066404 (2001).
18. S. T. Weir, A. C. Mitchell, and W. J. Nellis, *Phys. Rev. Lett.* **76**, 1860 (1996).
19. V. Ya. Ternovoi, A. S. Filimonov, V. E. Fortov, *et al.*, *Physica B (Amsterdam)* **265**, 6 (1999).
20. H. Xu and J. P. Hansen, *Phys. Rev. E* **57**, 211 (1998).
21. R. Redmer, G. Röpke, S. Kuhlbrodth, and H. Reinholz, *Contrib. Plasma Phys.* **41**, 163 (2001).

Spectral Luminescence Properties of Nanostructured Ce–Nd-Containing Silica Gel-Glasses

G. E. Malashkevich*, G. I. Semkova, V. E. Gaishun, and A. V. Mudryi

Institute of Molecular and Atomic Physics, National Academy of Sciences of Belarus, Minsk, 220072 Belarus

*malash@imaph.bas-net.by

Received August 29, 2001

Complex Ce^{4+} – Nd^{3+} centers were formed in silica gel-glasses. These centers were characterized by weak cross-relaxation quenching of luminescence; an increased luminescence branching ratio in the ${}^4F_{3/2} \rightarrow {}^4I_{11/2}, {}^4I_{13/2}$ transitions; strong structuring of the analogous spectral bands; and effective intracenter sensitization of luminescence. On reducing the Ce^{4+} ions to the triply charged state, the structure of the luminescence bands of Nd^{3+} ions became weaker and the ratio of their intensities approached the value typical of an Nd-containing silica gel-glass. © 2001 MAIK "Nauka/Interperiodica".

PACS numbers: 78.67.-n; 78.55.-m

Nanostructuring may impart new spectral luminescence properties to Ln-containing glasses untypical of disordered materials, which may considerably raise the competitiveness of the corresponding glass lasers and light transformers. Among the problems that can be solved by nanostructuring are obtaining Nd-containing glasses with an increased fraction of quanta emitted in the ${}^4F_{3/2} \rightarrow {}^4I_{13/2}$ transition ($\lambda \sim 1.34 \mu\text{m}$) and glasses characterized by efficient UV excitation of IR luminescence. These problems have remained topical for years for a number of practical applications. They are also of great interest from the viewpoint of materials science.

This work is devoted to an attempt to obtain such glasses using the possibility of forming complex Ce^{4+} – Nd^{3+} centers in silica gel-glasses, which was discovered recently [1–4], where Ln = Ce, Sm, and Eu. These centers are characterized by increased symmetry of Ln(III) oxo complexes and by efficient sensitization of their luminescence by photoreduced metastable ions (Ce^{4+}), which absorb in the UV spectral region.

Test samples were prepared by direct sol–gel–glass transition using the known method [2]. Activation was performed by impregnating porous xerogels with solutions of neodymium and cerium compounds. The xerogels were sintered in oxygen to a transparent glassy state. The Ce^{4+} ions were reduced to Ce^{3+} by annealing the glasses in hydrogen. The concentration of activators N was determined in layers using a Spectroscan spectrometer with a limiting error of measurements of $\pm 15\%$ and was averaged over the volume. All the reagents were of high-purity grade. The phase composition of the glasses was monitored using a DRON-2.0 X-ray diffractometer and an S-806 scanning electron microscope.

Light attenuation spectra were recorded on a Cary-500 spectrophotometer and were represented as the dependence of the natural light attenuation coefficient k on the wavelength λ . The luminescence and luminescence excitation spectra were recorded on an SDL-2 spectrofluorimeter, corrected [5], reduced to unity at a maximum, and represented as the dependence of the number of quanta per unit interval of wavelengths $dn/d\lambda$ on λ . In order to diminish the luminescence quenching of the coactivated samples, frontal excitation was used and their thickness was decreased to 0.3 mm. The luminescence quantum yield η of Nd^{3+} ions was determined by the comparison method [5]. A certified GLS-22 glass was used as the reference standard. All the spectral measurements were carried out at $T = 298 \text{ K}$.

The light attenuation spectra of the glasses studied in this work are shown in Fig. 1. It is evident that a significant excess of the intensity of the "supersensitive" ${}^4I_{9/2} \rightarrow {}^4G_{5/2}, {}^2G_{7/2}$ band ($\lambda_{\text{max}} \approx 580 \text{ nm}$) of Nd^{3+} ions over the intensity of the other bands (curve 1) is characteristic of the monoactivated glass with $N_{\text{Nd}} = 2 \times 10^{19} \text{ ion/cm}^3$. A considerable attenuation of both the relative intensity of the supersensitive band indicated above and the integral intensity of f – f bands reduced to one Nd^{3+} ion is observed for the coactivated glass with $N_{\text{Nd}} = 0.5N_{\text{Ce}} = 1.5 \times 10^{20} \text{ ion/cm}^3$ (curve 2). At the same time, the structure of the IR bands of Nd^{3+} ions becomes enhanced, and an intense UV band appears with an adjacent structureless weak band stretching over the entire visible region. The annealing of this glass in hydrogen leads to a strong weakening and narrowing of the UV band and to the disappearance of diffuse absorption in the visible region but only weakly affects the relative intensities and the structure of bands

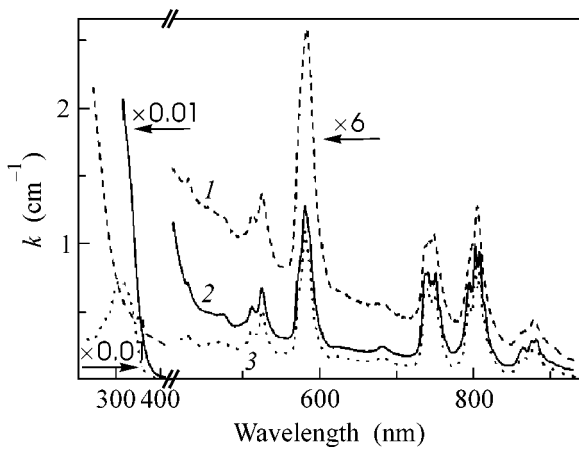


Fig. 1. Light attenuation spectra of (1) Nd- and (2, 3) Ce-Nd-containing glasses (2) before and (3) after annealing in hydrogen; N_{Nd} , 10^{19} ions/cm 3 : (1) 2 and (2, 3) 15; N_{Ce} (2, 3) = 3×10^{20} ion/cm 3 .

associated with Nd^{3+} ions (curve 3). Note that an increase in N_{Nd} up to 4×10^{20} ion/cm 3 in the monoactivated glass is also accompanied by a decrease in the relative intensity of the supersensitive band and in the specific absorption of Nd^{3+} ions; however, it hardly affects the structure of their spectral bands.

The IR luminescence spectra of the glasses under study are shown in Fig. 2. It can be seen that the spectrum of the monoactivated glass on excitation by non-selective radiation in the range 300–750 nm (a DKSSh-100 xenon lamp and an SZS25 light filter) is represented by three weakly structured bands (curve 1), the most intense of which corresponds to the $^4F_{3/2} \rightarrow ^4I_{9/2}$ transition of Nd^{3+} ions ($\lambda_{\text{max}} \approx 905$ nm). The fourth band at 1900 nm is more than two orders of magnitude weaker and is not shown in the figure. The character of this spectrum is retained on selective excitation in the above region with the half-width of the exciting radiation band equal to 2 nm. This spectroscopic behavior of the monoactivated glass is also observed at high N_{Nd} . The spectrum of the coactivated glass on nonselective excitation is distinguished by the presence of new narrow components and by redistribution of the integral intensities of spectral bands. These changes are most pronounced on excitation by radiation with the wavelength $\lambda_{\text{exc}} \leq 400$ nm (curve 2). It is remarkable that the position of new narrow components for the coactivated glass only slightly varies on scanning λ_{exc} . After annealing this glass in hydrogen, the structure of spectral bands becomes weaker (curve 3), and the distribution of their relative intensities approaches a distribution characteristic of monoactivated glasses.

The IR luminescence excitation spectra of the glasses under study are presented in Fig. 3. It can be

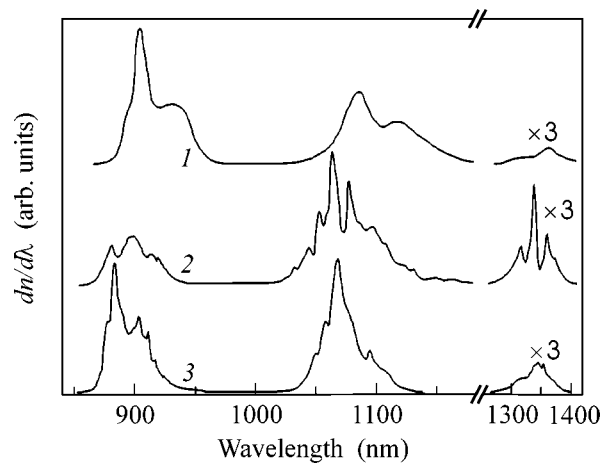


Fig. 2. Normalized and corrected IR luminescence spectra of (1) Nd- and (2, 3) Ce-Nd-containing glasses (2) before and (3) after annealing in hydrogen; N_{Nd} , 10^{19} ions/cm 3 : (1) 2 and (2, 3) 15; N_{Ce} (2, 3) = 3×10^{20} ions/cm 3 ; λ_{exc} , nm: (1) 300–750 and (2, 3) 370.

seen that the spectrum of the monoactivated glass (curve 1) at the recording wavelength λ_{rec} corresponding to the $^4F_{3/2} \rightarrow ^4I_{11/2}$ band of Nd^{3+} ions ($\lambda_{\text{max}} \approx 1085$ nm) differs from the corresponding absorption spectrum both in the ratio between the intensities of spectral bands of the activator (the relative intensity of the supersensitive band increases) and in their shape. The partial intensities of the main spectral bands of Nd^{3+} ions in the spectrum of the coactivated glass at $\lambda_{\text{rec}} = 1340$ nm (curve 2) come close together, and an intense and broad UV band appears. The annealing of this glass in hydrogen leads to a change in the position

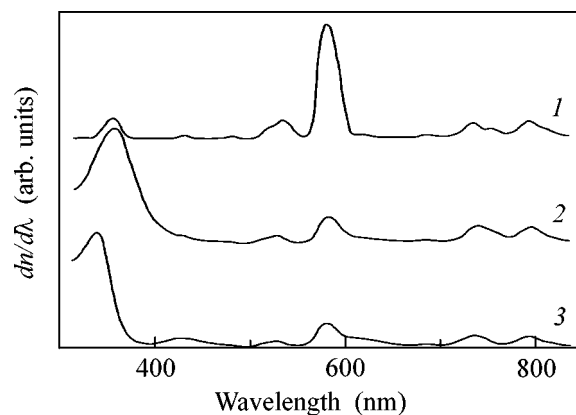


Fig. 3. Normalized and corrected IR luminescence excitation spectra of (1) Nd- and (2, 3) Ce-Nd-containing glasses (2) before and (3) after annealing in hydrogen; N_{Nd} , 10^{19} ions/cm 3 : (1) 2 and (2, 3) 15; N_{Ce} (2, 3) = 3×10^{20} ions/cm 3 ; λ_{rec} , nm: (1) 1075 and (2, 3) 1340.

and shape of the UV band and produces noticeable changes in the contours of f - f bands (curve 3).

The results presented above must be supplemented with the statement that no crystalline phase was found in all the samples studied. For the monoactivated glass excited in the ${}^4I_{9/2} \rightarrow {}^4F_{3/2}$ band, the value of η comprises $\approx 5\%$ at $N_{\text{Nd}} = 2 \times 10^{19}$ ion/cm³ and decreases down to 0.5% at $N_{\text{Nd}} = 4 \times 10^{20}$ ion/cm³. For the monoactivated glass sintered in oxygen, this value is close to 15% under similar excitation conditions. When this glass is excited in the UV band ($\lambda_{\text{exc}} = 355$ nm), the value of η decreases down to 5% and approaches 15% again after annealing in hydrogen. Also note that the concentration of hydroxyl ions determined by the known method [2] comprises ≈ 0.8 wt % for the glasses under study.

The radical differences of the spectra of the coactivated glass sintered in oxygen from the corresponding spectra of the monoactivated glass caused by Nd³⁺ ions (compare curves 1 and 2 in Figs. 1–3) should be associated with the formation of complex Ce⁴⁺-Nd³⁺ centers. The appearance of these centers is due to the relatively small ionic radius of the quadruply charged cerium (~ 0.8 Å [6]). According to the geometrical criterion [7], this allows cerium to form seven- and, possibly, six-coordinate polyhedra with oxygen. In this case, according to the consequence [8] from Pauling's electrostatic valence rule, the Ce⁴⁺ ions can serve as buffer elements, favoring the entry of higher coordinate lanthanide ions into a rigid silicon-oxygen framework and, thus, the formation of such complex centers. The results that we obtained recently¹ in studying the vibronic interaction of 4f electrons of Eu³⁺ ions with the environment in Ce⁴⁺-Eu³⁺ centers of a silica gel-glass point to the displacement of Si-O structural units outside these centers. This fact, with regard to the absence of evidence of crystallization in the glasses under study, suggests that such complex centers represent oxide nanoparticles in which Ln³⁺ ions are surrounded by Ce(IV) oxo complexes. The attenuation of the supersensitive band and the specific absorption of Nd³⁺ ions observed in this case (compare curves 1 and 2 in Fig. 1) indicate that the symmetry of Nd(III) oxo complexes in these nanoparticles is increased. In our opinion, this increase is due to the fact that the covalent character of the Ce⁴⁺-O²⁻ chemical bond is relatively low and, according to [9], comprises $\approx 33\%$. It counts in favor of this interpretation that no increase in the symmetry of Nd(III) is observed in silica gel-glasses when six-coordinate Al³⁺ ions are used as a buffer [10]. The degree of covalent character of these ions in compounds with oxygen is close to 41%. The occurrence of the nanoparticles indicated above explains why the luminescence spectra exhibit no continuous variation in going from one complex center to another one within their ensem-

ble. It also explains the fact that the value of η for the coactivated glasses is considerably greater than that for the Nd-containing ones, for which the formation of Nd-Nd centers, with luminescence quenched because of cross-relaxation interactions, is typical [10].

The presence of an intense UV band in the IR luminescence excitation spectrum of Ce⁴⁺-Nd³⁺ centers (see curve 2 in Fig. 3) points to the efficient intracenter transfer of excitations to Nd³⁺ ions. It is known that Ce⁴⁺ ions do not luminesce [2]; therefore, this transfer can proceed only from labile photoreduced ions (Ce⁴⁺)⁻, whose absorption spectrum is close to the analogous spectrum of Ce³⁺ ions [11]. The absence of the ability of Nd³⁺ ions to decrease their charge state in glasses suggests a superexchange mechanism of this transfer with simultaneous electron return from the ground state (Ce⁴⁺)⁻ to a ligand. The overlap between electron orbitals of the donor and acceptor necessary for the given mechanism can be accomplished through the bonding of Ce⁴⁺ and Nd³⁺ ions by a bridging oxygen atom with the formation of a configuration close to collinear [12]. A weak change in the relative intensity of the UV excitation band due to annealing of the coactivated glass in hydrogen (compare curves 2 and 3 in Fig. 3) can be reasonably explained by the closeness of the excited states of (Ce⁴⁺)⁻ and Ce³⁺ ions in energy, the good resonance of these states with the close-lying states of Nd³⁺ ions, and the insignificant change of the distance between the coactivators on reducing Ce⁴⁺ to Ce³⁺. In this case, the considerable decrease in the splitting of the luminescence bands of Nd³⁺ ions after the annealing of the coactivated glass in hydrogen (compare curves 2 and 3 in Fig. 2) is, in the main, the consequence of a decrease in the field strength of their environment. As for the modification of the spectral bands at $\lambda \sim 430$ and 620 nm (compare curves 1 and 3 in Fig. 3) that is untypical for such an activator as Nd³⁺ ions, additional investigations are necessary for its interpretation.

From the practical point of view, the relatively high luminescence branching ratio ($\approx 15\%$) [13] in the ${}^4F_{3/2} \rightarrow {}^4I_{13/2}$ transition is the most attractive property of the Ce⁴⁺-Nd³⁺ centers formed in this work. This property is important in creating lasers and amplifiers for optical transmission lines at a wavelength corresponding to the minimum material dispersion of silica glass. It is also reasonable to believe that a decrease in the concentration of Ce⁴⁺-O-Ce³⁺ and Ce⁴⁺-O-Fe³⁺ groups, which absorb in the UV, visible, and, partially, in the near IR spectral regions [14], as well as the use of special dehydration methods, must significantly increase the value of η for glasses with the Ce⁴⁺-Nd³⁺ centers considered above.

This work was partially supported by the Belarusian Republican Foundation for Basic Research, project no. F00-186.

¹ These results will be published in a separate work.

REFERENCES

1. G. E. Malashkevich, E. N. Poddenezhnyĭ, I. M. Mel'nichenko, *et al.*, *Opt. Spektrosk.* **78**, 84 (1995) [*Opt. Spectrosc.* **78**, 74 (1995)].
2. G. E. Malashkevich, E. N. Poddenezhnyĭ, I. M. Mel'nichenko, *et al.*, *J. Non-Cryst. Solids* **188**, 107 (1995).
3. G. E. Malashkevich, E. N. Poddenezhnyĭ, I. M. Mel'nichenko, *et al.*, *Fiz. Tverd. Tela (St. Petersburg)* **40**, 458 (1998) [*Phys. Solid State* **40**, 420 (1998)].
4. G. E. Malashkevich, A. G. Makhaneĭ, A. V. Semchenko, *et al.*, *Fiz. Tverd. Tela (St. Petersburg)* **41**, 229 (1999) [*Phys. Solid State* **41**, 202 (1999)].
5. C. A. Parker, *Photoluminescence of Solutions* (Elsevier, Amsterdam, 1968; Mir, Moscow, 1972).
6. *Chemistry and Periodic Table*, Ed. by K. Saito (Iwanami Shoten, Tokyo, 1979; Mir, Moscow, 1982), translated from Japanese.
7. B. K. Vainshteĭn, V. M. Fridkin, and V. L. Indenbom, *Modern Crystallography*, Vol. 2: *Structure of Crystals*, Ed. by B. K. Vainshteĭn, A. A. Chernov, and L. A. Shuvalov (Nauka, Moscow, 1979; Springer-Verlag, Berlin, 1982).
8. L. E. Ageeva, V. I. Arbuzov, E. I. Galant, *et al.*, *Fiz. Khim. Stekla* **13**, 409 (1987).
9. N. N. Ermolenko, *Steklo, Sitaly Silik. Mater.* **5**, 3 (1976).
10. G. E. Malashkevich, P. P. Pershukevich, E. N. Poddenezhnyĭ, *et al.*, *Zh. Prikl. Spektrosk.* **62**, 61 (1995).
11. V. I. Arbuzov, M. N. Tolstoĭ, M. A. Élerts, *et al.*, *Fiz. Khim. Stekla* **13**, 581 (1987).
12. M. S. Poluéktov, N. P. Efryushina, and S. A. Gava, *Determination of Lanthanide Microquantity by Luminescence of Crystal Phosphors* (Naukova Dumka, Kiev, 1976).
13. G. E. Malashkevich, N. V. Ovcharenko, T. V. Smirnova, *et al.*, *Fiz. Khim. Stekla* **17**, 52 (1991).
14. G. E. Malashkevich, G. I. Semkova, and W. Streck, *J. Alloys Compd.* (2001) (in press).

Translated by A. Bagatur'yants

Effect of Coulomb Interaction on the Electron Spectral Density and the Transverse Conductivity of Layered Metals

S. N. Artemenko* and S. V. Remizov

Institute of Radio Engineering and Electronics, Russian Academy of Sciences, Moscow, 101999 Russia

*art@cplire.ru

Received August 30, 2001

Interaction of electrons with strongly anisotropic plasma oscillations leads to an incoherent contribution to the electron spectral density that does not vanish even for energies distant from the Fermi surface. In the superconducting state, this gives a peak–dip–hump structure analogous to that observed in layered high- T_c superconductors. The incoherent part of the spectral density and electron transitions with the participation of plasmons are responsible for two mechanisms of the occurrence of a finite conductivity in the transverse direction at high voltages or frequencies. © 2001 MAIK “Nauka/Interperiodica”.

PACS numbers: 73.21.-b; 73.63.-b; 71.45.Gm

Layered metals can be considered as strongly anisotropic crystals with a small transfer integral between layers, which determines the electron band width in the transverse direction. In pure crystals, electron transitions between layers must be coherent as distinct from artificial rough tunnel junctions, in which the parallel momentum component is not conserved in transitions between layers. It is known that an electron oscillates in an electric field applied to a perfect periodic crystal, and the dissipative current does not arise. A finite resistance (and the real part of conductivity) in the direction perpendicular to layers arises because of electron scattering. At frequencies higher than the inverse momentum scattering time $1/\tau$, the scattering efficiency decreases; therefore, the real part of conductivity must drop with increasing frequency. Similarly, if the voltage drop across one layer $V > \hbar/e\tau$, the period of electron oscillations in the electric field becomes smaller than τ and the conductivity must also drop as the voltage further increases. However, in one of the most extensively studied types of layered metals, namely, in high- T_c superconductors, a finite conductivity is observed even at voltages that exceed the value of the superconducting gap [1–4], which, in its turn, exceeds \hbar/τ . The real, dissipative part of the conductivity does not drop even at high frequencies [5]. A similar behavior was also observed in the layered metal 2H-TaSe₂ [6].

In addition, a peak–dip–hump structure extending up to energies distant from the Fermi surface was observed in the electron spectral density of a high- T_c superconductor measured by angle-resolved photoemission spectroscopy [7]. A similar structure was observed earlier using tunnel spectroscopy [8]. The occurrence of an extended incoherent part of the spectral density can explain the finite value of the dissipative current at high frequencies [9]. In works by Nor-

man *et al.* [10], it was shown that the features of the spectral density could be due to the interaction of electrons with a dispersionless boson mode presumably of an electron origin.

We propose a mechanism of the occurrence of the features under discussion not associated with the specific properties of high- T_c superconductors, that is, common to layered metals. This mechanism is based on the Coulomb interaction and the interaction of electrons with strongly anisotropic plasma oscillations. Such oscillations must be inherent in strongly anisotropic layered metals, because the frequency of plasma oscillations with the wave vector perpendicular to the conducting layers is proportional to the small transfer integral squared and, correspondingly, to the conductivity in this direction. Such plasma oscillations in the superconducting state are manifested in the Josephson plasma mode in the high- T_c superconductor [11, 12]. It is evident that an analogous, weakly damped mode must also exist in the normal state at frequencies higher than the collision frequency and at wavelengths shorter than the mean free path, that is, in the limit when the material behaves as an ideal metal, whose response to an electric field is in many respects similar to the response of a superconductor.

Consider a layered metal with the period s in the direction perpendicular to the metallic layers coupled with a small transfer integral t_\perp . The Hamiltonian of the system takes the form

$$\mathcal{H} = \sum_{\mathbf{p}, n, \sigma} \left[\frac{p^2}{2m} a_{\mathbf{p}n\sigma}^+ a_{\mathbf{p}n\sigma} + t_\perp (a_{\mathbf{p}, n+1, \sigma}^+ a_{\mathbf{p}n\sigma} + a_{\mathbf{p}, n-1, \sigma}^+ a_{\mathbf{p}n\sigma}) \right] + \mathcal{H}_C + \mathcal{H}_{BCS}, \quad (1)$$

where $a_{\mathbf{p},n,\sigma}^+$ is the creation operator of an electron with the momentum component p along the layer and the spin σ in the conducting layer n , \mathcal{H}_C describes the Coulomb interaction, and \mathcal{H}_{BCS} is the BCS part of the Hamiltonian, which lead to singlet pairing. For simplicity, we will use a discrete potential of the Coulomb interaction of the electrons occurring in the n and n' layers and separated by the distance r_{\parallel} in the plane of layers $V_C(r_{\parallel}, n) = e^2/\sqrt{r_{\parallel}^2 + (n - n')^2 s^2}$. The Fourier transform of the potential takes the form

$$V_C(\mathbf{q}) = 4\pi e^2/(q_{\parallel}^2 + \hat{q}_{\perp}^2), \quad (2)$$

where q_{\parallel} is the wave vector in the plane of layers, and $\hat{q}_{\perp} = (2/s)\sin(q_{\perp}s/2)$, $|q_{\perp}| < \pi/s$ is the wave vector obtained by a discrete Fourier transform over the layer numbers.

We will neglect electron scattering by impurities and phonons, because the considerable energies that will be required in calculations are high as compared with \hbar/τ . We also omit the renormalization of the effective mass and the broadening of the quasiparticle peak in the electron spectral density due to electron–electron scattering. Instead, we will focus on the effects associated with the plasma mode and its interaction with electrons.

First, we will calculate the polarization operator within the random phase approximation and find the renormalized Coulomb interaction \mathcal{V}_C at zero temperature. In the normal state and in the dynamic limit $\omega \gg q_{\parallel}v_F$, we will obtain

$$\begin{aligned} \mathcal{V}_C(\omega, \mathbf{q}) &= \frac{4\pi e^2}{(q_{\parallel}^2 + \hat{q}_{\perp}^2)\omega^2 - \omega_{\mathbf{q}}^2}, \\ \omega_{\mathbf{q}}^2 &= \frac{\omega_p^2 \hat{q}_{\perp}^2 + \Omega_p^2 q_{\parallel}^2}{q_{\parallel}^2 + \hat{q}_{\perp}^2}, \end{aligned} \quad (3)$$

where $\Omega_p^2 = 2e^2 v_F p_F / s = 4\pi e^2 n / m$ is the plasma frequency for the orientation of the wave vector parallel to the layers, and $\omega_p = (4t_{\perp} s / \hbar v_F) \Omega_p \ll \Omega_p$ is that for the orientation of the wave vector perpendicular to the layers. The poles of the potential given by Eq. (3) determine the spectrum of the plasma mode. Large values of $q_{\perp} \sim s^{-1}$ make the greatest contribution to integrals in the subsequent calculations. At such q_{\perp} , the frequency of the mode grows almost linearly with q_{\parallel} in the wide range between ω_p and Ω_p , and the characteristic velocity of plasmons in the plane of layers is determined by the value $\omega_{\mathbf{q}} \approx q_{\parallel} \Omega_p / \hat{q}_{\perp}$, where $\kappa^2 = \Omega_p^2 / 2 v_F^2$, and $1/\kappa$ is the Thomas–Fermi screening length, which, for simplicity, we consider small compared to the period s , $\kappa s \gg 1$. This relation is true for high- T_c superconductors, where an estimate gives $\kappa \sim 10 \text{ nm}^{-1}$ and $s \sim 1.5 \text{ nm}$.

Note that $\tilde{c} \sim (\kappa s) v_F$, and this fact allows us to use the dynamic limit in Eq. (3).

Note a certain analogy between the interaction of electrons with photons in quantum electrodynamics and the interaction of electrons with plasmons in our problem. However, the interaction in the first case is characterized by the small parameter $e^2/\hbar c = 1/137$, whereas the corresponding parameter in our case $e^2/\hbar \tilde{c} \sim (e^2/s)/\hbar \Omega_p$ can be large or small, depending on the value of the plasma frequency, that is, on the density of charge carriers. First, we consider the case of a relatively good metal with a high plasma frequency when this parameter is small. Next, we will consider the situation when the carrier density decreases.

The renormalized potential in the superconducting state at $\omega, q v_F \ll \Delta$ takes the form $\mathcal{V}_C = 4\pi e^2/(q_{\parallel}^2 + \hat{q}_{\perp}^2 + \kappa^2)$; that is, it describes static screening, and the poles determining the plasma mode are absent. These poles appear only at $\omega, q v_F \gg \Delta$, when superconductivity is of little importance. Note that the Josephson plasma mode at small frequencies with the spectrum given by Eq. (3) is, nevertheless, present and is revealed in the poles of the Green function, which describes fluctuations of the superconducting momentum. These fluctuations also make a contribution to the effects studied here; however, this contribution is small compared with the Coulomb effects by the parameter $(\kappa s)^2$.

Consider the effect of the Coulomb interaction on the electronic structure by the perturbation theory, calculating the mass operator Σ . The poles of the potential \mathcal{V}_C , which acquires the properties of a boson Green function, make the main contribution to Σ . The calculated mass operator does not decrease up to very high energies of order Ω_p , and it gives the following electron Green function in the normal state at energies much less than Ω_p :

$$\begin{aligned} G &= \frac{1}{(\varepsilon - \xi_p)[1 + g_0 + igF(\varepsilon - \xi_p)/\Omega_p]}, \\ g &= \frac{\pi e^2}{\hbar s \Omega_p}, \quad g_0 = g \int_0^{\infty} \frac{dq s \Omega_p}{2\pi^3 \omega_{\mathbf{q}}(q_{\parallel}^2 + \hat{q}_{\perp}^2)}, \end{aligned} \quad (4)$$

where $\xi_p = p^2/2 - \varepsilon_F$, and F is a slowly varying function equal to 1 at $\varepsilon \ll \xi \kappa s$ and to $1/2$ at $\varepsilon \gg \xi \kappa s$. Formally, the integral for g_0 diverges logarithmically at large q_{\parallel} but becomes finite if it is considered that the integration over q_{\parallel} is restricted by the Brillouin zone or if the exact form of the dependence $\omega_{\mathbf{q}}$ at $q_{\parallel} \sim \kappa$ is taken into account. As a result, we obtain $g_0 \sim g \ln s q_F$ or $g_0 \sim g \ln \kappa s$, respectively. The exact expression for g_0 is determined by the particular energy structure of the metal at large distances from the Fermi surface.

The spectral function of electrons $A = \text{Im}G/\pi$ consists of a quasiparticle peak, whose value decreases with decreasing density of charge carriers, and of an

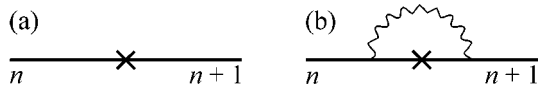


Fig. 1. Diagrams for the Green function nondiagonal with respect to the layer number that make the main contribution to the current in the transverse direction with respect to layers.

extended incoherent part. At $\varepsilon \ll \Omega_p$, with an accuracy to the terms linear in g ,

$$A = \frac{\delta(\varepsilon - \xi_p)}{1 + g_0} + \frac{gF}{\pi\Omega_p}. \quad (5)$$

Equation (5) is applicable to the superconducting state at $\varepsilon \gg \Delta(\kappa s)$. At lower energies, the second term in the spectral function becomes small, because it is determined by the plasmon poles of the potential and these poles are absent at energies lower than Δ . As a result, a dip appears in the spectral density at energies $\varepsilon < \Delta(\kappa s)$. This leads to the appearance of a peak–dip–hump structure in the superconducting state. This structure is similar to that observed in layered high- T_c superconductors in the direction $(0, \pi)$, corresponding to a maximum in the superconducting gap. However, our analysis, based on a simple model isotropic in the plane of layers, cannot pretend to be a quantitative description of the spectral density in a high- T_c superconductor.

Note that, though Eqs. (4) and (5) are formally applicable only at $T = 0$, a calculation at finite temperatures indicates that these equations can be used at a temperature much lower than the energies of plasmons, which give the main contribution to the integral in Eq. (4), that is, at $kT \ll \hbar v_F/s, \varepsilon_F, \Omega_p$.

Let us discuss now how the results will change on increasing the parameter g , determining the magnitude of interaction. In the general case, the Dyson equation must be solved for the renormalized Green function with regard to the vertex part. The diagrams entering into the vertex part, as well as the mass operator, contain large contributions associated with the plasmon poles of the renormalized interaction potential. However, an analysis shows that taking into account the vertex corrections does not change the results qualitatively. Therefore, expressions given by Eq. (4) can be used with an accuracy to constant factors if it is considered that the nonrenormalized plasma frequency enters into the formulas for g and g_0 , whereas the plasmon spectrum and frequency are renormalized, $\Omega_p \rightarrow \Omega_{p0}/(1 + g)$, $\omega_q \rightarrow \omega_{q0}/(1 + g)$, where the subscript 0 relates to the nonrenormalized frequencies.

To calculate the current at high voltages, we will use the Keldysh nonequilibrium diagram technique. The current density between the layers n and $n + 1$ can be

expressed through Green functions nondiagonal with respect to the layer number

$$j_{n, n+1} = \int \frac{2et_{\perp}}{\hbar} (G_{n, n+1}^{12} - G_{n+1, n}^{21}) \frac{d\varepsilon d\mathbf{p}_{\parallel}}{2\pi^3}, \quad (6)$$

where the superscripts relate to the time contour and the subscripts describe the layer number.

The diagrams for $G_{n, n+1}^{12}$ corresponding to the two basic mechanisms of the occurrence of a linear conductivity are presented in Fig. 1. The solid and wavy lines designate, correspondingly, the renormalized Green functions and the Coulomb potential, whereas a cross corresponds to t_{\perp} . These diagrams give strict results in the second order by the interaction and describe the current qualitatively at large g . The diagrams with a greater number of Coulomb lines either give small corrections by the parameter V/Ω_p or correspond to the renormalization of the vertex part, which does not result in a qualitative change of the results.

In the case of coherent tunneling, the process described by the diagram in Fig. 1a makes a contribution to the current in the normal state at the voltage drop across one layer $eV \gg \hbar/\tau$ (and in the superconducting state at $V \gg \Delta$) only as a result of renormalization, because renormalization gives the incoherent part of the spectral density. Assuming that $eV \gg \hbar\omega_p$ (but $eV \gg \hbar\Omega_p$), we obtain the linear volt–ampere characteristic with the conductivity

$$\sigma_1 = \frac{e^2 m s t_{\perp}^2}{\pi \hbar^4 \Omega_p} \frac{g}{(1 + g_0)^3} \left[1 + \frac{S_p}{2\pi p_F^2} \right], \quad (7)$$

where S_p is the area of the two-dimensional Brillouin zone of a metal layer. Comparing Eq. (7) with the standard equation for conductivity $\sigma = \omega_p^2 \tau / 4\pi$, we see that the role of the effective scattering time in σ_1 is played by $\pi \hbar [1 + S_p / (2\pi p_F^2)] / 8\varepsilon_F$. The diagram in Fig. 1a also makes a contribution to the conductivity of a superconductor with d pairing at $V < \Delta$ due to processes of the passage of quasiparticles through the superconducting gap [13], and $\pi \hbar / 16\Delta$, where Δ is the maximum gap, serves as the effective scattering time.

The diagram in Fig. 1b describes the contribution to the conductivity due to electron transitions with the emission or absorption of a plasmon. Its contribution to the current have an evident physical meaning

$$j = \int dk d\mathbf{p} d\mathbf{p}' e^{iks} \frac{4e^3 t_{\perp}^2 \omega_q}{\pi^3 \hat{q}_{\perp}^2 V^2} \times [n_p(1 - n_{p'}) (1 + N_q) - (1 - n_p) n_{p'} N_q] \times [\delta(\xi_p - \xi_{p'} + V + \omega_q) - \delta(\xi_p - \xi_{p'} - V + \omega_q)], \quad (8)$$

where n_p and N_q are the Fermi and Planck distributions of electrons and plasmons, respectively. Calculating

integrals at $eV \gg \hbar\omega_p$, Δ , we obtain the linear conductivity

$$\sigma_2 = \frac{e^2 p_F t_\perp^2}{3\pi^2 \hbar^4 \Omega_p^2 (1 + g_0)^3} g \quad (9)$$

Under our assumptions, the first contribution to the conductivity is greater than the second one, $\sigma_1/\sigma_2 \sim \kappa s$.

The expressions given by Eqs. (7) and (9) are also obtained for the real part of the conductivity at frequencies $\omega \gg \hbar\omega_p$, Δ , because the linear response is described by the same diagrams in which the voltage V is replaced by the frequency ω .

Let us discuss now the relation of the calculated results to experimental data, the most part of which were obtained with high- T_c superconductors. Our approach, based on taking into account the Coulomb effects and containing no assumptions on some special boson modes, describes qualitatively the appearance of a peak–dip–hump structure in the electron spectral density in such materials and suggests mechanisms of conductivity in the directions perpendicular to layers at high voltages or frequencies. However, the specific features of the electronic structure of high- T_c superconductors (such as the occurrence of almost flat regions of the Fermi surface in the $(0, \pi)$ directions, the van Hove singularities at the Fermi surface, and the angular dependence of t_\perp and Δ) are not taken into account in our simple model. Therefore, a quantitative description cannot be obtained without regard to the details of the electronic structure of particular layered metals.

The results calculated for the conductivity within the framework of our simple model do not contradict experimental data. The conductivity of $\text{Bi}_2\text{Sr}_2\text{CaCu}_2\text{O}_x$ measured at $V > \Delta$ is several times higher than the conductivity at small voltages $V < \Delta$ [1, 3, 4]. The conductivity calculated at high voltages contains the Fermi energy as the effective scattering frequency, and that calculated at low voltages contains the superconducting gap Δ as the effective scattering frequency. In the case of an isotropic transfer integral between layers t_\perp , this would mean that the conductivity at high voltages is lower than that at low voltages. However, if t_\perp is anisotropic and is determined by transitions through vertex oxygen atoms (see the review [14]), the ratio between the conductivities may become opposite, because the conductivity at low voltages is determined by quasiparticles near the sites of the superconducting gap. In this

case, the transfer integral is small, quasiparticles with arbitrary momentum directions make a contribution to the transitions between layers at $V > \Delta$, and the conductivity is determined by large values of t_\perp . Thus, the anisotropy of the electronic spectrum of the material must be taken into account in detail for a quantitative description.

The authors are grateful to K.É. Nagaev and A.G. Kobel'kov for useful discussions. This work was supported by the Russian Foundation for Basic Research, project no. 01-02-17527, and by the Russian State Program on Superconductivity, project no. 96053.

REFERENCES

1. Yu. I. Latyshev, T. Yamashita, L. N. Bulaevskii, *et al.*, Phys. Rev. Lett. **82**, 5345 (1999).
2. M. Suzuki, T. Watanabe, and A. Matsuda, Phys. Rev. Lett. **82**, 5361 (1999).
3. V. M. Krasnov, A. Yurgens, D. Winkler, *et al.*, Phys. Rev. Lett. **84**, 5860 (2000).
4. R. Kleiner and P. Müller, Phys. Rev. B **57**, 14518 (1998).
5. S. Tajima, J. Schützmann, S. Miyamoto, *et al.*, Phys. Rev. B **55**, 6051 (1997).
6. B. Ruzicka, L. Degiorgi, H. Berger, *et al.*, Phys. Rev. Lett. **86**, 4136 (2001).
7. D. S. Dessau, B. O. Wells, Z.-X. Shen, *et al.*, Phys. Rev. Lett. **71**, 2781 (1993).
8. Qiang Huang, J. E. Zasadinski, K. E. Gray, *et al.*, Phys. Rev. B **40**, 9366 (1989).
9. L. B. Ioffe and A. J. Millis, Phys. Rev. B **61**, 9077 (2000).
10. M. R. Norman and H. Ding, Phys. Rev. B **57**, R11089 (1998); M. Eschrig and M. R. Norman, Phys. Rev. Lett. **85**, 3261 (2000).
11. T. Mishonov, Phys. Rev. B **44**, 12033 (1991); **50**, 4004 (1994); S. N. Artemenko and A. G. Kobel'kov, Pis'ma Zh. Éksp. Teor. Fiz. **58**, 435 (1993) [JETP Lett. **58**, 445 (1993)]; M. Tachiki, S. Koyama, and M. Takahashi, Phys. Rev. B **50**, 7065 (1994).
12. Ophelia K. C. Tsui, N. P. Ong, Y. Matsuda, *et al.*, Phys. Rev. Lett. **73**, 724 (1994); Y. Matsuda, M. B. Gaifullin, K. Kumagai, *et al.*, Phys. Rev. Lett. **75**, 4512 (1995).
13. S. N. Artemenko, Pis'ma Zh. Éksp. Teor. Fiz. **70**, 516 (1999) [JETP Lett. **70**, 526 (1999)].
14. O. K. Andersen, A. I. Liechtenstein, O. Jepsen, *et al.*, J. Phys. Chem. Solids **56**, 1573 (1995).

Translated by A. Bagatur'yants

Theory of High- T_c Superconductivity Based on the Fermion-Condensation Quantum Phase Transition¹

M. Ya. Amusia^{1,2}, S. A. Artamonov³, and V. R. Shaginyan^{3*}

¹The Racah Institute of Physics, the Hebrew University, Jerusalem 91904, Israel

²Ioffe Physicotechnical Institute, Russian Academy of Sciences, Politekhnikeskaya ul. 26, St. Petersburg, 194021 Russia

³Institute of Nuclear Physics, Russian Academy of Sciences, Gatchina, Leningradskaya oblast, 188350 Russia

*e-mail: vrshag@thd.pnpi.spb.ru

Received September 3, 2001

A theory of high-temperature superconductivity based on the combination of the fermion-condensation quantum phase transition and the conventional theory of superconductivity is presented. This theory describes maximum values of the superconducting gap, which can be as big as $\Delta_1 \sim 0.1\epsilon_F$, with ϵ_F being the Fermi level. We show that the critical temperature $2T_c \approx \Delta_1$. If the pseudogap exists above T_c , then $2T^* \approx \Delta_1$ and T^* is the temperature at which the pseudogap vanishes. A discontinuity in the specific heat at T_c is calculated. The transition from conventional superconductors to high- T_c ones as a function of the doping level is investigated. The single-particle excitations and their lineshape are also considered © 2001 MAIK “Nauka/Interperiodica”.

PACS numbers: 74.20.Fg; 71.27.+a; 74.25.Jb

The explanation of the large values of critical temperature T_c , of the maximum value of the superconducting gap Δ_1 , and of the relation between Δ_1 and the temperature T^* at which the pseudogap vanishes are, as years before, among the main problems in the physics of high-temperature superconductivity. To solve them, one needs to know the single-particle spectra of corresponding metals. Recent studies of photoemission spectra discovered an energy scale in the spectrum of low-energy electrons in copper oxides, which manifests itself as a kink in the single-particle spectra [1–4]. As a result, the spectra in the energy range (–200–0) meV can be described by two straight lines intersecting at the binding energy $E_0 \sim (50–70)$ meV [2, 3]. The existence of the energy scale E_0 could be attributed to the interaction between electrons and the collective excitations, for instance, phonons [4]. On the other hand, the analysis of the experimental data on the single-particle electron spectra demonstrates that the perturbation of the spectra by phonons or other collective states is, in fact, very small; therefore, the corresponding state of electrons has to be described as a strongly collectivized quantum state and is named “quantum protectorate” [5, 6]. Thus, the interpretation of the above-mentioned kink as a consequence of electron–phonon interaction may very likely be in contradiction with the quantum protectorate concept. To describe the single-particle spectra and the kink, the assumption may be used that the electron system of a high- T_c superconductor has undergone the fermion-condensation quantum phase transition (FCQPT). This transition serves as a bound-

ary separating the normal Fermi liquid from the strongly correlated liquid of a new type [7, 8] and fulfills the quantum protectorate requirements [9]. The FCQPT appears in many-electron systems at relatively low density, where the effective interaction constant becomes sufficiently large. In ordinary electron liquid, this constant is directly proportional to the dimensionless parameter $r_s \sim 1/p_F a_B$, where a_B is the Bohr radius and p_F is the Fermi momentum. The FCQPT appears at a certain value r_s , $r_s = r_{FC}$, and precedes formation of charge-density waves or stripes [10], which are observed in underdoped samples of copper oxides [11]. This is why the formation of the FCQPT in copper oxides may be considered as a quite determinate process stemming from general properties of a low-density electron liquid [9].

In this paper, we address the above-mentioned problems in the physics of high-temperature superconductivity and demonstrate that these problems can be resolved in a theory based on the combination of the FCQPT and the conventional theory of superconductivity. We show that the FCQPT manifests itself in large values of Δ_1 , T_c , and T^* . We also trace the transition from conventional superconductors to high- T_c ones as a function of the parameter r_s , or as a function of the doping level.

At $T = 0$, the ground-state energy $E_{gs}[\kappa(\mathbf{p}), n(\mathbf{p})]$ of a two-dimensional electron liquid is a functional of the order parameter of the superconducting state $\kappa(\mathbf{p})$ and of the occupation numbers $n(\mathbf{p})$ and is determined by

¹ This article was submitted by the authors in English.

the known equation of the weak-coupling theory of superconductivity

$$E_{gs} = E[n(\mathbf{p})] + \int \lambda_0 V(\mathbf{p}_1, \mathbf{p}_2) \kappa(\mathbf{p}_1) \kappa^*(\mathbf{p}_2) \frac{d\mathbf{p}_1 d\mathbf{p}_2}{(2\pi)^4}. \quad (1)$$

Here, $E[n(\mathbf{p})]$ is the ground-state energy of a normal Fermi liquid, $n(\mathbf{p}) = v^2(\mathbf{p})$, and $\kappa(\mathbf{p}) = v(\mathbf{p})\sqrt{1 - v^2(\mathbf{p})}$. It is assumed that the pairing interaction $\lambda_0 V(\mathbf{p}_1, \mathbf{p}_2)$ is weak. Minimizing E_{gs} with respect to $\kappa(\mathbf{p})$, we obtain the equation connecting the single-particle energy $\varepsilon(\mathbf{p})$ to $\Delta(\mathbf{p})$,

$$\varepsilon(\mathbf{p}) - \mu = \Delta(\mathbf{p}) \frac{1 - 2v^2(\mathbf{p})}{2\kappa(\mathbf{p})}. \quad (2)$$

The single-particle energy $\varepsilon(\mathbf{p})$ is determined by the Landau equation, $\varepsilon(\mathbf{p}) = \delta E[n(\mathbf{p})]/\delta n(\mathbf{p})$ [12], and μ is the chemical potential. The equation for the superconducting gap $\Delta(\mathbf{p})$ takes the form

$$\begin{aligned} \Delta(\mathbf{p}) &= -\int \lambda_0 V(\mathbf{p}, \mathbf{p}_1) \kappa(\mathbf{p}_1) \frac{d\mathbf{p}_1}{4\pi^2} \\ &= -\frac{1}{2} \int \lambda_0 V(\mathbf{p}, \mathbf{p}_1) \frac{\Delta(\mathbf{p}_1)}{\sqrt{(\varepsilon(\mathbf{p}_1) - \mu)^2 + \Delta^2(\mathbf{p}_1)}} \frac{d\mathbf{p}_1}{4\pi^2}. \end{aligned} \quad (3)$$

If $\lambda_0 \rightarrow 0$, then the gap $\Delta(\mathbf{p}) \rightarrow 0$, and Eq. (2) reduces to the equation proposed in [7]

$$\varepsilon(\mathbf{p}) - \mu = 0, \text{ if } 0 < n(\mathbf{p}) < 1; \quad p_i \leq p \leq p_f. \quad (4)$$

At $T = 0$, Eq. (4) defines a particular state of Fermi liquid with the fermion condensate (FC), for which the modulus of the order parameter $|\kappa(\mathbf{p})|$ has finite values in the L_{FC} range of momenta $p_i \leq p \leq p_f$, and $\Delta_1 \rightarrow 0$ in the L_{FC} . Such a state can be considered as superconducting with an infinitely small value of Δ_1 , so that the entropy of this state is equal to zero. It is obvious that this state, being driven by the quantum phase transition, disappears at $T > 0$ [9]. When $p_i \rightarrow p_F \rightarrow p_f$, Eq. (4) determines the point r_{FC} at which the FCQPT takes place. It follows from Eq. (4) that the system breaks into two quasiparticle subsystems: the first subsystem in the L_{FC} range is occupied by the quasiparticles with the effective mass $M_{FC}^* \rightarrow \infty$, while the second one is occupied by quasiparticles with finite mass M_L^* and momenta $p < p_i$. If $\lambda_0 \neq 0$, Δ_1 becomes finite, leading to a finite value of the effective mass M_{FC}^* in L_{FC} , which can be obtained from Eq. (2) [9]

$$M_{FC}^* \approx p_F \frac{p_f - p_i}{2\Delta_1}. \quad (5)$$

As to the energy scale, it is determined by the parameter E_0 :

$$E_0 = \varepsilon(\mathbf{p}_f) - \varepsilon(\mathbf{p}_i) \approx 2 \frac{(p_f - p_F) p_F}{M_{FC}^*} \approx 2\Delta_1. \quad (6)$$

Thus, a system with FC has a single-particle spectrum of the universal form and possesses quantum protectorate features at $T \ll T_f$, with T_f being a temperature at which the effect of the FCQPT disappears.

We assume that the range L_{FC} is small, $(p_f - p_F)/p_F \ll 1$, and $2\Delta_1 \ll T_f$, so that the order parameter $\kappa(\mathbf{p})$ is governed mainly by the FC [9]. To solve Eq. (2) analytically, we take the Bardeen–Cooper–Schrieffer (BCS) approximation for the interaction [13]: $\lambda_0 V(\mathbf{p}, \mathbf{p}_1) = -\lambda_0$ if $|\varepsilon(\mathbf{p}) - \mu| \leq \omega_D$, and the interaction is zero outside this region, with ω_D being the characteristic phonon energy. As a result, the gap becomes dependent only on the temperature, $\Delta(\mathbf{p}) = \Delta_1(T)$, being independent of the momentum, and Eq. (2) takes the form

$$\begin{aligned} 1 &= N_{FC} \lambda_0 \int_0^{E_0/2} \frac{d\xi}{\sqrt{\xi^2 + \Delta_1(0)^2}} \\ &+ N_L \lambda_0 \int_{E_0/2}^{\omega_D} \frac{d\xi}{\sqrt{\xi^2 + \Delta_1(0)^2}}. \end{aligned} \quad (7)$$

Here, we set $\xi = \varepsilon(\mathbf{p}) - \mu$ and introduce the density of states N_{FC} in the L_{FC} or E_0 range. As follows from Eq. (5), $N_{FC} = (p_f - p_F) p_F / 2\pi \Delta_1(0)$. The density of states N_L in the range $(\omega_D - E_0/2)$ has the standard form $N_L = M_L^* / 2\pi$. If the energy scale $E_0 \rightarrow 0$, Eq. (7) is reduced to the BCS equation. On the other hand, assuming that $E_0 \leq 2\omega_D$ and omitting the second integral in the right-hand side of Eq. (7), we obtain

$$\begin{aligned} \Delta_1(0) &= \frac{\lambda_0 p_F (p_f - p_F)}{2\pi} \ln(1 + \sqrt{2}) \\ &= 2\beta \varepsilon_F \frac{p_f - p_F}{p_F} \ln(1 + \sqrt{2}), \end{aligned} \quad (8)$$

where the Fermi energy $\varepsilon_F = p_F^2 / 2M_L^*$, and dimensionless coupling constant $\beta = \lambda_0 M_L^* / 2\pi$. Taking the usual values of the dimensionless coupling constant $\beta \approx 0.3$, and $(p_f - p_F)/p_F \approx 0.2$, we get from Eq. (7) the large value of $\Delta_1(0) \sim 0.1\varepsilon_F$, while for normal metals one has $\Delta_1(0) \sim 10^{-3}\varepsilon_F$. Taking into account the omitted integral, we obtain

$$\Delta_1(0) \approx 2\beta \varepsilon_F \frac{p_f - p_F}{p_F} \ln(1 + \sqrt{2}) \left(1 + \beta \ln \frac{2\omega_D}{E_0}\right). \quad (9)$$

It is seen from Eq. (9) that the correction due to the second integral is small, provided $E_0 \approx 2\omega_D$. Below, we show that $2T_c \approx \Delta_1(0)$, which leads to the conclusion

that there is no isotope effect, since Δ_1 is independent of ω_D . But this effect is restored as $E_0 \rightarrow 0$. Assuming $E_0 \sim \omega_D$ and $E_0 > \omega_D$, we see that Eq. (7) has no standard solutions $\Delta(p) = \Delta_1(0)$ because $\omega_D < \varepsilon(p \approx p_f) - \mu$ and the interaction vanishes at these momenta. The only way to obtain solutions is to restore the condition $E_0 < \omega_D$. For instance, we can define the momentum $p_D < p_f$ such that

$$\Delta_1(0) = 2\beta\varepsilon_F \frac{p_D - p_F}{p_F} \ln(1 + \sqrt{2}) = \omega_D, \quad (10)$$

while the other part in the L_{FC} range can be occupied by a gap Δ_2 of the different sign, $\Delta_1(0)/\Delta_2 < 0$. It follows from Eq. (10) that the isotope effect is presented. A more detailed analysis will be published elsewhere.

At $T \rightarrow T_c$, Eqs. (5) and (6) are replaced by the equation, which is valid also at $T_c \leq T \ll T_f$ [9]

$$M_{FC}^* \approx p_F \frac{p_f - p_i}{4T_c}, \quad E_0 \approx 4T_c; \quad (11)$$

$$\text{if } T_c \leq T: M_{FC}^* \approx p_F \frac{p_f - p_i}{4T}, \quad E_0 \approx 4T.$$

Equation (7) is replaced by its conventional finite-temperature generalization

$$1 = N_{FC}\lambda_0 \int_0^{E_0/2} \frac{d\xi}{\sqrt{\xi^2 + \Delta_1(T)^2}} \tanh \frac{\sqrt{\xi^2 + \Delta_1(T)^2}}{2T} + N_L\lambda_0 \int_{E_0/2}^{\omega_D} \frac{d\xi}{\sqrt{\xi^2 + \Delta_1(T)^2}} \tanh \frac{\sqrt{\xi^2 + \Delta_1(T)^2}}{2T}. \quad (12)$$

Putting $\Delta_1(T \rightarrow T_c) \rightarrow 0$, we obtain from Eq. (12)

$$2T_c \approx \Delta_1(0), \quad (13)$$

with $\Delta_1(0)$ being given by Eq. (9). By comparing Eqs. (5), (11), and (13), we see that M_{FC}^* and E_0 are almost temperature-independent at $T \leq T_c$. Now a few remarks are in order. One can define T_c as the temperature where $\Delta_1(T_c) \equiv 0$. At $T \geq T_c$, Eq. (12) has only the trivial solution $\Delta_1 \equiv 0$. On the other hand, T_c can be defined as a temperature at which the superconductivity vanishes. Thus, we deal with two different definitions, which can lead to different temperatures. It was shown [14, 15] that in the case of the d -wave superconductivity, taking place in the presence of the FC, there exist nontrivial solutions of Eq. (12) at $T_c \leq T \leq T^*$ corresponding to the pseudogap state. It happens when the gap occupies only that part of the Fermi surface which shrinks as the temperature increases. Here, T^* defines the temperature at which $\Delta_1(T^*) \equiv 0$ and the pseudogap state vanishes. The superconductivity is destroyed at T_c , and the ratio $2\Delta_1/T_c$ can vary in a wide range and strongly depends upon the material properties, as follows from the con-

sideration given in [14, 15]. Therefore, provided the pseudogap exists above T_c , then T_c is to be replaced by T^* , and Eq. (13) takes the form

$$2T^* \approx \Delta_1(0). \quad (14)$$

The ratio $2\Delta_1/T_c$ can reach very high values. For instance, in the case of $\text{Bi}_2\text{Sr}_2\text{CaCu}_2\text{Q}_{6+\delta}$, where the superconductivity and the pseudogap are considered to be of common origin, $2\Delta_1/T_c \approx 4$ is about 28, while the ratio $\Delta_1/T^* \approx 4$, which is also valid for various cuprates [16]. Thus, Eq. (14) gives a good description of the experimental data. We remark that Eq. (7) also gives a good description of the maximum gap Δ_1 in the case of the d -wave superconductivity [14, 15], because the different regions with the maximum absolute value of Δ_1 and the maximal density of states can be considered as disconnected [17]. Therefore, the gap in this region is formed by attractive phonon interaction, which is approximately independent of the momenta. According to the model proposed in [9], the doping level x is related to the parameter r_s in the following way: $(x_{FC} - x) \sim (r_s - r_{FC}) \sim (p_f - p_i)/p_F$. The value x_{FC} matches r_{FC} when defining the point at which the FCQPT takes place. We assume that the dopant concentration x_{FC} corresponds to the highly overdoped regime at which slight deviations from the normal Fermi liquid are observed [18]. Then, from Eqs. (8) and (9) it follows that Δ_1 is directly proportional to $(x_{FC} - x)$. From Eq. (14) one finds that the function $T^*(x)$ represents a straight line crossing the abscissa at the point $x_{FC} \approx x$, while, in the vicinity of this point, T^* merges with T_c and both of them tends to zero.

Now we turn to the calculations of the gap and the specific heat at the temperatures $T \rightarrow T_c$. It is worth noting that this consideration is valid, provided $T^* = T_c$, otherwise the discontinuity considered below is smoothed out over the temperature range $T^* - T_c$. For the sake of simplicity, we calculate the main contribution to the gap and the specific heat coming from the FC. The function $\Delta_1(T \rightarrow T_c)$ is found from Eq. (12) upon expanding the right-hand side of the first integral in powers of Δ_1 and omitting the contribution from the second integral on the right-hand side of Eq. (12). This procedure leads to the following equation:

$$\Delta_1(T) \approx 3.4T_c \sqrt{1 - T/T_c}. \quad (15)$$

Thus, the gap in the spectrum of the single-particle excitations has quite usual behavior. To calculate the specific heat, the conventional expression for the entropy S [13] can be used

$$S = 2 \int [f(\mathbf{p}) \ln f(\mathbf{p}) + (1 - f(\mathbf{p})) \ln(1 - f(\mathbf{p}))] \frac{d\mathbf{p}}{(2\pi)^2}, \quad (16)$$

$$f(\mathbf{p}) = \frac{1}{1 + \exp[E(\mathbf{p})/T]}; \quad (17)$$

$$E(\mathbf{p}) = \sqrt{(\varepsilon(\mathbf{p}) - \mu)^2 + \Delta_1^2(T)}.$$

The specific heat C is determined by

$$C = T \frac{dS}{dT} \approx 4 \frac{N_{FC}}{T^2} \int_0^{E_0} f(E)(1 - f(E)) \times \left[E^2 + T\Delta_1(T) \frac{d\Delta_1(T)}{dT} \right] d\xi + 4 \frac{N_L}{T^2} \quad (18)$$

$$\times \int_{E_0}^{\omega_D} f(E)(1 - f(E)) \left[E^2 + T\Delta_1(T) \frac{d\Delta_1(T)}{dT} \right] d\xi.$$

When deriving Eq. (18), we again use the variable N_{FC} and the densities of states N_{FC}, N_L , just as before in connection to Eq. (7), as well as the notation $E = \sqrt{\xi^2 + \Delta_1^2(T)}$. Equation (18) predicts the conventional discontinuity δC in the specific heat C at T_c because of the last term in the square brackets of Eq. (18). Upon using Eq. (15) to calculate this term and omitting the second integral on the right-hand side of Eq. (18), we obtain

$$\delta C \approx \frac{3}{2\pi} (p_f - p_i) p_F. \quad (19)$$

In contrast to the conventional result when the discontinuity is a linear function of T_c , δC is independent of the critical temperature T_c because the density of state varies inversely with T_c , as follows from Eq. (11). Note that, deriving Eq. (19), we take into account the main contribution coming from the FC. This contribution vanishes as soon as $E_0 \rightarrow 0$, and the second integral in Eq. (18) gives the conventional result.

Consider the lineshape $L(q, \omega)$ of the single-particle spectrum which is a function of two variables. Measurements carried out at a fixed binding energy $\omega = \omega_0$, where ω_0 is the energy of a single-particle excitation, determine the lineshape $L(q, \omega = \omega_0)$ as a function of the momentum q . We have shown above that M_{FC}^* is finite and constant at $T \leq T_c$. Therefore, at excitation energies $\omega \leq E_0$ the system behaves like an ordinary superconducting Fermi liquid with the effective mass given by Eq. (5) [9]. At $T_c \leq T$, the low-energy effective mass M_{FC}^* is finite and is given by Eq. (11). Once again, at the energies $\omega \leq E_0$, the system behaves as a Fermi liquid, the single-particle spectrum is well defined, while the width of single-particle excitations is on the order of T [9, 19]. This behavior was observed in experiments on measuring the lineshape at a fixed energy [1]. It is pertinent to note that recent measurements of the lineshape suggest that quasiparticle exci-

tation even in the $(\pi, 0)$ region of the Brillouin zone of $\text{Bi}_2\text{Sr}_2\text{CaCu}_2\text{Q}_{8+\delta}$ (Bi2212) are much better defined than was previously believed from earlier Bi2212 data [20]. The lineshape can also be determined as a function $L(q = q_0, \omega)$ at a fixed $q = q_0$. At small ω , the lineshape resembles the one considered above, and $L(q = q_0, \omega)$ has a characteristic maximum and width. At energies $\omega \geq E_0$, quasiparticles with the mass M_L^* come into play, leading to a growth of the function $L(q = q_0, \omega)$. As a result, the function $L(q = q_0, \omega)$ possesses the known peak-dip-hump structure [21] directly defined by the existence of the two effective masses M_{FC}^* and M_L^* [9]. To have a more quantitative and analytical insight into the problem, we use the Kramers–Krönig relation to construct the imaginary part $\text{Im}\Sigma(\mathbf{p}, \varepsilon)$ of the self-energy $\Sigma(\mathbf{p}, \varepsilon)$, starting with the real one $\text{Re}\Sigma(\mathbf{p}, \varepsilon)$ which defines the effective mass [22]

$$\frac{1}{M^*} = \left(\frac{1}{M} + \frac{1}{p_F} \frac{\partial \text{Re}\Sigma}{\partial p} \right) \left(1 - \frac{\partial \text{Re}\Sigma}{\partial \varepsilon} \right). \quad (20)$$

Here, M is the bare mass, while the relevant momenta p and energies ε are subjected to the following conditions: $|p - p_F|/p_F \ll 1$, and $\varepsilon/\varepsilon_F \ll 1$. We take $\text{Re}\Sigma(\mathbf{p}, \varepsilon)$ in the simplest form which accounts for the change of the effective mass at the energy scale E_0 :

$$\text{Re}\Sigma(\mathbf{p}, \varepsilon) = -\varepsilon \frac{M_{FC}^*}{M} + \left(\varepsilon - \frac{E_0}{2} \right) \frac{M_{FC}^* - M_L^*}{M} \times [\theta(\varepsilon - E_0/2) + \theta(-\varepsilon - E_0/2)]. \quad (21)$$

Here, $\theta(\varepsilon)$ is the step function. Note that, in order to ensure a smooth transition from the single-particle spectrum characterized by M_{FC}^* to the spectrum defined by M_L^* , the step function is to be substituted by some smooth function. Upon inserting Eq. (21) into Eq. (20), we can check that inside the interval $(-E_0/2, E_0/2)$ the effective mass $M^* \approx M_{FC}^*$, and outside the interval $M^* \approx M_L^*$. By applying the Kramers–Krönig relation to $\text{Re}\Sigma(\mathbf{p}, \varepsilon)$, we obtain the imaginary part of the self-energy,

$$\text{Im}\Sigma(\mathbf{p}, \varepsilon) \sim \varepsilon^2 \frac{M_{FC}^*}{\varepsilon_F M} + \frac{M_{FC}^* - M_L^*}{M} \times \left(\varepsilon \ln \left| \frac{\varepsilon + E_0/2}{\varepsilon - E_0/2} \right| + \frac{E_0}{2} \ln \left| \frac{\varepsilon^2 - E_0^2/4}{E_0^2/4} \right| \right). \quad (22)$$

We can see from Eq. (22) that, at $\varepsilon/E_0 \ll 1$, the imaginary part is proportional to ε^2 ; at $2\varepsilon/E_0 = 1$, $\text{Im}\Sigma \sim \varepsilon$; at $E_0/\varepsilon \ll 1$, the main contribution to the imaginary part is approximately constant. This is the behavior that gives rise to the known peak-dip-hump structure. Then, it is seen from Eq. (22) that, when $E_0 \rightarrow 0$, the second

term on the right-hand side tends toward zero, the single-particle excitations become better defined, resembling that of a normal Fermi liquid, and the peak-dip-hump structure eventually vanishes. On the other hand, the quasiparticle amplitude $a(\mathbf{p})$ is given by [22]

$$\frac{1}{a(\mathbf{p})} = 1 - \frac{\partial \text{Re}\Sigma(\mathbf{p}, \varepsilon)}{\partial \varepsilon}. \quad (23)$$

It follows from Eq. (20) that the quasiparticle amplitude $a(\mathbf{p})$ rises as the effective mass M_{FC}^* decreases. Since $M_{FC}^* \sim (p_f - p_i) \sim (x_{FC} - x)$ [9], we are led to the conclusion that the amplitude $a(\mathbf{p})$ rises as the doping level rises, and the single-particle excitations become better defined in highly overdoped samples. It is worth noting that such behavior was observed experimentally Bi2212 so highly overdoped that the gap size was about 10 meV [18]. Such a small size of the gap indicates that the region occupied by the FC is small, since $E_0/2 \approx \Delta_1$.

In conclusion, we have shown that the theory of high-temperature superconductivity based on the fermion-condensation quantum phase transition and on the conventional theory of superconductivity permits one to describe high values of T_c , T^* , and the maximum value of the gap, which may be as large as $\Delta_1 \sim 0.1\varepsilon_F$. We have also traced the transition from conventional superconductors to high- T_c ones and demonstrated that, in highly overdoped cuprates, single-particle excitations become much better defined, resembling those of a normal Fermi liquid.

This work was supported in part by the Russian Foundation for Basic Research, project no. 01-02-17189.

REFERENCES

1. T. Valla *et al.*, *Science* **285**, 2110 (1999); T. Valla *et al.*, *Phys. Rev. Lett.* **85**, 828 (2000).
2. P. V. Bogdanov *et al.*, *Phys. Rev. Lett.* **85**, 2581 (2000).
3. A. Kaminski *et al.*, *Phys. Rev. Lett.* **86**, 1070 (2001).
4. A. Lanzara *et al.*, *Nature* **412**, 510 (2001).
5. R. B. Laughlin and D. Pines, *Proc. Natl. Acad. Sci. USA* **97**, 28 (2000).
6. P. W. Anderson, cond-mat/0007185; cond-mat/0007287.
7. V. A. Khodel and V. R. Shaginyan, *Pis'ma Zh. Éksp. Teor. Fiz.* **51**, 488 (1990) [*JETP Lett.* **51**, 553 (1990)].
8. G. E. Volovik, *Pis'ma Zh. Éksp. Teor. Fiz.* **53**, 208 (1991) [*JETP Lett.* **53**, 222 (1991)].
9. M. Ya. Amusia and V. R. Shaginyan, *Pis'ma Zh. Éksp. Teor. Fiz.* **73**, 268 (2001) [*JETP Lett.* **73**, 232 (2001)]; *Phys. Rev. B* **63**, 224507 (2001).
10. V. A. Khodel, V. R. Shaginyan, and M. V. Zverev, *Pis'ma Zh. Éksp. Teor. Fiz.* **65**, 242 (1997) [*JETP Lett.* **65**, 253 (1997)].
11. G. Grüner, *Density Waves in Solids* (Addison-Wesley, Reading, 1994).
12. L. D. Landau, *Zh. Éksp. Teor. Fiz.* **30**, 1058 (1956) [*Sov. Phys. JETP* **3**, 920 (1956)].
13. J. Bardeen, L. N. Cooper, and J. R. Schrieffer, *Phys. Rev.* **108**, 1175 (1957).
14. V. R. Shaginyan, *Pis'ma Zh. Éksp. Teor. Fiz.* **68**, 491 (1998) [*JETP Lett.* **68**, 527 (1998)].
15. S. A. Artamonov and V. R. Shaginyan, *Zh. Éksp. Teor. Fiz.* **119**, 331 (2001) [*JETP* **92**, 287 (2001)].
16. M. Kugler *et al.*, *Phys. Rev. Lett.* **86**, 4911 (2001).
17. A. A. Abrikosov, *Phys. Rev. B* **52**, R15738 (1995); A. A. Abrikosov, cond-mat/9912394.
18. Z. Yusof *et al.*, cond-mat/01044367.
19. J. Dukelsky *et al.*, *Z. Phys.* **102**, 245 (1997).
20. D. L. Feng *et al.*, cond-mat/0107073.
21. D. S. Dessau *et al.*, *Phys. Rev. Lett.* **66**, 2160 (1991).
22. A. B. Migdal, *Theory of Finite Fermi Systems and Applications to Atomic Nuclei* (Nauka, Moscow, 1982, 2nd ed.; Interscience, New York, 1967).

Synthesis of a New Magnetic $Y_2Mn_{2/3}Re_{4/3}O_7$ with Pyrochlore-like Structure

G. V. Bazuev*, T. I. Chupakhina, and V. N. Krasil'nikov

*Institute of Solid-State Chemistry, Ural Division, Russian Academy of Sciences,
ul. Pervomaïskaya 91, Yekaterinburg, 620219 Russia*

* e-mail: bazuev@ihim.uran.ru

Received September 3, 2001

A complex oxide of the $Y_2Mn_{2/3}Re_{4/3}O_7$ composition with pyrochlore-like structure and parameters of hexagonal unit cell $a = 14.91(1) \text{ \AA}$, $c = 17.53(1) \text{ \AA}$ was synthesized. The magnetic susceptibility and magnetization measurements showed that below 190 K this oxide possesses spontaneous magnetic moment. In the paramagnetic region, the magnetic susceptibility obeys the Curie–Weiss law $\chi = C/(T - \Theta)$, with $C = 2.07 \text{ cm}^3 \text{ K mol}^{-1}$ and $\Theta = -160 \text{ K}$, and the effective magnetic moment corresponding to the cationic combination $Mn^{2+} - Re^{5+}$. The data obtained allow one to assume that the compound has a noncollinear antiferromagnetic structure. © 2001 MAIK “Nauka/Interperiodica”.

PACS numbers: 75.20.Hr; 75.30.Cr; 75.50.-y

Magnetic properties of complex oxides with a pyrochlore structure have attracted serious attention after the discovery of ferromagnetism in rare-earth hypovanadates $Ln_2V_2O_7$ ($Ln = Lu, Yb$, and Tm ; $T_C = 73.5 \text{ K}$) [1, 2]. A search for pyrochlore-like oxides have culminated, in particular, in the synthesis of thallium manganate $Tl_2Mn_2O_7$ ($T_C = 121 \text{ K}$) [3], which was found to display colossal magnetoresistance [4]. Recently [5], “unprecedented” magnetoresistance (higher than for the stoichiometric $Tl_2Mn_2O_7$) was observed in a $Tl_{2-x}Cd_xMn_2O_7$ solid solution. These oxides have a face-centered cubic lattice belonging to the space group $Fd\bar{3}m$ and they are isostructural with the pyrochlore mineral $NaCaTa_2O_6(OH; F)$ [6].

In a number of works [7, 8 and references therein], oxides of a more complex composition ($Ln_2B'_{2/3}B''_{4/3}O_7$) were synthesized, in which the B' and B'' sites are occupied by two different d elements. Contrary to the “simple” pyrochlores, the structure of more complex oxides is not cubic and belongs to the rhombohedral or monoclinic [9] crystal system. A detailed analysis of the crystal structures of these compounds has not been carried out so far. In [9], the X-ray diffraction patterns of the compositionally close $Ho_2Mn_{0.6}Nb_{1.4}O_{7.1}$ oxide were indexed on the basis of the zirconolite structure $CaZrTi_2O_7$ [10]. In the structural model adopted for this oxide, three types of cationic positions occur for the Nb and Mn atoms.

The magnetic properties of these complex oxides also remain to be studied. Those compounds in which both B' and B'' sites are occupied by the cations whose d orbitals are only partly filled are of greatest interest. In [7, 8], the presence of ferrimagnetic properties of the

$Y_2Mn_{2/3}Mo_{4/3}O_7$ and $Y_2Fe_{2/3}Mo_{4/3}O_7$ compounds at low temperatures was suggested on the basis of magnetic susceptibility measurements carried out at $T \geq 77 \text{ K}$.

This paper reports on the synthesis of a new complex oxide $Y_2Mn_{2/3}Re_{4/3}O_7$, whose crystal structure is similar to the structure of previously synthesized $Ln_2B'_{2/3}B''_{4/3}O_7$ oxides. The compound was prepared in vacuum from Mn_2O_3 , ReO_2 , and Y_3ReO_8 oxides and metallic Re. The double oxide Y_3ReO_8 was obtained in air from yttrium oxide Y_2O_3 and ammonium perrhenate NH_4ReO_4 at 900°C . A mixture of the indicated components was carefully ground in the ratio 1 : 1 : 2 : 1 and pressed and placed into a quartz tube, which was then evacuated and sealed. Synthesis was carried out at a temperature of 1273 K with one-fold intermediate grinding, repeated pressing, and sealing in a quartz tube. The course of chemical reactions was monitored by X-ray diffraction.

The X-ray diffraction pattern of the prepared $Y_2Mn_{2/3}Re_{4/3}O_7$ sample is shown in Fig. 1 (DRON-2 diffractometer, CuK_α radiation, Ni filter). The array of reflections was indexed in the hexagonal (or rhombohedral) symmetry. The lattice parameters of $Y_2Mn_{2/3}Re_{4/3}O_7$ in the hexagonal basis are as follows: $a = 14.91(1) \text{ \AA}$, $c = 17.53(1) \text{ \AA}$, and $V = 3375 \text{ \AA}^3$. These values, especially the c parameter, are quite different from those previously found for the $Y_2Mn_{2/3}Mo_{4/3}O_7$ oxide: $a = 14.80(1) \text{ \AA}$, $c = 17.24(1) \text{ \AA}$, and $V = 3270 \text{ \AA}^3$. Since the ion radii of Mo^{5+} and Re^{5+} are close and equal, respectively, to 0.61 and 0.58 Å [9], this result calls for further analysis. The X-ray diffraction data did not reveal any impurities in the sample.

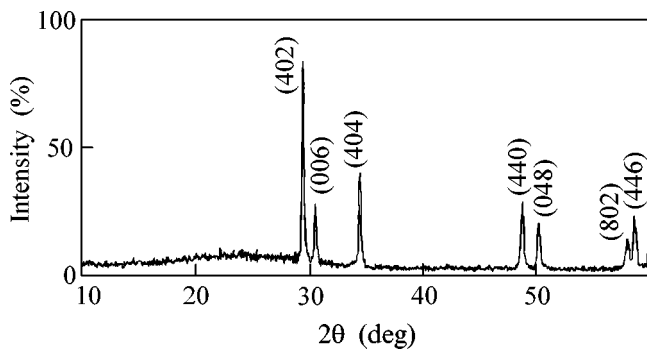


Fig. 1. X-ray diffraction pattern of $\text{Y}_2\text{Mn}_{2/3}\text{Re}_{4/3}\text{O}_7$

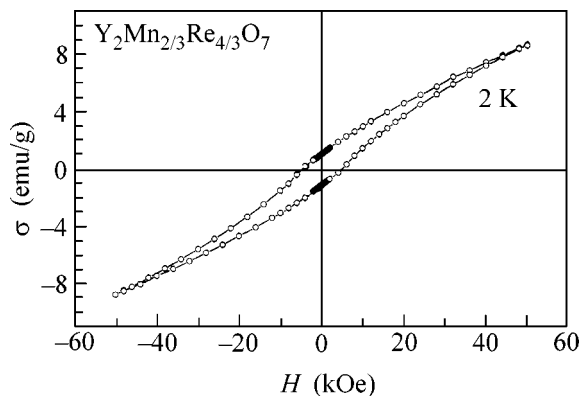


Fig. 3. Magnetic hysteresis curve (magnetization σ as a function of magnetic field H) of $\text{Y}_2\text{Mn}_{2/3}\text{Re}_{4/3}\text{O}_7$ at 2 K.

The magnetic properties of the prepared compound were studied on an MPMS SQUID magnetometer over the temperature range 2–400 K. Measurements were made in magnetic fields of 0.5 and 5 kOe upon cooling in zero and nonzero fields. The magnetization was measured in magnetic fields below 50 kOe at 2, 20, 130, 200, and 298 K after zero-field cooling. The sample was ceramics sintered under the above-mentioned conditions. The results of measurements are presented in Figs. 2–4.

It is seen from Fig. 2 that the temperature dependence of the susceptibility χ of $\text{Y}_2\text{Mn}_{2/3}\text{Re}_{4/3}\text{O}_7$ has well-defined anomalies in the range 2–300 K. Below 190 K, χ increases dramatically and displays different behavior below 125 K, depending on whether it was zero-field- or field-cooled. The $\chi = f(T)$ curve also has inflection at 7 K. At 2, 20, and 130 K, spontaneous magnetization was observed with the following magnetic moments: $0.03\mu_B$ at 130 K and $0.2\mu_B$ at 20 K. At 2 K, magnetic saturation was not achieved. The magnetic hysteresis curve at 2 K is shown in Fig. 3.

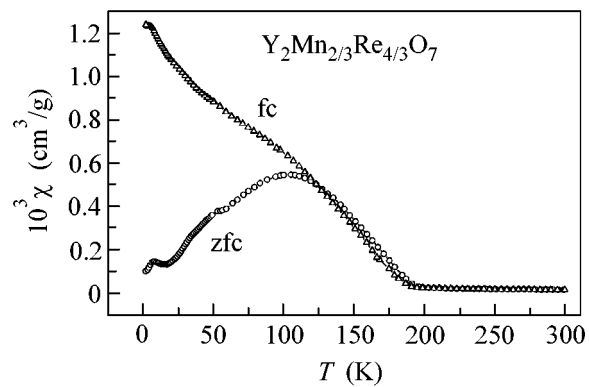


Fig. 2. Temperature dependences of magnetic susceptibility χ of $\text{Y}_2\text{Mn}_{2/3}\text{Re}_{4/3}\text{O}_7$ after (*fc*) field cooling (*fc*) and (*zfc*) zero-field cooling.

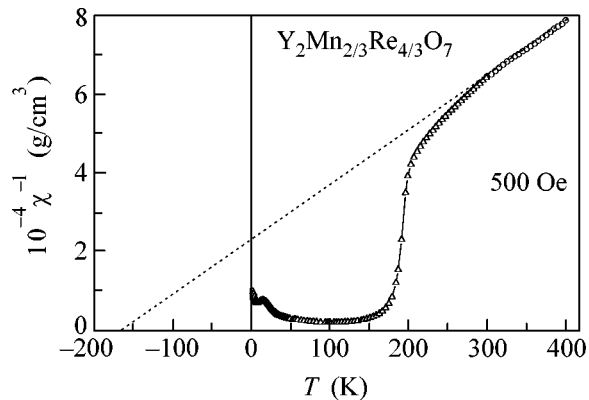


Fig. 4. Temperature dependence of inverse magnetic susceptibility $1/\chi$ of $\text{Y}_2\text{Mn}_{2/3}\text{Re}_{4/3}\text{O}_7$ in a magnetic field of 500 Oe.

The temperature dependence of the inverse magnetic susceptibility $1/\chi$ is shown in Fig. 4. One can see that χ obeys the Curie–Weiss law in the temperature range 300–400 K: $\chi = C/(T - \Theta)$. The Curie constant C and the Weiss constant Θ of this law are equal to $2.07 \text{ (cm}^2 \text{ K)/mol}$ and -160 K , respectively. The effective magnetic moment ($4.07\mu_B$) per one averaged paramagnetic center of the formula $\text{Y}_2\text{Mn}_{1/3}\text{Re}_{2/3}\text{O}_{3.5}$ is close to that calculated for the cationic combination $\text{Mn}^{2+}\text{Re}^{5+}$ ($4.13\mu_B$). This fact counts in favor of the presence of the Mn^{2+} (outer electronic configuration d^5) and Re^{5+} (d^2) cations in the compound.

The negative value of Θ is evidence of the antiferromagnetic interaction between the Mn and Re cations at low temperatures. It is notable that the absolute value of Θ (160 K) is close to the magnetic transition temperature (190 K). The experimental results, in particular, the small spontaneous magnetic moments, in conjunction with the negative value of Θ , allow one to assume that the magnetic structure of this oxide is noncollinear.

More detailed insight into the nature of exchange magnetic interaction in $Y_2Mn_{2/3}Re_{4/3}O_7$ and its magnetic structure calls for further, especially neutron diffraction, studies.

We are grateful to Prof. G.V. Subba Rao, India, for discussions.

REFERENCES

1. G. V. Bazuev, O. V. Makarova, V. Z. Oboldin, and G. P. Shveikin, Dokl. Akad. Nauk SSSR **230**, 869 (1976).
2. G. V. Bazuev, A. A. Samokhvalov, Yu. N. Morozov, *et al.*, Fiz. Tverd. Tela (Leningrad) **19**, 3274 (1977) [Sov. Phys. Solid State **19**, 1913 (1977)].
3. H. Fujinaka, N. Kinomura, M. Koizumi, *et al.*, Mater. Res. Bull. **14**, 1133 (1979).
4. M. A. Subramanian, B. H. Toby, A. P. Ramirez, *et al.*, Science **273** (5271), 81 (1996).
5. J. A. Alonso, P. Velasco, M. J. Martinez-Lope, *et al.*, Appl. Phys. Lett. **76**, 3274 (2000).
6. A. S. Povarennykh, *Crystal Chemical Classification of Mineral Kinds* (Naukova Dumka, Kiev, 1966).
7. G. V. Bazuev, O. V. Makarova, and G. P. Shveikin, Zh. Neorg. Khim. **29**, 875 (1984).
8. G. V. Bazuev, O. V. Makarova, and N. A. Kirsanov, Zh. Neorg. Khim. **34**, 23 (1989).
9. H. Nakano, A. Kishigami, M. Hisa, and N. Kamegashira, Mater. Res. Bull. **34**, 2075 (1999).
10. R. D. Shannon, Acta Crystallogr. A **32**, 751 (1975).

Translated by V. Sakun